Volume 18
Number 21
7 November 2025
Pages 9293–9624

Energy & Environmental Science

rsc.li/ees

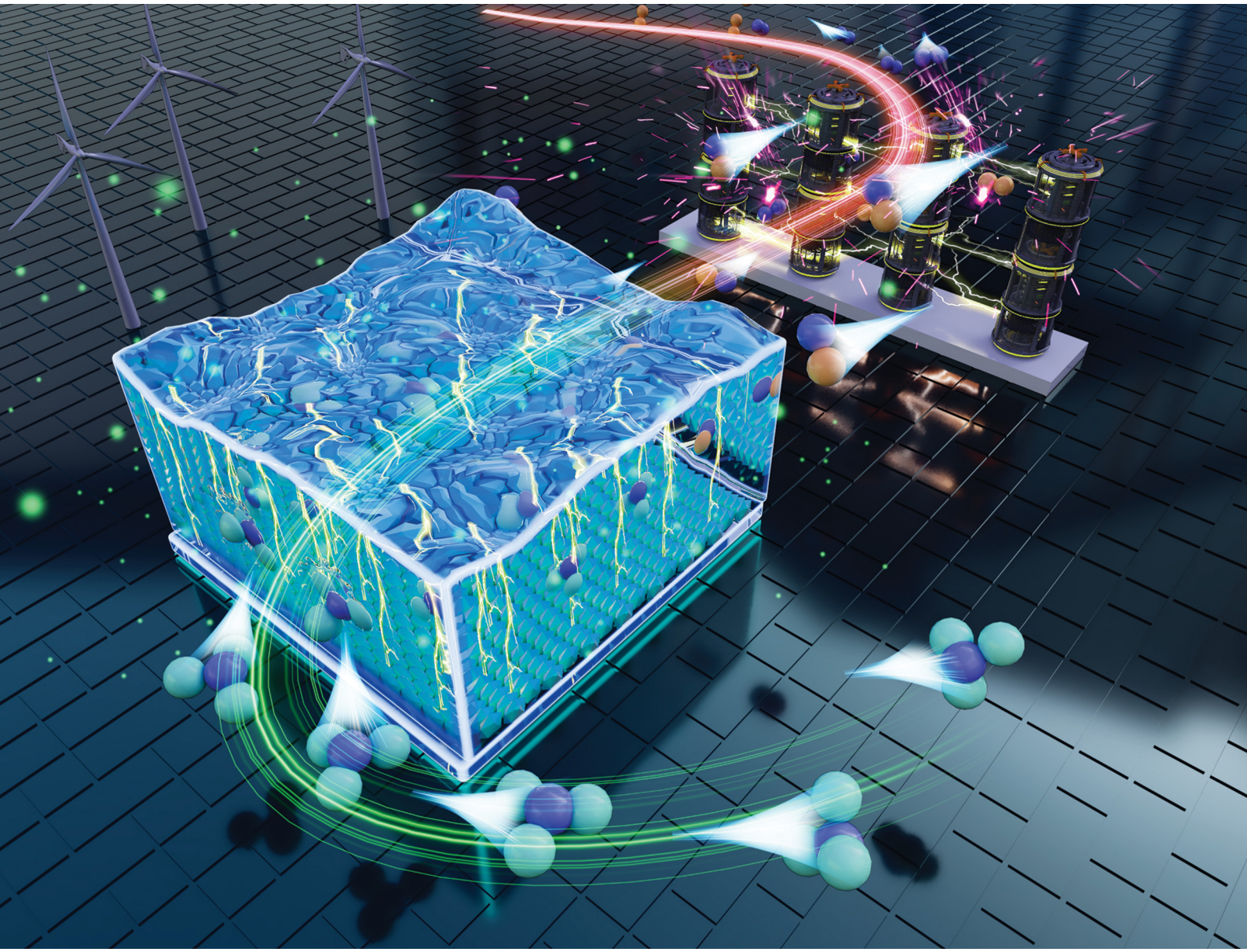

ISSN 1754-5706

ROYAL SOCIETY OF CHEMISTRY

PERSPECTIVE
Renwu Zhou, Ali R. Jalili *et al.*
A roadmap for ammonia synthesis *via* electrocatalytic reduction of nitric oxide

Energy & Environmental Science

ROYAL SOCIETY OF CHEMISTRY

PERSPECTIVE

View Article Online
View Journal | View Issue

Cite this: *Energy Environ. Sci.*, 2025, **18**, 9373

A roadmap for ammonia synthesis *via* electrocatalytic reduction of nitric oxide

Haoxuan Jiang,[a] Adel Rezaeimotlagh,[b] Sahar Nazari,[b] Renwu Zhou,*[a] Tianyu Li,[a] Jingwen Huang,[a] Dorna Esrafilzadeh [c] and Ali R. Jalili *[b]

Electrifying ammonia production demands modular systems powered entirely by renewable energy, eliminating dependence on fossil-derived hydrogen. This perspective argues that coupling non-thermal plasma oxidation of air to nitric oxide (NO) with five-electron electrocatalytic NO-to-NH_3 reduction (NORR) is a promising, energy-efficient and cost-realistic pathway. Drawing on lessons from mature electrochemical platforms, we identify the key mechanistic challenges and system-level gaps and translate them into targeted engineering strategies bounded by explicit techno-economic constraints. Our density functional theory analysis reveals a hidden bottleneck in nitrate-based pathways: slow nitrite desorption in an eight-electron/nine-proton deoxygenation and hydrogenation cascade, which NORR circumvents. To achieve industrially relevant rates and selectivity, we quantify the engineered reaction microenvironment, clarify associative *versus* dissociative pathways, and emphasise the role of gas-fed membrane assemblies and flow-by gas-diffusion electrodes. We also address integration, durability, and electrolyser design compatible with scale-out plasma–electrolyser architectures and set performance targets linked to TRLs. Finally, integrated techno-economic modelling indicates that NORR can reach cost parity with Haber–Bosch supplied by electrolytic hydrogen by ~2035, with the potential to capture ~1–5% of the global ammonia market by 2050 *via* distributed, modular deployment.

Received 19th June 2025,
Accepted 21st August 2025

DOI: 10.1039/d5ee03443d

rsc.li/ees

Broader context

Decarbonising fixed-nitrogen production has emerged as a cornerstone of both climate-neutral agriculture and future energy systems, yet global ammonia supply remains dominated by the fossil-intensive Haber–Bosch process. Electrified processes could break this fossil dependence by synthesising ammonia directly from renewable electricity under ambient conditions. Yet current electrochemical routes remain hampered: direct N_2 reduction must overcome the formidable N≡N bond, whereas nitrate pathways contend with dilute feedstocks and multistep oxygen-removal sequences. This perspective advances a strategically intermediate alternative that couples atmospheric–pressure non-thermal plasma oxidation of air to nitric oxide with a five-electron electrocatalytic NORR step. By integrating fresh, constant-potential DFT insights, system-wide kinetic modelling, and a unified techno-economic analysis, we construct a milestone-driven roadmap that translates molecular reactivity into process-relevant targets and technology-readiness benchmarks. The discussion encompasses plasma-reactor efficiency, electrocatalyst design, triple-phase boundary engineering, and gas-handling architectures while emphasising the economic and operational advantages of modular electrochemical stacks, whose scale-out deployment naturally aligns with variable renewable power and decentralised production. Parallels with the rapid learning curves of PEM water electrolysis and CO_2-to-CO GDE cells provide realistic, time-stamped performance horizons, highlighting how coordinated plasma-electrolyser co-design can unlock cost parity with electrolyser-assisted Haber–Bosch well before mid-century. By uniting cross-disciplinary lessons with a charted commercial trajectory, the perspective aims to galvanise collaboration among researchers, engineers, and industry to realise a resilient, fossil-free ammonia economy.

1. Challenge and opportunity for electrified ammonia production

At the intersection of climate stability, energy resilience, and food security, ammonia presents a unique vector for addressing global challenges. It sustains approximately half of the world's food supply, supports dispatchable power generation through co-firing technologies, and emerges as a versatile, carbon-free hydrogen carrier.[1–5] Currently, global ammonia production,

[a] *State Key Laboratory of Electrical Insulation and Power Equipment, Centre for Plasma Biomedicine, Xi'an Jiaotong University, Xi'an 710049, Shaanxi, China. E-mail: renwu.zhou@xjtu.edu.cn*
[b] *School of Chemistry, University of New South Wales (UNSW), Sydney, New South Wales 2052, Australia. E-mail: ali.jalili@unsw.edu.au*
[c] *Graduate School of Biomedical Engineering, University of New South Wales (UNSW), Sydney, New South Wales 2052, Australia*

exceeding 200 million tonnes annually, overwhelmingly relies on the Haber–Bosch process, an industrial marvel from the early 20th century now increasingly viewed as a substantial environmental burden.[6,7] Conventional Haber–Bosch plants, predominantly centralized and tethered to fossil fuel-rich locations, consume roughly 22 GJ per tonne of ammonia and emit about 1.2 tonnes of CO_2 per tonne of NH_3, operating under harsh conditions of 350–450 °C and 100–150 bar.[8–10]

However, the twenty-first-century energy transition is reshaping the economics of chemical synthesis.[11] Electrification is no longer restricted to high-value niches; it is now modularised, containerised, and scaled using repeatable factory-built units.[12,13] In 2023, green hydrogen electrolyser capacity doubled to 1.4 GW, and global manufacturing lines expanded to 25 GW $year^{-1}$, indicating a shift towards decentralised, demand-responsive deployment.[14] These units are not only less capital-intensive and more geographically flexible than giga-scale incumbents, but they can also perform millisecond-scale load-following to match the intermittent nature of solar and wind.[15,16] Ammonia, in contrast to hydrogen, is significantly more compatible with this modularity.[17,18] It liquefies at 9 bar and ambient temperature (compared to 70 MPa or −253 °C for H_2),[4,19] stores 12.7 MJ L^{-1}, delivers 176 kg H_2 t_{liq}^{-1} and can be transported *via* existing ammonia and LPG infrastructures.[20–23]

Electrifying ammonia synthesis offers a double benefit: it decarbonises the most significant industrial hydrogen sink and provides a high-density, long-duration storage medium for renewable energy. However, translating this potential into a practical process necessitates a novel synthesis pathway.[24] Early efforts focused on direct N_2 electroreduction at ambient conditions, but theoretical and practical bottlenecks were quickly identified. The 941 kJ mol^{-1} N≡N bond,[25–27] ~10 eV HOMO–LUMO gap,[28,29] and low aqueous solubility (0.6 mM) hinder reactivity. Even with optimised catalysts, current densities are below one mA cm^{-2}, with faradaic efficiencies typically under 1%.[28]

Li-mediated nitrogen reduction (Li-NRR) has shown significant laboratory metrics, making it a promising alternative. By plating Li^0 onto a porous cathode, N_2 can be cleaved *via* a Li_3N intermediate, enabling near-quantitative faradaic efficiencies

Haoxuan Jiang

Haoxuan Jiang is currently pursuing an MS in Electrical Engineering at Xi'an Jiaotong University. He earned a BS in Applied Chemistry from North China Electric Power University (Baoding) in 2024. His research interests center on electrochemical ammonia synthesis and plasma-assisted energy conversion.

Adel Rezaeimotlagh

Adel Rezaeimotlagh is a Postdoctoral Research Fellow at the University of New South Wales (UNSW), Australia. He received his PhD in Chemical Engineering from UNSW in 2020 and has over 5 years of industrial experience. His current research interests include emerging technologies for green chemical production, with a particular focus on techno-economic modelling and assessment of innovative processes to support sustainable and economically viable chemical manufacturing.

Sahar Nazari

Sahar Nazari is currently pursuing her PhD in Chemical Engineering at the University of New South Wales (UNSW), Sydney, and undertook a research visit at EPFL in Switzerland. Her work centers on the application of atomic-scale simulations, including density functional theory (DFT) and machine learning (ML), to guide the design and synthesis of advanced materials for sustainable technologies. Her current focus lies in nitrate reduction to ammonia and the optimization of electrochemical systems.

Renwu Zhou

Renwu Zhou is currently a professor at Xi'an Jiaotong University, China. He received his PhD degree from Queensland University of Technology, Australia in 2019 and worked as a Research Fellow at The University of Sydney from 2019 to 2022. His main research background lies in the area of plasma chemistry and plasma-enabled catalysis for green energy production.

and high current densities in pressurized batch systems.[30] Yet these gains come at a steep energy cost. The ≈ -3 V Li-plating step drives the net specific energy beyond 140 GJ t^{-1} NH_3, limiting overall energy efficiency to $\sim$28%, an order of magnitude higher than Haber–Bosch, which would require a cell potential below 0.38 V to match.[31] Moisture-sensitive, low-conductivity organic electrolytes further inflate ohmic losses and operating complexity, while growing lithium demand in the battery sector constrains supply. Recent techno-economic analyses therefore treat Li-NRR primarily as an upper-bound benchmark for single-cell performance: projected levelized ammonia costs remain above USD 3000 t^{-1} NH_3, well outside the parity window for large-scale deployment.[32]

These limitations have motivated research toward nitrogen-oxide pathways, such as nitrate electroreduction (NO_3RR), leveraging the weaker N–O bond and mature proton-exchange technologies as a more practical route to achieving cost-competitive electrified ammonia production.[33] Laboratory-scale systems demonstrated promising performance (hundreds of mA cm^{-2} and high selectivity).[34,35] Nevertheless, the viable feedstocks, including wastewater and agricultural runoff, contain nitrate concentrations ranging from 0.1 to 1 mM.[36] Even with full conversion, the resulting ammonium concentrations are low, necessitating energy-intensive separation.[37] Furthermore, complex electrolyte conditions of nitrate-rich waste can destabilise surface intermediates like NO_2*, leading to a rapid loss of activity. Moreover, field trials under realistic pH variations and contaminant levels reveal activity reductions of 30–50% within days, underscoring how nitrogen source complexity challenges laboratory-optimised catalysts.[38] While waste-nitrate electroreduction offers an elegant route for localised environmental remediation, it is fundamentally constrained by the dilute and inconsistent nature of available nitrate streams.[39] Consequently, it is unlikely to substantially contribute to the decarbonisation of the 200 Mt $year^{-1}$ global ammonia sector.[40] It should be considered a niche solution rather than a viable pathway to displace the Haber–Bosch process at a large scale.

Modern non-equilibrium plasma systems use electrons at 1–3 eV while maintaining gas temperatures near 300 K, unlike the 1903 Birkeland–Eyde arc that required over 10 MJ mol^{-1} to produce NO in thermal plasmas above 3000 K.[41] These vibrationally excited N_2 molecules react selectively with O atoms *via* the Zeldovich mechanism, producing NO while suppressing back-reactions.[42] Theoretical studies indicate that energy costs as low as 0.2 MJ mol^{-1} NO could be achievable under ideal conditions. In practice, however, gliding arcs, nanosecond pulsed discharges, and microplasma arrays typically report energy consumptions in the 1–3 MJ mol^{-1} range.[43,44] Further improvements are possible through strategies such as pulsed power shaping, after-cooling catalysts, and rapid quenching.

Plasma-generated NO can then be electrochemically reduced to ammonia *via* NORR, a five-electron/proton process that bypasses the complex deoxygenation pathway of NO_3RR and avoids *NO_2 desorption. The initial reduction step (*NO $\rightarrow$ *NOH) has a low barrier of approximately 0.45 eV,[45,46] and the reaction occurs at favorable potentials (+0.71 V *vs.* RHE), effectively suppressing hydrogen evolution. Recent experiments show growing alignment with theory: membrane-electrode assemblies (MEAs) fed with 1–2% NO achieve current densities of 100–150 mA cm^{-2} and faradaic efficiencies up to 96%.[47–49] Because NORR occurs at the gas-ionomer-catalyst triple-phase boundary, ammonia exits in gas form, allowing direct condensation and avoiding energy-intensive salt separation steps.[50]

Dorna Esrafilzadeh

Dorna Esrafilzadeh is a Scientia Senior Lecturer and Australian Research Council DECRA Fellow at the University of New South Wales (UNSW), Sydney. Her multidisciplinary research spans material chemistry, nanotechnology, and advanced fabrication, leading to applications in bioelectronics, device/material interfaces, and sustainable energy. Dr Esrafilzadeh was awarded multiple prestigious fellowships in Australia, including a Vice Chancellor's post-doctoral fellowship at RMIT (2017–2020), a Scientia fellowship at UNSW (2020–2027), and an ARC DECRA fellowship (2024–2027). She received the UNSW Dean of Engineering Excellence Award in Research and has published in prestigious outlets such as Nature Electronics and Nature Communications, earning high recognition, and secured multiple highly competitive national and international funding.

Ali R. Jalili

Ali R. Jalili is a Senior Lecturer and Australian Research Council Future Fellow at the School of Chemistry, UNSW Sydney. He received his PhD from the University of Wollongong in 2013. His research focuses on electrically driven green chemistry, emphasizing non-equilibrium plasma, plasma–electrochemical systems, atomically thin materials, additive manufacturing, and biomimetic designs. He leads a multidisciplinary group advancing green ammonia synthesis, sustainable fertilizers, and hydrogen technologies, with a strong emphasis on system integration and technology scale-up. Recently, his team has adopted AI-assisted materials discovery to accelerate catalyst development and optimize processes for scalable, cost-effective, and environmentally sustainable chemical production.

Fig. 1a and b presents a schematic of the decoupled, two-step modular process, separating NO formation from electrochemical ammonia synthesis. Because NO yield is maximised at short residence and rapid quench, scaling by numbering-up microplasmas (kW-class modules) is preferred: enlarging a single reactor increases residence, favours NO → N_2 + O_2/NO_2 recombination, and drives non-uniform fields that erode energy efficiency (Fig. 1c).

However, NO–NH_3 systems introduce a distinct set of integration challenges. Plasma effluents typically contain only 0.5–5% NO, along with residual O_2 and NO_2 that must be eliminated to avoid reoxidation and competitive side reactions during electroreduction.[51] This necessitates precise gas purification using pressure-swing adsorption, membrane separation, cryogenic pervaporation, or fundamental changes to the plasma reactor to improve NO selectivity and suppress secondary oxidants. Future research must match the plasma output composition to the downstream electrolyser's narrow operating tolerances, ensuring that NO concentration, purity, and flow stability are within the optimal window for triple-phase boundary reduction.[52] Simultaneously, humidity control remains critical: excess water vapour causes NO disproportionation to nitrite, whereas insufficient hydration degrades membrane conductivity. Existing proton-exchange membrane (PEM) fuel cell and CO_2 electrolyser solutions, including tailored flow-field architectures and gas diffusion electrodes (GDEs), perfluorinated ionomer coatings, and microchannel NH_3 condensers, can be adapted with minimal redesign.[53] However, both units must be designed in tandem to achieve stable, high-yield ammonia production with a fully integrated plasma–electrolyser module.

This perspective advances NORR as the most feasible and technologically promising route to electrified ammonia, grounded in rigorous microenvironment characterisation, quantitative techno-economic assessment, and whole-system engineering. Building on recent theoretical, computational, and experimental advances, we set out a structured, techno-economically constrained roadmap for modular, integrated plasma–electrolyser systems: Section 2 establishes the thermodynamic and kinetic foundations of ammonia electrosynthesis; Section 3 develops the engineered reaction microenvironment, encompassing mass transfer, interfacial pH and water activity, and nitric oxide solubility and speciation, and translates these insights into high-performance electrochemical interfaces; Section 4 translates the quantified microenvironmental and engineering constraints into forward-looking catalyst design strategies, linking adsorption and pathway considerations to materials classes and architectures that operate under NORR conditions and remain compatible with the system-integration requirements; Section 5 addresses system integration and stack architecture, converting microenvironment-informed targets into practical electrolyser design rules and stack-level performance milestones; and Section 6 closes with a detailed techno-economic analysis, scaling out and a realistic market-entry strategy. Together, these elements define a practical roadmap, anchored to cost-realistic targets, to accelerate the transition toward sustainable, distributed, and decarbonised ammonia production.

2. Oxidation states of nitrogen

2.1 Thermodynamic-kinetic hierarchy: why nitric oxide is the sweet spot

Electrochemical nitrogen conversion depends critically on the choice of nitrogen oxidation state, which must strike a balance between thermodynamic accessibility, kinetic favorability, and system integration. As shown in Fig. 2, the nitrogen sources, arranged in order of decreasing oxidation state, include nitrate (NO_3^-, +5) and nitrite (NO_2^-, +3) from industrial emissions/wastewater, nitric oxide (NO, +2) generated by non-thermal plasma, and atmospheric dinitrogen (N_2, 0). On the catalyst surface, all of these species undergo multi-electron–multi-proton stepwise reduction to NH_3. Fig. 2 also depicts the progressive gradient in proton and electron consumption, number of reaction steps, and bond activation difficulty among the different nitrogen sources.

Dinitrogen (N_2, oxidation state 0) is inert by design: its 941 kJ mol^{-1} triple bond and ~10 eV HOMO–LUMO gap confers extreme thermodynamic stability,[27,29] while its weak metal–surface interactions and sluggish $*N_2$ → *NNH activation restrict current densities to the milliampere scale.[54] On the opposite end, nitrate (NO_2^-, +5) and nitrite (NO_2^-, +3) are highly oxidised and must be deoxygenated through long, branched reaction networks that demand stringent control of pH, potential, and proton flux. These intermediates are prone to side reactions, including nitrite desorption and N_2O evolution, making them difficult to reduce selectively at scale.[55–57]

Nitric oxide (NO, +2) offers a redox compromise. Its N=O bond (607 kJ mol^{-1}) is weaker than the N≡N bond but strong enough to preserve molecular integrity upon adsorption.[58] Critically, its open-shell electronic configuration, an 11-valence-electron system with a half-filled π* orbital, enables facile electron transfer through both back-donation from transition-metal d-bands and forward donation into bonding states.[58–60] The electron affinity (~0.02 eV) and moderate ionisation energy (~9 eV) position NO as uniquely receptive to charge transfer, unlike N_2 (−1.9 eV EA), and substantially more reactive than nitrate or nitrite, which require pre-reduction or deoxygenation before hydrogenation.[61,62] As a result, the activation barrier for the first protonation step (*NO → *NOH) is reduced to just 0.35–0.45 eV, a threshold significantly below that of $*N_2$ or $*NO_3$ activation.[63]

The +2 oxidation state of NO simplifies the reaction topology. Rather than traversing eight- or nine-electron cascades with multiple labile intermediates, NO reduction proceeds *via* a five-electron/five-proton sequence, NO* → NOH* → NHO*/NH* → NH_2* → NH_3, comprising largely neutral or weakly polar species.[64,65] These intermediates remain surface-bound, with minimal susceptibility to pH or field-induced desorption.[66–68] Furthermore, the absence of charged oxygenates eliminates proton-coupled side reactions and simplifies

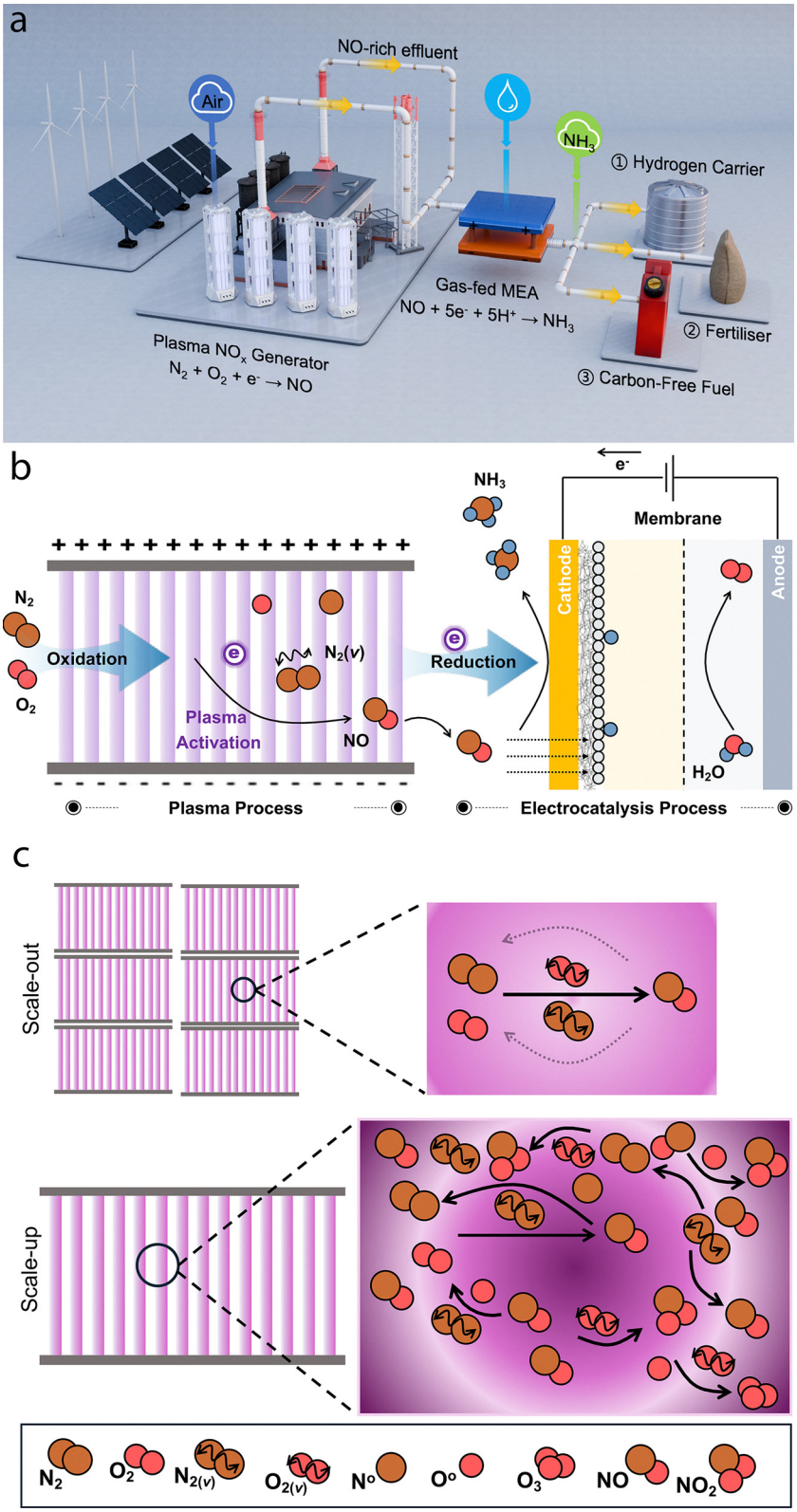

Fig. 1 Modular plasma–electrocatalytic pathway for sustainable ammonia synthesis. A renewable-powered non-thermal plasma oxidises air to 1–5 vol% NO (~1–3 MJ mol^{-1}), which feeds a gas-fed MEA where $NO + 5H^+ + 5e^- \rightarrow NH_3$ at 100–500 mA cm^{-2} (a) and (b). (c) Scaling strategy: scale-out of short-residence, rapidly-quenched kW-class modules maintains NO selectivity and lowers recombination; scale-up to a single large vessel lengthens residence, accumulates $NO/O_2/NO_2$ and hot zones, promotes reverse chemistry, complicates uniform power coupling/heat removal, and creates single-point-failure risk, so numbering-up best supports TRL, compatible better with intermittent renewable energies and support modular deployment.

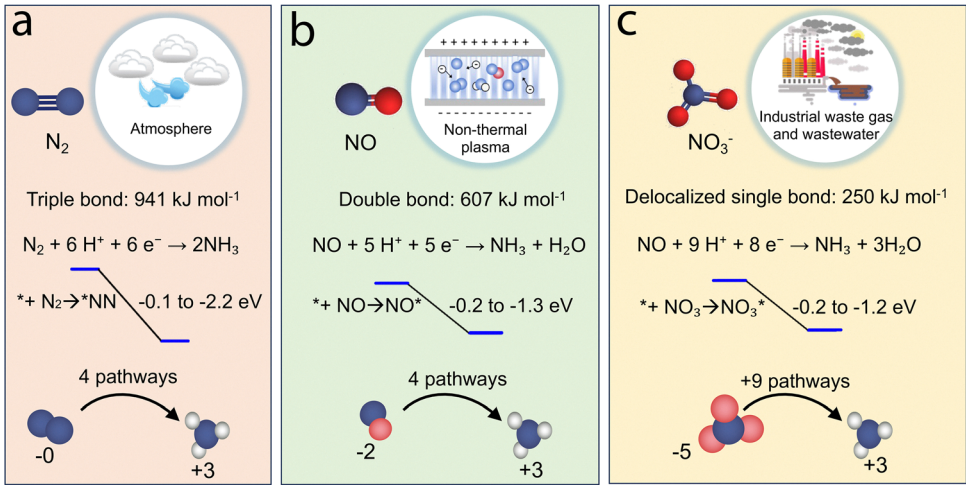

Fig. 2 Electroreduction pathways for ammonia synthesis from nitrogen species at different oxidation states, (a) N_2 (0), (b) NO (+2), and (c) NO_3^- (+5), along with their respective sources, bond dissociation energies (kJ mol^{-1}), overall reduction stoichiometries, and first-step adsorption free energies. Sphere colours denote nitrogen (blue), oxygen (red), and hydrogen (white).

interface design, particularly for membrane systems operating in mildly acidic or neutral environments.[69]

These thermodynamic and kinetic advantages manifest at the device level. In gas-fed membrane–electrode assemblies supplied with 1–2% NO, partial NH_3 current densities above 100 mA cm^{-2} and faradaic efficiencies exceeding 60% have been routinely achieved at cell voltages where nitrate systems remain mass-transport limited.[70] Furthermore, operating NORR entirely in the gas phase lets NH_3 be condensed directly, eliminating any brine-handling step.

In CO_2 reduction, the transformation of CO_2 to CO (*CO_2 → *COOH → *CO) substantially lowers the activation barrier for further hydrogenation reactions, analogous to how *NO intermediates in NO reduction avoid the need for complete deoxygenation and reduce the electron–proton burden of the overall transformation.[71,72] Both CO and NO occupy intermediate oxidation states, with open-shell or partially filled orbitals that facilitate charge transfer to catalyst surfaces and unlock favourable reaction energetics. In CO_2-to-CO-to-C_2^+ electroreduction,[73] the CO intermediate allows for >100 mA cm^{-2} partial current densities and direct gas–solid–liquid triple-phase boundary control. This fundamental knowledge and these system design principles are directly applicable to NORR systems.

This analogy underscores the broader insight that intermediate oxidation state molecules, whether NO or CO, act as "reaction enablers" by circumventing the formidable barriers of fully oxidised precursors (NO_3^- or CO_2) and offering a more streamlined, energetically accessible reaction coordinate. Accordingly, the strategic focus on NO electroreduction in ammonia synthesis aligns with the same fundamental design paradigm proven in CO_2RR: leveraging intermediate redox species to reduce reaction complexity, optimise selectivity, and harness gas-phase reaction interfaces for modular, scalable system integration.

2.2 Reaction-network complexity: contrasting nitrate, nitrite and nitric oxide routes

The appeal of nitrate electrochemical reduction lies in its apparent thermodynamic advantage: the N–O bond in NO_3^- is significantly weaker than the N≡N bond in dinitrogen, allowing activation at lower overpotentials.[74] Yet this advantage is offset by a complexity penalty. Reducing nitrate to ammonia requires nine protons and eight electrons delivered through a highly branched sequence involving at least thirteen adsorbed intermediates, NO_3*, HNO_3*, NO_2*, NO_2H*, NO*, NOH*, NH*, NH_2*, and their oxygenated or protonated variants, each with distinct kinetics, coverage effects, and pH sensitivity.[35] Microkinetic modelling and experimental data converge on two critical barriers: the initial proton-coupled electron transfer from NO_3* to HNO_3*, and the N–O bond cleavage in NO_2H*, both of which dominate the reaction rate in the mildly acidic to neutral pH regime commonly used to stabilise nitrate and suppress nitrite disproportionation.

Selectivity loss is an endemic problem. NO_2*, though a required intermediate, is metastable on most catalytic surfaces. When its surface coverage exceeds ~0.1 monolayer, it readily desorbs as nitrite, which either accumulates in the electrolyte or migrates downstream, competing for active sites and rerouting the catalytic flux.[69,75] This dynamic destabilisation is exacerbated under real-world conditions. Field tests confirm that these complex intermediates destabilize under real-world pH and contaminant variations, creating persistent selectivity challenges in practical nitrate electroreduction.

Nitrite reduction condenses the electron–proton requirements by one pair but retains substantial complexity. The NO_2* intermediate still undergoes branching: it can be hydrogenated to NO*, desorb as gaseous NO, or couple to form N_2O.[76–78] The latter pathway becomes dominant in concentrated alkaline media, diverting current away from ammonia. Restoring selectivity in such conditions often necessitates

pulse-modulated waveforms to rebalance intermediate coverage and suppress parasitic N–N coupling.[79] Proton management further complicates nitrite conversion. At elevated current densities, hydroxide accumulation near the cathode depletes local proton activity and elevates the barrier for water dissociation. This shifts the entire reaction free-energy profile uphill by more than 400 kJ mol^{-1} relative to acidic operation.[80] Buffering can stabilise pH, but it introduces trade-offs: elevated salt concentrations and ohmic resistance, both of which complicate downstream ammonia separation.[50] Moreover, buffering does not prevent localised pH gradients that destabilise adsorbed NO_2* and NOH*, especially in flow systems.

In CO_2 reduction, the transformation of CO_2 to CO bypasses the formidable activation barrier of the fully oxidised CO_2 and leverages the intermediate oxidation state of CO to enable selective hydrogenation and carbon–carbon coupling. This paradigm has been extensively validated in gas-diffusion architectures that maintain high local concentrations of CO and stabilise intermediates against competitive desorption.[81] The parallels to nitrate and nitrite reduction are striking: NO, like CO in CO_2RR, is an intermediate oxidation state that avoids the deoxygenation bottlenecks and intermediate destabilisation inherent to nitrate and nitrite pathways. Leveraging this analogy can guide catalyst design and reactor engineering to stabilise critical intermediates and maintain high selectivity, directly informing NORR development.

2.3 Mechanistic bifurcation: dissociative and associative NORR pathways

Having established that NO circumvents the extensive deoxygenation and proton-coupled electron transfer burdens of nitrate and nitrite pathways, we now turn to the mechanistic nuances that define how NO reduction proceeds selectively and efficiently. The five-electron conversion of NO to NH_3 can occur *via* two fundamentally distinct reaction pathways, with their relative predominance determined by the identity of the catalyst, the applied potential, and the local availability of hydrogen. The dissociative pathway produces surface-bound N* and O* that are then hydrogenated when the adsorbed molecule immediately undergoes N–O bond scission following coordination.[66,67] Quantum chemical calculations indicate that the intrinsic cleavage barrier is approximately 0.9–1.1 eV for noble metals, while it can be as low as 0.4 eV for early-transition nitrides and carbide-derived MBenes like WB, where back-donation into the antibonding π* orbital both elongates the N–O bond and stabilises the resultant adatoms.[50] Upon dissociation, the nitrogen atom adheres to the established sequence N* → NH* → NH_2* → NH_3, concurrently reducing O* to water. The primary benefit is that distal hydrogenation of a strongly bound N* inhibits the desorption of partially hydrogenated intermediates, achieving near-quantitative faradaic efficiency at low overpotentials when cleavage occurs rapidly. The penalty serves as the catalyst specificity: materials that sufficiently weaken the N–O bond frequently bind O* so strongly that the removal of product water becomes rate-limiting or induces oxide formation.

The associative pathway bypasses this cleavage penalty by hydrogenating the intact NO molecule *via* NOH*, HNO*, and NH_2OH* intermediates prior to the ultimate N–O bond cleavage.[66] The energy barrier for the initial proton-coupled electron transfer to generate NOH* on coinage metals and single-atom Cu or Fe centres is merely 0.3–0.5 eV;[82] however, the subsequent dehydration of NH_2OH* to NH* may surpass 0.8 eV, making that step the kinetic bottleneck. Due to the incomplete reduction of early intermediates, N–N coupling to N_2O or disproportionation to NO_2^- becomes competitive at concentrations exceeding approximately 5% NO, necessitating gas-phase operation with dilute feeds to achieve high selectivity.[70] The associative pathway is enhanced by dynamic hydrogen coverage: constant-potential *ab initio* dynamics demonstrate that alternating high- and low-proton conditions synchronise NOH* formation with N–O bond cleavage, a principle recently utilised in square-wave pulsed electrolysis to elevate partial NH_3 currents beyond 200 mA cm^{-2} on MnB nanoflakes.[50]

Together, the two pathways define a mechanistic window: when ΔG_{*NO} is moderate, the free-energy span is shared between N–O cleavage and the first hydrogenation, yielding a shallow apparent Tafel slope.[83,84] The branching ratio is set by interfacial H* coverage[85] and NO activity.[86] These two pathways set distinct electronic and coverage requirements that we later translate into materials and interface choices.

2.4 Hydrogen-transfer mechanisms: Tafel *versus* Heyrovsky control

The delivery of hydrogen equivalents to adsorbed intermediates is the most important elementary act in nitric oxide electroreduction. Two established pathways proposed: the Tafel pathway, wherein hydrogen atoms pre-adsorbed on the catalyst surface migrate to or are abstracted by NO-derived species, and the Heyrovsky pathway, in which protons from the electrolyte react with an electron at the surface during the reaction.[87,88] While both mechanisms yield identical product stoichiometry, they impose different kinetic and selectivity limitations influenced by the electronic structure of the catalyst, the applied potential, and the pH of the electrolyte.

The Tafel pathway predominates in platinum-group metals. Hydrogen adsorption is quasi-reversible and incurs an enthalpic penalty of approximately 0.25 eV, resulting in millisecond surface coverages of 0.2–0.5 monolayers even at moderate overpotentials. Infrared reflection–absorption spectroscopy indicates that H* species engage in end-on interactions with NO* to produce NOH* in a barrierless or sub-0.2 eV process;[89] however, the elevated hydrogen coverage enhances the competing H* + H* → H_2 recombination, thereby constricting the potential range for selective NORR. To inhibit H_2 evolution, one must either employ alloying (such as Pt–Hg or Pt–Bi) to differentiate between NO and H adsorption sites or function in mildly acidic polymer electrolytes, where proton transport, rather than surface coverage, constrains HER kinetics.[90]

Copper, iron, and manganese-based catalysts promote the Heyrovsky mechanism at similar potentials.[91,92] DFT constant-

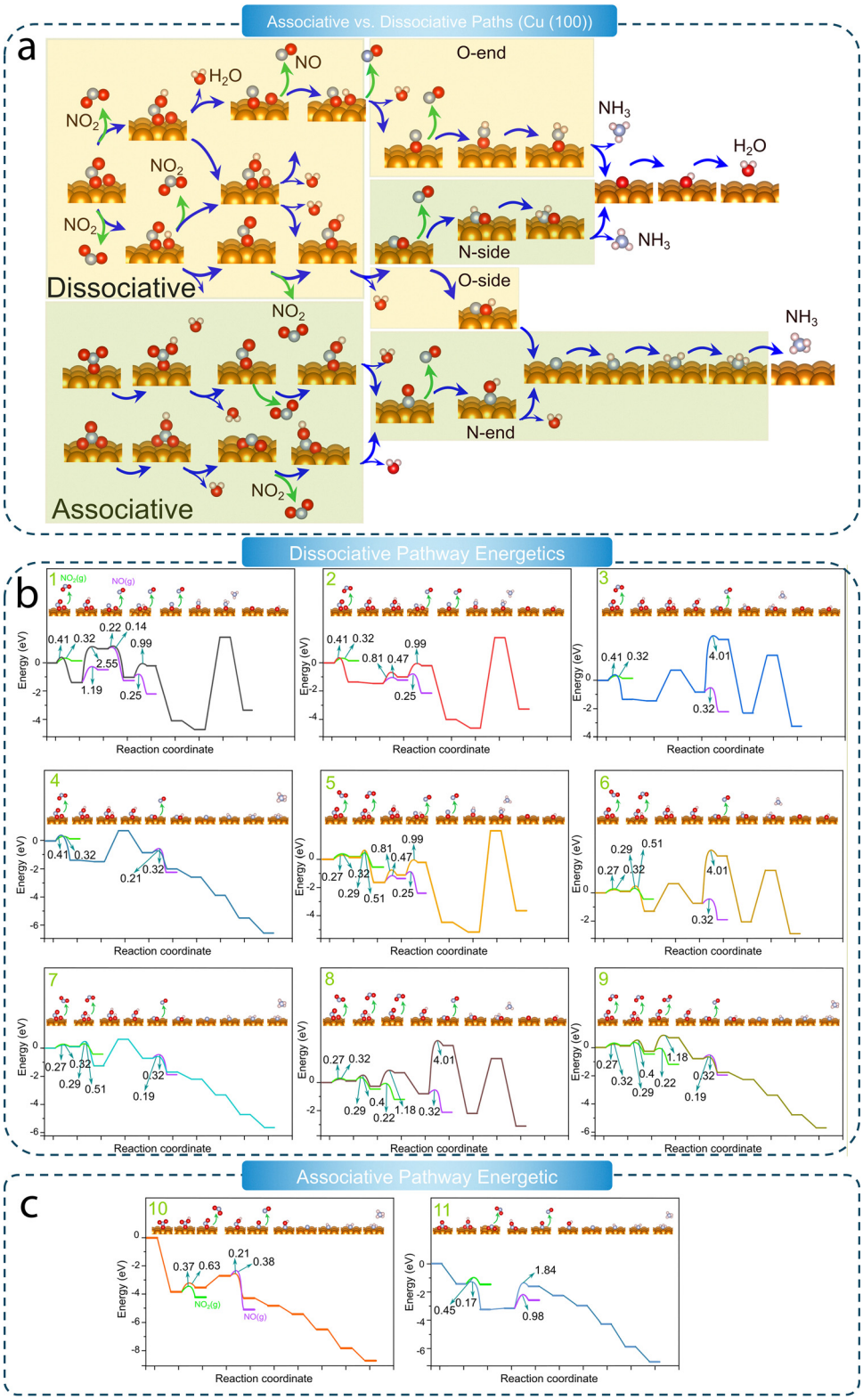

Fig. 3 DFT modelling of electroreduction of highly oxidised nitrogen pathways to ammonia and kinetic desorption sinks. (a) Schematic illustrations of associative and dissociative nitrate electroreduction pathways on Cu(100), capturing key proton-coupled electron transfer steps and the evolution of *NO_2, *NO, and *O intermediates toward NH_3 formation or desorption events, with green arrows indicating desorption events and blue arrows marking water formation and the continuation of the reaction pathway. Reaction coordinate diagrams for the nine dissociative (b) and two associative (c) pathways, highlighting transition-state energies ($\Delta G^{\ddagger}$) and reaction free energies (ΔG) for hydrogenation, N–O scission, and desorption events, with green and purple lines indicating desorption of *NO_2 and NO, respectively.

potential calculations identify the transition state for the distal-Heyrovsky protonation of NO* at 0.35–0.45 eV, marginally exceeding the Tafel analogue but achieved at reduced surface hydrogen coverage, thus alleviating HER.[93] *Operando* Raman experiments on Cu(111) demonstrate a kinetic isotope effect of 2.1 when D_2O is substituted for H_2O, supporting a rate-limiting proton-coupled electron transfer instead of H* recombination. The equilibrium between these two pathways is highly dependent on pH: increasing the bulk pH[94] by two units reduces the Heyrovsky overpotential by approximately 120 mV (due to the Nernstian term) while the Tafel barrier remains relatively constant, thereby favouring Heyrovsky-controlled NH_3 synthesis in alkaline or buffered neutral environments.

Coverage and potential oscillations add another layer of complexity.[95] Square-wave pulsed electrolysis, which alternates between a cathodic phase (to enrich the surface with H*) and a mild anodic phase (to desorb excess H_2 and re-adsorb NO), has doubled the partial NH_3 currents on MnB nanoflakes compared to steady-state bias, illustrating that the dynamic synchronisation of the two pathways can exceed the Sabatier optimum of static operation.[95] Strategies adapted from membrane–electrode CO_2 electrolysers, including duty-cycle-controlled humidification and ionomer gradients, provide further mechanisms for modulating local proton activity and influencing the Tafel/Heyrovsky dynamics.

2.5 Hidden desorption sink: $*NO_2$ escape in electroreduction of highly oxidised nitrogen

Selective ammonia synthesis from nitrate or nitrite hinges on keeping the $*NO_2$ intermediate surface-bound long enough for hydrogenation. Evidence from gas-fed flow reactors shows that this condition is not trivially met. Yuan *et al.* showed that increased superficial gas velocity in a 200 mA cm^{-2} membrane–electrode assembly correlates linearly with nitrite escape, highlighting that convective desorption can outpace hydrogenation at residence times below approximately 300 ms.[96] Jia *et al.* mitigated the problem with a Cu/Ag–Ru tandem that chemisorbs nitrite strongly on Ru; a Ru-free Cu/Ag control accumulated millimolar nitrite under identical flow.[80] Most DFT studies report only relative free energies and often presume barrierless hydrogenation when $\Delta G(*NO_2H) < \Delta G(NO_2(g))$. Where transition-state searches exist, hydrogenation barriers of 0.60–0.85 eV are consistently higher than the 0.35–0.45 eV estimated for desorption under alkaline shear.[97] Our flow-cell experiments corroborate this kinetic preference, showing persistent nitrite breakthrough above 50 mA cm^{-2} despite quantitative nitrate conversion in batch H-cells.[98]

To quantify how often the desorption route wins, we mapped eleven mechanistic pathways for nitrate electroreduction on Cu(100) (Fig. 3) using climbing-image NEB calculations. Nine proceed through dissociative adsorption ($*NO_2$ + *O), while two follow an associative sequence in which nitrate adsorbs intact.[99] In the dominant dissociative pathways, the activation energy for $*NO_2 \rightarrow NO_2(g)$ ($\approx$0.32 eV) is 0.10–0.25 eV lower than hydrogenation to $*NO_2H$ ($\approx$0.41 eV), so kinetic control, rather than thermodynamics, determines the fate of $*NO_2$.[100] Later in the cascade, the barriers and reaction free energies for NO(g) release also fall below those for further proton-coupled electron transfer, making desorption the prevailing sink when proton activity is limited.

However, this issue is potentially solvable *via* intelligent catalyst and electrode design. Recent studies on high-entropy liquid–metal alloy catalysts highlight that carefully engineered multi-element active sites can finely tune adsorption energies of intermediates, thereby suppressing unwanted desorption pathways and enhancing selectivity.[101] Moreover, strategies successfully employed in CO_2 electroreduction, such as optimized microenvironments, rapid proton delivery systems, and tailored gas-phase reactor architectures, offer valuable insights for mitigating NO_2 desorption.

Nitric oxide bypasses these complications. NORR starts at the +2 oxidation state and needs only a single deoxygenation step. Five sequential proton–electron pairs ($NO* \rightarrow NOH* \rightarrow NH* \rightarrow NH_2* \rightarrow NH_3$) dominate under practical overpotentials; competing N–N coupling pathways emerge only at NO partial pressures >0.5–5% produced by typical non-thermal plasma reactors.[102] With no oxygenated anions, local pH remains near the membrane value, and water activation is never rate-limiting. Consequently, NORR can be implemented in a PEM-like MEA that focuses on humidity regulation and O_2 exclusion, challenges already solved in CO_2 electrolysers,[103,104] whereas nitrate electrolysis must juggle pH buffers, ion-exchange zones, and pulsed waveforms to shepherd intermediates.[105,106]

3. Electrochemical interfaces and electrolyte engineering

Building on the molecular simplicity of the five-electron NO reduction pathway, we now address the engineering imperatives, electrolyte selection, interface hydration, and NO mass transfer, needed to translate this mechanistic advantage into practical devices. Fig. 4 summarises the core design principles and outstanding challenges related to electrochemical interfaces and electrolyte management in NORR, while Fig. 5 illustrates how these strategies have been implemented in recent literature. In general, precise regulation of proton activity is required to maintain the potential 50–80 mV below the onset of the hydrogen evolution reaction (HER), thereby ensuring the preferential reduction of NO. Simultaneously, maintaining a membrane hydration level above 95% and controlling the local pH near the membrane's isoelectric point (pH 5–6) are essential for minimizing resistance and suppressing hydroxide intrusion. From the perspective of mass transport, given the limited solubility of NO in aqueous media, enhancing its interfacial concentration to the range of 10–50 mM through gas diffusion electrode structures or pressurization is crucial for sustaining catalytic activity. Lastly, electrolyte composition, including strong acids, strong bases, neutral buffers, and ionic liquids, must be carefully selected to achieve a synergistic balance between catalytic selectivity, HER suppression, and device scalability.

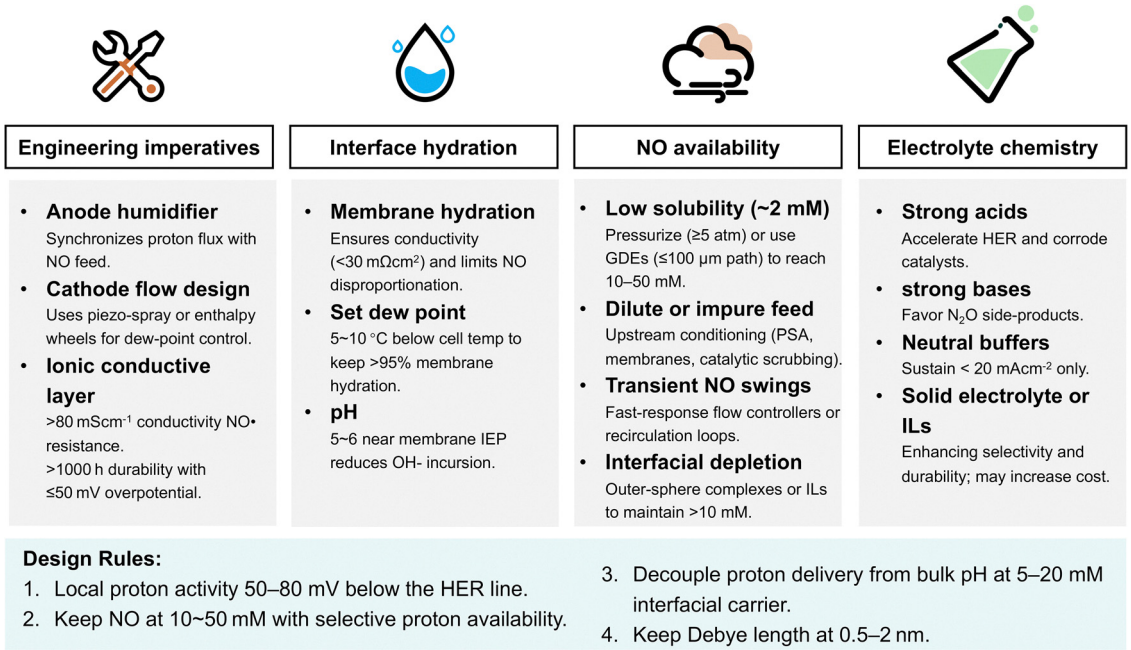

Fig. 4 Engineering and operating design framework for high-performance nitric oxide electroreduction to ammonia.

3.1 Proton budget and pH management

Efficient electrochemical reduction of nitrogen oxides hinges on an electrolyte that can deliver protons to the cathode in lockstep with the faradaic current while simultaneously removing the hydroxide generated by charge balance.[63] In aqueous nitrate cells, each electron consumes one proton and releases OH^-, causing the local cathode pH to rise above 12 within five minutes when the current density exceeds approximately 50 mA cm^{-2}.[107] *Operando* fibre-optic probes confirm that the acidification of the anode imposes a thermodynamic penalty of $\sim$0.40 MJ mol^{-1} NH_3 and, by infrared tracking, strips $*NO_2$ and *NOH coverages on Cu and Ni by $\sim$40% in 24 hours. Producing one tonne of NH_3 day^{-1}, assuming 100% electrolyser efficiency, implies the anode must split approximately 33 kg H_2O h^{-1} (794 kg H_2O day^{-1}). Every additional 0.10 V across the interface, whether from bubble masking or carbonate fouling, adds at least 50 kWh t^{-1} NH_3 (3.06 MJ mol^{-1}).

Flooding the cell with acid can accelerate HER and dissolve earth-abundant catalysts, while strong alkaline buffers reduce the equilibrium potential to 60 mV pH^{-1} and promote N_2O formation. Neutral phosphate or borate delays the problem only to $\approx$20 mA cm^{-2}. Outer-sphere shuttles like Fe(II)–EDTA temporarily increase local NO_3^- activity, but scale-up is hindered by oxidative fragility and assay interference.[108] Ionic liquids inhibit HER and absorb millimolar NO, but their viscosity and cost preclude large-scale use.

The nitric oxide pathway rewrites this balance sheet. Because NO is already in the +2 oxidation state, NORR terminates after 5 proton–electron pairs, producing no bulk hydroxide. A membrane–electrode assembly uses a solid polymer electrolyte to transport protons from a humidified anode. The cathode operates near the membrane isoelectric point (pH $\approx$ 5–6), preventing Donnan-driven OH^- incursion.[109] Keeping the dew point 5–10 °C lower than the cell temperature of 60–80 °C maintains >95% membrane hydration, keeps area-specific resistance under 30 mΩ cm^2, and reduces NO disproportionation. Under these conditions Singh-Morgan *et al.* maintained 150–200 mA cm^{-2} partial NH_3 current for 100 h with <1% loss.

The theoretical water-splitting requirement is reduced from 237 kWh to 132 kWh t^{-1} NH_3 by lowering the proton budget from nine to five.[110] However, this figure represents only the ideal thermoneutral potential for water-splitting-derived protons (1.23 V).[111] In practice, stack voltages typically exceed 1.5 V, raising the practical electrolyser energy demand closer to 0.9–1.0 MWh t^{-1} NH_3 once overpotentials, balance-of-plant loads, and faradaic losses are included.[112] This streamlined proton balance not only reduces energy and material costs but also eliminates approximately 100 kg of spectator K^+ per tonne of ammonia, obviating the need for electrodialysis purge. Consequently, it enables compact, modular electrolyser architectures that can be seamlessly coupled to variable NO feeds from plasma-based air oxidation units or other distributed sources.

Realising this molecular-level advantage in a functional device demands three interdependent tasks: (i) an anode humidification module that throttles proton flux to match the plasma-derived NO supply, similar to dynamic water management in high-temperature PEM fuel cells; (ii) a cathode manifold capable of millisecond-scale dew-point modulation, achievable *via* piezo-spray injectors or enthalpy wheels, to mitigate membrane dehydration during transient load-shedding and dampen moisture spikes that foster nitrite formation; (iii) an ionomer binding layer sustaining >80 mS cm^{-1} conductivity at $\lambda \approx 8$ while withstanding $NO^\bullet$ radical exposure.

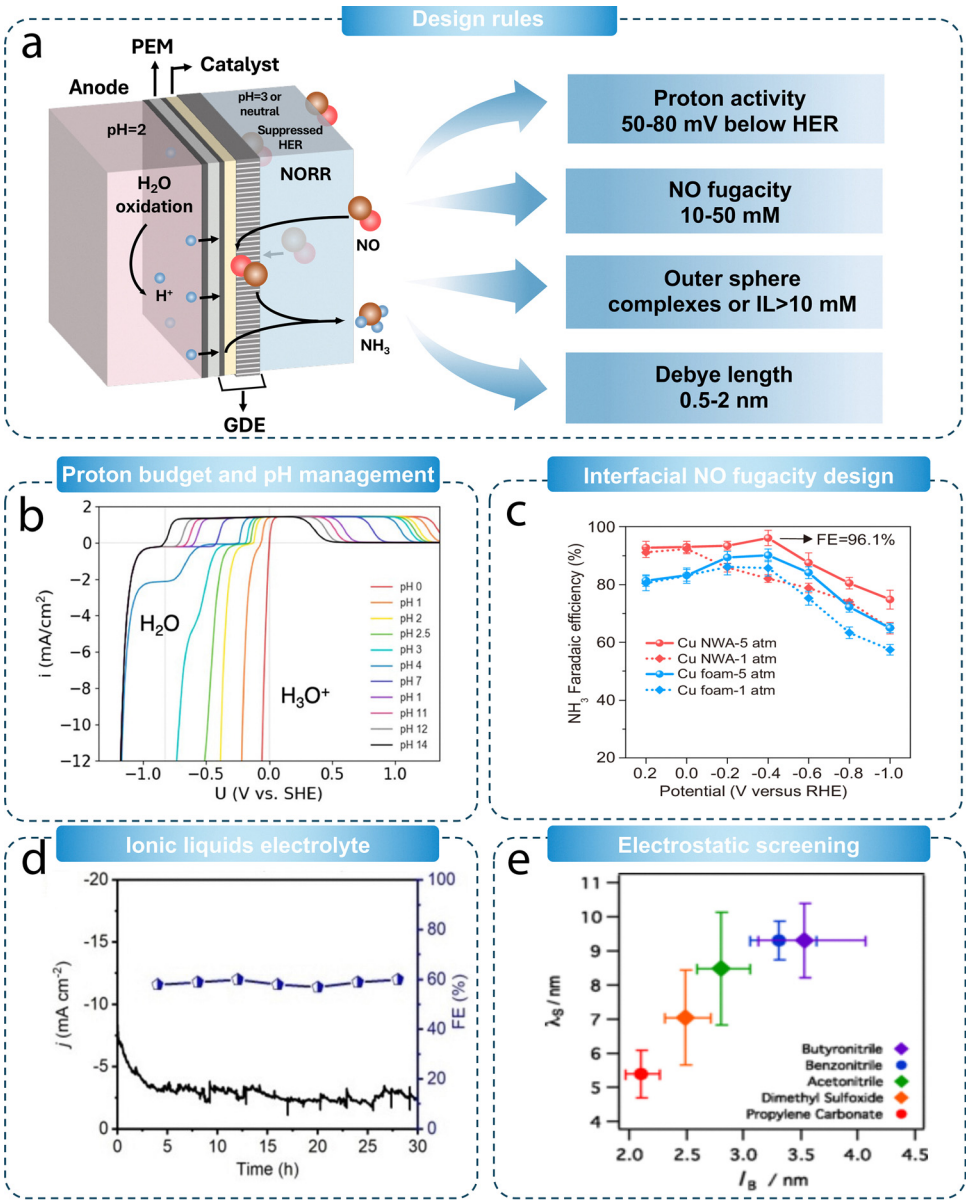

Fig. 5 (a) Design of electrochemical interfaces for efficient NORR. (b) Computed HER/HOR polarization curves using the DFT activation energies and mean-field microkinetic modeling.[113] Copyright 2019, American Chemical Society. (c) NH_3 FE over Cu NWA and commercial Cu foam at different applied potentials at 25 °C under 1 atm, 5 atm NO, respectively.[112] Copyright 2025, Springer Nature. (d) Chronoamperometry stability test of P–MoS_2/NS in NO-saturated IL electrolyte at −0.7 V *vs.* RHE.[123] Copyright 2022, Wiley-VCH. (e) The measured electrolyte screening lengths are consistent with a linear increase with the Bjerrum length.[38] Copyright 2017, American Physical Society.

Recent advances in partially fluorinated poly(arylene ether) backbones demonstrate >1000 h durability in this environment with ≤50 mV overpotential penalty.

The pH remains a decisive lever even in NO systems. Strongly acidic media (pH ≈ 1) provide protons so readily that the Heyrovsky step outpaces *NO hydrogenation, turning the cathode into a hydrogen pump and throttling NH_3 formation.[113] Shifting to neutral or mildly alkaline buffers drops the proton chemical potential by 50–80 mV, tipping selectivity: Kouer *et al.* showed that Cu foil at pH 1 yields mostly NH_3 + H_2, whereas at pH 7 the spectrum drifts to N_2O/N_2; converting the same Cu into a hollow-fibre GDE fed with 10% NO restored proton availability, driving FE(NH_3) ≈ 90% and 0.4 mmol h^{-1} cm^{-2} at −0.6 *vs.* RHE.[63] Design Rule 1: maintain the local proton activity 50–80 mV below the HER Nernst line, low enough to suppress hydrogen evolution yet high enough to complete the alternating or distal protonations of NORR. This balance ensures that the Heyrovsky and Volmer steps of hydrogen evolution remain thermodynamically disfavoured, while the energetically accessible hydrogenation of NO and NOH intermediates proceeds rapidly. Online EC-MS data illustrate this switch: Cu in 0.05 M H_2SO_4 shows early HER onset, while the same electrode in 0.5 M Na_2SO_4 remains dominated by NORR until the buffer depletes.[114]

3.1.1 Governing the interfacial pH. Managing interfacial, rather than bulk, pH can be a key lever for selective nitric oxide electroreduction, an approach already explored in similar reactions such as nitrate reduction. *Operando* fiber-optic microprobes and confocal fluorescence imaging reveal that, even in 0.5 M phosphate buffer (pH 7), the cathode surface can drift 4–8 pH units above the bulk within 60 s once $j \geq 50$ mA cm^{-2}, throttling *NO_2/*NOH hydrogenation and rerouting the reaction toward N_2O/N_2 formation.[115] To tame this gradient, five complementary strategies have emerged:

First, combining high-capacity phosphate/borate buffers with forced convection replenishes H^+ faster than it is consumed, maintaining interfacial pH $\leq$ 9 at 200 mA cm^{-2} and doubling NH_3 faradaic efficiency.[116] Second, the $Ru(NH_3)_6^{3+/2+}$ system demonstrates reversible proton shuttles, which decouple proton delivery from bulk acidity. This shuttle recycles H^+ to adsorbed *NO_x by cycling between the outer Helmholtz plane and the diffusion layer, maintaining 78% FE at 120 mA cm^{-2} for 12 hours in neutral 0.1 M Na_2SO_4 and reducing the surface-to-bulk pH gap to less than 2.[117] Third, bipolar–membrane MEAs provide an inherent acid flux toward the cathode; at 100 mA cm^{-2}, a physically interlocked BPM increased FE(NH_3) from 34% to 82%, keeping the bulk electrolyte near pH 7.[118] Fourth, millisecond pulsed-potential waveforms periodically re-acidify the interface, relax diffusion layers, and push single-pass NH_3 yields above 90%.[119] Fifth, hierarchically porous Cu gas-diffusion architectures, such as hollow-fibre macropores, shorten proton-diffusion paths and stabilize buffer anions near active sites. A copper hollow-fibre GDE sustained $\approx$90% FE(NH_3) at 0.4 A cm^{-2}, maintaining interfacial pH below 8.[114] Similarly, a hierarchical Cu-nanowire/graphene electrode achieved 85% FE at 300 mA cm^{-2}, demonstrating a surface–bulk pH gap <1 in CO_2 reduction to formate.[120] Thus, Future NO RR studies should benchmark interfacial pH control against $\geq$80% FE at $\geq$200 mA cm^{-2}, using BPM or pulsed-potential protocols as the current best-practice baselines.

Selectivity is also conditioned by the prevailing hydrogen-transfer regime. Practical diagnostics, Tafel slope, kinetic isotope effect, and the pH-shift of onset, reveal whether electrochemical desorption (Heyrovsky-biased) or surface recombination (Tafel-biased) governs the competing H_2 pathway. When the response is Heyrovsky-biased, isolated or ensemble-blocked surface motifs that limit contiguous H* combined with a mildly acidic proton supply (pH $\approx$ 5–6) favour the *NO $\rightarrow$ *NOH hydrogenation; thin ionomer films and controlled humidification moderate interfacial water activity, and short duty-cycle pulsing helps to refresh coverage. When Tafel recombination dominates, weaker H adsorption or frustrated H–H pairing, a small downward shift in proton activity from the operating window above, and higher local NO activity (*via* gas-side fugacity and sub-nanometre confinement) bias coverage towards *NO/NOH rather than H. In both cases, keep the local proton activity 50–80 mV below the HER Nernst line (Design Rule 1) and re-check the Tafel/KIE signature after each adjustment; if it drifts toward HER-like behaviour, iterate alloy loading, humidity, and pulse width before increasing current density.

3.2 Interfacial NO fugacity and mass-transfer design

Despite optimising the proton budget, the dissolved NO concentration in water is only approximately 2 mM at 25 °C, which is one order of magnitude lower than the 10–50 mM coverage necessary to ensure that every catalytic site is occupied during high-current operation. Yang *et al.* addressed this deficiency by pressurising a 1 M KOH electrolyte to 5 atm NO, thereby enhancing the interfacial concentration by around tenfold.[112] This enhancement arises from Henry's Law, which dictates that the solubility of a gas in a liquid is directly proportional to its partial pressure in the gas phase, thereby allowing NO fugacity at the interface to be precisely tuned by pressure. *In situ* ATR-SEIRAS monitored a proportional rise in the NO-ad band alongside a simultaneous reduction of surface hydrogen, allowing a self-supported Cu nanowire array to maintain a 1.0 A cm^{-2} NH_3 partial current at 96% FE for 100 hours. At ambient pressure, the same electrode stabilised at 90 mA cm^{-2}. Gas-diffusion electrodes attain comparable coverages without mechanical compression: Krzywda's hollow-fibre Cu architecture reduced the gas boundary layer to less than 60 μm and achieved 0.4 mmol h^{-1} cm^{-2} NH_3 at -0.6 V_{RHE} under 10% NO, demonstrating that convective flux can replace bulk solubility.[114] Design rule 2: elevate the near-surface NO concentration to the 10–50 mM range by applying either a minimum of 5 atm overpressure or limiting gas-diffusion path lengths to 100 μm or less.

3.3 Outer-sphere capture complexes & ionic liquids

In situations where pressurisation is unfeasible, chemical carriers can provide comparable NO fugacities. Fe(II)–EDTA generates a nitrosyl adduct that elevates the apparent NO concentration to around 30 mM; when combined with a NiO nanosheet array, it yields 2.13 mmol h^{-1} cm^{-2} of NH_3 at 90% faradaic efficiency (-0.6 *vs.* RHE).[121] Xiong *et al.* replaced EDTA with ferrous citrate to mitigate interference in colorimetric NH_3 assays, achieving 65% FE at neutral pH while preserving analytical accuracy.[122] Hydrophobic ionic liquids provide an alternative approach: their minimal intrinsic proton activity inhibits the hydrogen evolution reaction, and their elevated gas affinity enhances NO concentration in the absence of water. Phosphorus-doped MoS_2 nanospheres functioning in this ionic liquid maintained a 69% faradaic efficiency at -0.6 V and exhibited sustained activity for 30 hours without pH variation.[123] Nevertheless, these strategies come with inherent trade-offs: ionic liquids often exhibit elevated viscosities that limit gas and proton transport, while outer-sphere complexes can be prone to oxidative degradation or interfere with downstream analytical assays. Design rule 3: in the absence of mechanical or convective methods, utilise outer-sphere complexes or ionic liquid solvents to increase the local NO concentration above 10 mM while preserving a proton activity within the 50–80 mV 'selectivity window'.

3.4 Electrostatic screening and double-layer structure

All NORR transition states exhibit significant dipole moments. When the electrolyte Debye length diminishes below approximately 0.5 nm (in high-salt acidic environments), the compressed electric field destabilises the dipoles, leading to surface oxidation; conversely, if it surpasses approximately 2 nm (in dilute alkaline solutions), the polar intermediates lack adequate stabilisation, resulting in an exponential decrease in the rate constant. Conducting impedance spectroscopy on pressurised KOH cells establishes the ideal screening length at 0.8–1.5 nm, a range attainable with 0.5 to 2 M supporting electrolyte concentrations or by choosing ionic liquids with cation–anion pairs that possess similar Bjerrum lengths. Design rule 4: sustain a Debye length ranging from 0.5 to 2 nm to equilibrate field stabilisation with oxidative stress mitigation. This target range overlaps with the typical screening lengths found in high-salinity environments such as seawater and industrial brines, illustrating the practicality of achieving these conditions in large-scale implementations.

4. Electrocatalytic materials and mechanistic insights

Electrocatalyst design for the nitric oxide reduction reaction (NORR) requires a precise alignment with the mechanistic and thermodynamic constraints discussed previously. Also, with performance thresholds fixed in Section 3, we can interrogate which catalyst architectures satisfy the adsorption, kinetics, and durability criteria while remaining scalable. Fig. 6 provides a schematic illustration of material classes and mechanistic modulation strategies for NO electroreduction catalysts. Each material system corresponds to distinct design approaches such as electronic structure engineering, associative pathway control, and atomically precise catalyst construction.

4.1 Bridging molecular insights with catalyst design

According to the thermodynamic analysis discussed earlier, any feasible NORR catalyst needs to meet three quantitative descriptors: (i) a nitrogen monoxide adsorption free energy within the range of $-0.45 \leq \Delta G_{NO} \leq -0.60$ eV to stabilise the precursor while preventing product inhibition; (ii) an activation barrier for the initial proton-coupled step (*NO → *NOH) below 0.45 eV to maintain a free-energy span compatible with *iR*-free cell voltages ≤ 0.60 V; and (iii) a hydrogen-evolution exchange current at least an order of magnitude smaller than the partial ammonia current, ensuring over 90% faradaic efficiency at the 300 mA cm^{-2} benchmark. Catalyst design is not merely a cataloguing task but the intentional engineering of surfaces and microenvironments that fulfil the trio of electronic, kinetic, and selectivity constraints while maintaining stability during gas-phase, membrane-mediated operation.

This section explores how five material categories (noble metals, earth-abundant transition metals, hetero-anionic compounds, single-atom motifs, and metal-free frameworks) address these descriptors. Instead of solely categorising by periodic provenance, we correlate each class with the mechanistic levers delineated in the previous section: electronic back-donation to weaken the N–O bond, bifurcation control between associative and dissociative pathways, proton management at the gas–ionomer interface, and microstructural strategies to mitigate parasitic H_2 evolution. By correlating experimentally determined ΔG_{*NO} values, turnover frequencies, and long-term stability with quantitative milestones, we elucidate which architectures approach techno-economic viability, identify persistent kinetic or durability bottlenecks, and demonstrate how solutions derived from related fields such as CO_2 electrolysis, PEM fuel cells, and ORR catalysis can bridge the remaining gaps. This framework transforms catalyst discovery from empirical enumeration to hypothesis-driven optimisation focused on the performance thresholds that will dictate commercial adoption.

4.2 Electronic and structural engineering

4.2.1 Electronic structure modulation and facet engineering. Electronic and crystallographic control over surface adsorption energetics has proven to be the most powerful lever for raising NORR activity on metallic catalysts. Early mechanistic voltammetry by de Vooys *et al.* quantified the potential-dependent selectivity window on polycrystalline noble metals,

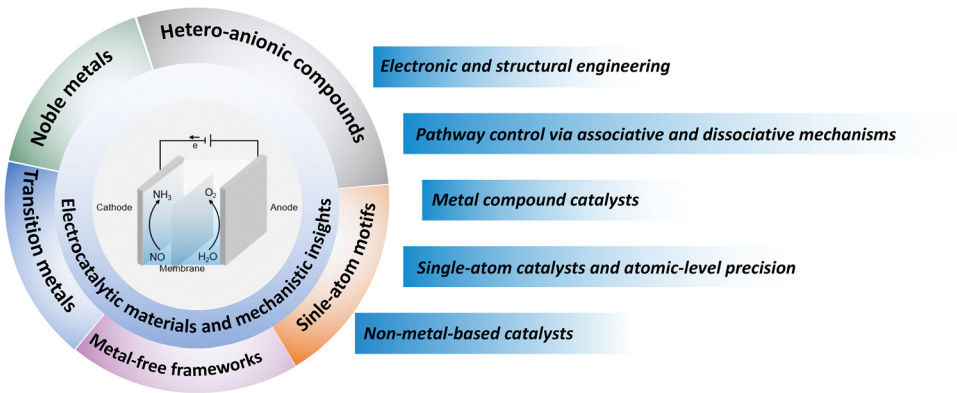

Fig. 6 Schematic summary of representative electrocatalyst classes used in NORR, including noble metals, transition metals, non-metallic frameworks, single-atom catalysts, and hetero-anionic compounds, alongside their corresponding mechanistic tuning strategies.

establishing that a low potential regime (≤ -0.2 V *vs.* RHE) favours the eight-electron transformation to NH_3, whereas intermediate potentials divert flux toward N_2 and high potentials toward N_2O.[124] Density functional plus kinetic–Monte Carlo analysis later demonstrated that on a Pt(100) terrace the barrier for the first hydrogenation (*NO → *NOH) is only 0.38 eV once a critical 0.25 ML hydrogen coverage is reached, enabling rapid N–O scission and suppressing HER.[125] These atomistic predictions are corroborated experimentally by chronoamperometry in 0.05 M H_2SO_4, where Pt(100) sustains a 25 mA cm^{-2} partial NH_3 current at −0.12 V with 82% faradaic efficiency.

The performance of noble metals significantly enhances when the local coordination and d-band centre are independent of the bulk lattice. Yu *et al.* produced plasma-etched low-coordination Ru nanosheets (Ru-LCN) that feature an open surface revealing Ru sites with a downshifted d-band centre (−2.75 eV) compared to high-coordination Ru nanosheets (Ru-HCN). At −0.20 V in neutral 0.5 M Na_2SO_4 saturated with 1% NO, the RuLCN exhibits an NH_3 production rate of 45.02 μmol h^{-1} mg_{cat}^{-1} and a faradaic efficiency of 65.9%, approximately doubling both parameters of the parent phase.[126] *Operando* FTIR reveals a twofold increase in *NOH coverage, confirming that coordinatively unsaturated Ru enhances the associative hydrogenation process (Fig. 7a).

Ligand and intermetallic approaches further refine the electronic landscape. Shi *et al.* incorporated isolated Ru into a Cu matrix through *in situ* electro-reduction of mixed hydroxides. The optimal $Ru_{0.05}Cu_{0.95}$ alloy reduces the Cu d-band centre by 0.17 eV towards the Fermi level (Fig. 7b), decreasing the *NOH formation barrier from 0.59 to 0.41 eV. In 20% NO/Ar, it attains 17.68 μmol h^{-1} cm^{-2} with 64.9% FE at −1.10 V (Ag/AgCl), surpassing monometallic Cu by an order of magnitude.[127] A more significant electronic enhancement occurs in body-centred cubic RuGa intermetallic, where electron donation from Ga produces isolated Ru^0 centres (Fig. 7c). Lu *et al.* documented an unprecedented 320.6 μmol h^{-1} mg_{Ru}^{-1} and 72.3% faradaic efficiency at −0.20 V, with density functional theory ascribing the activity to a 0.32 eV barrier for the rate-limiting *HNO → NH step.[128] The amalgamation of electron-rich Ru and a Ga framework satisfies all three descriptor criteria ($\Delta G_{NO} \approx -0.52$ eV, $\Delta G^{\ddagger} \leq 0.45$ eV, $i_{0,HER} \ll i_{NH_3}$).

Silver presents a contrasting scenario in which activity is constrained not by bond-breaking energetics but by the delivery of protons to weakly adsorbed NO. Long *et al.* illustrated on Ag(111) that reducing the applied potential from −0.20 to −0.65 V inhibits thermochemical NO coupling and sequentially alters product distribution from N_2O to NH_3 before hydrogen evolution reaction predominates.[46] Kim *et al.* surpassed the inherent proton-transfer barrier by incorporating an EDTA–Fe^{2+} outer-sphere complex that chemically sequesters NO and transmits electrons from a nanostructured Ag surface (Fig. 7d); the hybrid electrolyte maintains 50 mA cm^{-2} with approximately 100% faradaic efficiency across a voltage range of 0.04 to −0.34 V, exhibiting stability for 120 hours.[92] This example highlights that electronic optimisation must be co-designed with proton-management chemistry when the Sabatier optimum is situated on the weak-binding flank.

Among earth-abundant metals, the engineering of copper facets has yielded the most significant advancements. Xiao *et al.* isolated Cu(111) nanosheets, which exhibit σ–π back-donation that weakens the N≡O bond by 0.15 Å compared to Cu(100), resulting in a d-band centre of −2.43 eV. The nanosheets attain 371.9 μmol h^{-1} cm^{-2} and 93.2% faradaic efficiency at −0.59 V, while exhibiting less than 5% deactivation after 50 hour.[129] Shao *et al.* synthesized a porous Cu_6Sn_5 alloy that combines electronic modulation, Sn lowers the Cu d-band, with enhanced hydrophilicity, thereby shortening the diffusion pathway for NO and enabling industrially relevant current densities. Despite the system exhibiting over 96% faradaic efficiency under flow conditions, the stated NH_3 production rate of 10 mmol h^{-1} cm^{-2} at −0.23 V could not be verified against the referenced study and may represent extrapolated or inaccurately assigned values.[130] Exercise caution until performance data is independently verified. These findings validate that careful selection of facets and ligands can elevate Cu from a moderate performer to a premier NORR catalyst without the use of precious metals.

The aforementioned studies demonstrate that NORR activity follows a consistent electronic-structure continuum: strong-binding noble surfaces necessitate coordination disruption or hetero-metal dilution to desaturate NO, while weak-binding coinage and post-transition metals must facilitate enhanced proton-coupled electron transfer. Facet orientation, heteroatom alloying, and intermetallic formation each offer adjustable parameters to align ΔG_{NO} and $\Delta G^{\ddagger}$ within the optimal range (−0.45 to −0.60 eV; ≤0.45 eV). The design strategies of noble and transition metal catalysts based on electronic structure modulation and facet engineering are summarized in Fig. 7e.

The subsequent subsections analyse how defect chemistry and coordinated vacancies can further reduce the free-energy landscape.

4.2.2 Vacancy and defect engineering. Defect engineering, primarily the intentional formation of anion vacancies, has become an effective approach for modifying the adsorption energetics and reaction mechanisms of NORR catalysts. Vacancies alter the local coordination environment, displace the d-band centre, and facilitate charge redistribution, consequently reducing the free-energy span for critical hydrogenation steps while concurrently inhibiting undesirable HER kinetics. Oxygen-deficient oxides. Li *et al.* fabricated dense oxygen-vacancy layers in three-dimensional TiO_{2-x} nanoarrays grown on titanium plates through hydrogen thermal reduction. *Operando* EPR demonstrated a fourfold increase in Ti^{3+} signal intensity ($g \approx 1.985$) compared to pristine TiO_2. DFT calculations on the TiO_{2-x}(101) surface indicated that an oxygen vacancy enhances the stability of the bent-end adsorption configuration of NO by 2.1 eV and reduces the $\Delta G^{\ddagger}$ for the NH_2* → NH_3* transition state to 0.70 eV. Similarly, in NO_3RR, Li *et al.* illustrated how oxygen vacancies influence the activation of nitrogen species.[131] In a neutral phosphate buffer saturated with 10% NO_3^-, the TiO_{2-x} nanoarray produced 1.23 mmol h^{-1} cm^{-2}

(around 1233 μg h^{-1} cm^{-2}) of NH_3 with a 92.5% faradaic efficiency at −0.70 V, maintaining over 80% activity for 50 hours. Zhang *et al.* enhanced this strategy by incorporating P hetero-dopants and corresponding O-vacancies into TiO_2 nanotubes and utilising the

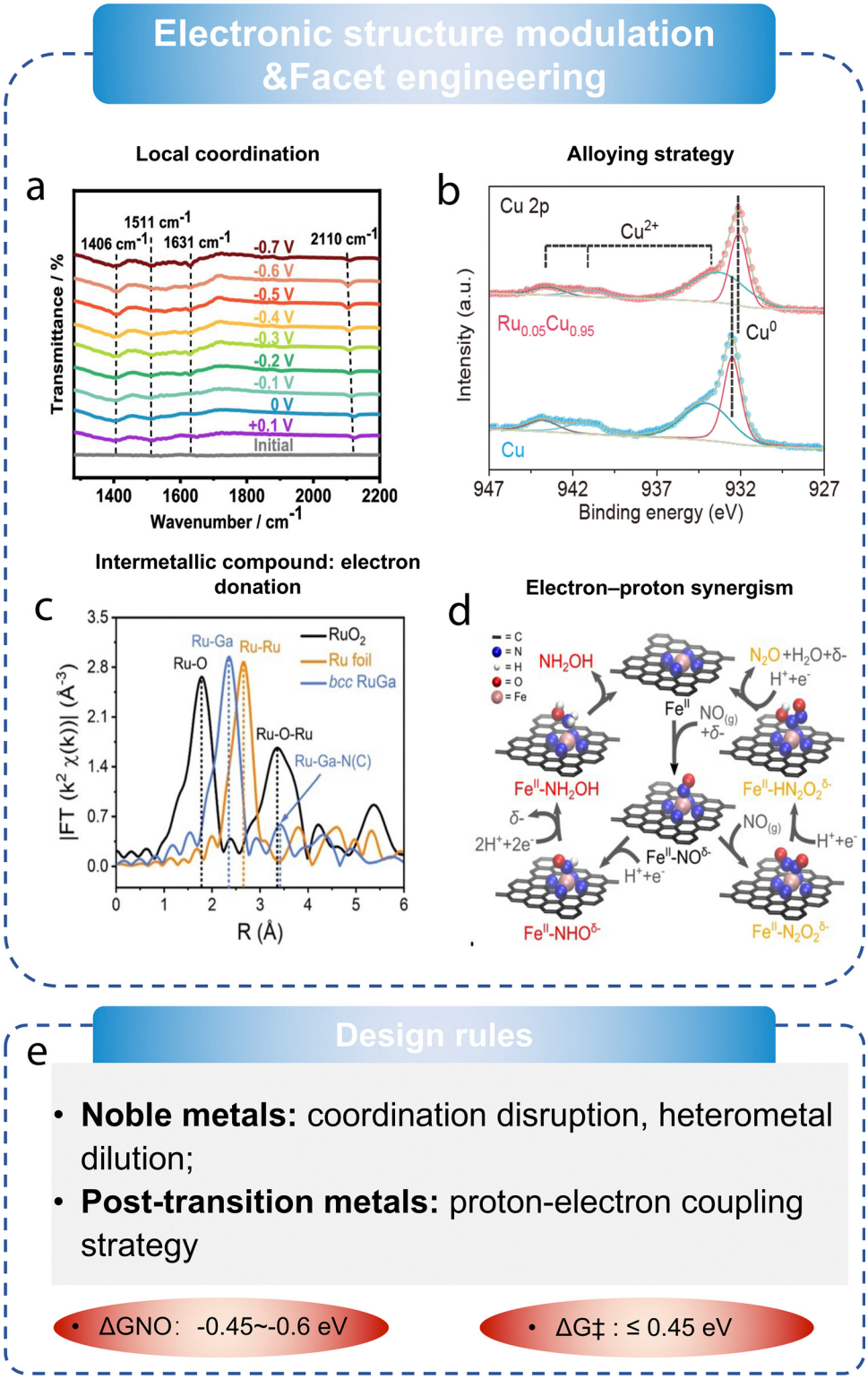

Fig. 7 (a) Potential-dependent *in situ* FTIR spectra of Ru-LCN during NORR.[126] Copyright 2022, American Chemical Society. (b) Cu 2p XPS spectra of Cu and $Ru_{0.05}Cu_{0.95}$.[127] Copyright 2021, Springer. (c) FT-EXAFS Ru K-edge absorption spectra of bcc-phase RuGa IMC. Copyright 2022, Wiley.[128] (d) Reaction mechanism and key rate-limiting intermediates of the single-atom Fe catalyst, as derived from microkinetic modeling analysis.[92] Copyright 2021, Nature. (e) Design strategies for noble and transition metal catalysts based on electronic structure modulation and facet engineering.

catalyst in a hydrophobic imidazolium-based ionic liquid. The liquid inhibited HER and stabilised NOH*, facilitating 425 μg h^{-1} $mg_{(cat)}^{-1}$ NH_3 at −0.30 V with 89% FE.[132]

Vacancy engineering is equally effective in high valent manganese oxides. MnO_{2-x} nanowires grown on Ti mesh, synthesised *via* hydrothermal methods followed by controlled annealing, exhibit oxygen-vacancy densities of 9.2% as quantified by XPS Vo peak deconvolution (Fig. 8a). These vacancies modulate the Mn 3d–O 2p hybridisation and stabilise the NO adsorption state with ΔG_{NO} = −0.57 eV, aligning with the Sabatier optimum. At −0.70 V *vs.* RHE in 0.2 M Na_2SO_4 saturated with 10% NO, the catalyst achieves 27.5 × 10^{-1} mol s^{-1} cm^{-2} NH_3 (≈0.99 mmol h^{-1} cm^{-2}) and 82.8% faradaic efficiency, more than doubling the turnover frequency of pristine MnO_2. DFT calculations confirmed that oxygen vacancies lower the activation barrier for the NOH to NH* transition, while long-term electrolysis (>30 h) showed minimal degradation (Fig. 8b).[133]

4.2.2.1 Phosphate vacancies. CoP nanowire arrays grown on Ti mesh show excellent performance in NO electroreduction. Liang *et al.* found that the catalyst achieves 47.2 μmol h^{-1} cm^{-2} NH_3 at −0.20 V, with 88.3% FE and minimal degradation over 14 hours. DFT studies confirmed end-on NO adsorption on the CoP(111) facet, with ΔG_{NO} ≈ −0.54 eV and a low NOH formation barrier of 0.05 eV.[47] Analogous FeP nanorods on carbon cloth achieve 85.62 μmol h^{-1} cm^{-2} and 88.49% FE under identical conditions in 0.2 M phosphate buffer.

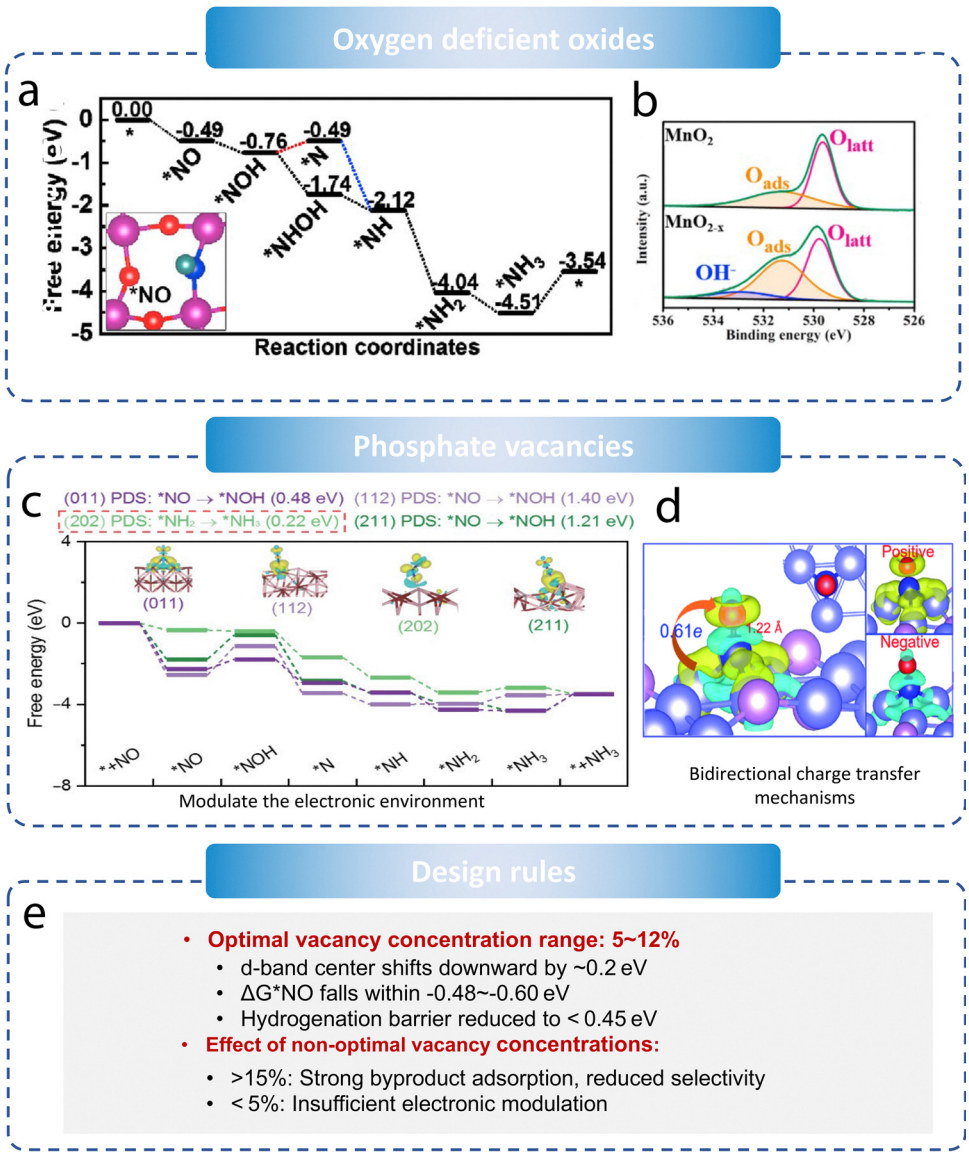

Fig. 8 (a) O 1s regions of MnO_2 and MnO_{2-x}.[133] Copyright 2022, Elsevier. (b) Free energy diagrams of NORR on MnO_{2-x}(211) surface along distal and alternating pathways.[133] Copyright 2022, Elsevier. (c) Free energy diagrams of the electrocatalytic NORR on FeP(011), (112), (202), and (211) surfaces.[134] Copyright 2022, Spinger. (d) Differential charge density of adsorbed NO* on the Ni_2P(111) surface.[134] Copyright 2022, Spinger. (e) Design principles of catalysts based on vacancy and defect engineering.

Phosphorus vacancies alter the electronic environment, resulting in $\Delta G_{*NO} \approx -0.49$ eV and reduced HER (Fig. 8c).[134] Mou *et al.* found that Ni_2P nanosheet arrays on carbon paper, with both P-vacancies and Ni^{3+} edge sites, show bidirectional charge transfer mechanisms (Fig. 8d). At −0.20 V in 0.1 M HCl, the system produced 33.47 μmol h^{-1} cm^{-2} NH_3 with 76.9% FE.[134]

4.2.2.2 Design rules emerge from vacancy chemistry. Across oxides and phosphides, a unifying trend is observed: anion-vacancy concentrations of 5–12% shift the d-band centre by ∼0.2 eV, set ΔG_{*NO} within the −0.48 to −0.60 eV window and reduce the rate-limiting hydrogenation barrier below 0.45 eV. Higher vacancy fractions (<15%) can cause strong chemisorption of oxygenated byproducts, while lower fractions do not reach the Sabatier optimum. Fig. 8e summarises the catalyst design principles and key parameters based on vacancy and defect engineering. Future research should use *operando* X-ray absorption and vacancy-controlled synthesis (*e.g.*, pulsed plasma, lattice-strain engineering) to stabilise defect densities under industrially relevant 300 mA cm^{-2} conditions.

4.3 Pathway control *via* associative and dissociative mechanisms

4.3.1 Dissociative pathway catalysts. The dissociative reduction of nitric oxide occurs through immediate N–O bond cleavage upon adsorption, resulting in surface-bound N* and O* intermediates that are then hydrogenated. This pathway avoids the formation of NOH* or HNO* intermediates and is preferred on catalysts with strong back-donation for bond weakening.[135,136] Early-transition metal carbides and nitrides, including WC, Mo_2C, and WB, may allow for low-barrier N–O bond cleavage due to their high density of d-states near the Fermi level and strong metal–NO orbital interactions, according to first-principles calculations. Direct NO-specific DFT studies on these materials are limited, with cleavage barriers below 0.5 eV extrapolated from related reactions or hypothetical surfaces. Until such systems are explicitly evaluated under realistic adsorbate configurations, this mechanistic hypothesis should be considered provisional and prioritised in future computational work. Research suggests that back-donation into NO antibonding orbitals weakens the N–O bond and promotes dissociative adsorption.[137,138] The (111) surface of WB stabilises NO dissociation with an activation energy of 0.42 eV, keeping ΔG_{NO} within the optimal −0.50 to −0.60 eV range. The resulting N and O* species undergo classical distal or alternating hydrogenation steps. However, the strong binding of O* ($\Delta G > -1.0$ eV) requires either co-catalytic oxygen scavengers or pulsed regeneration protocols to maintain turnover.

A related approach uses dual-site motifs, like Fe–Mo pairs embedded in sulfur-defective MoS_2. Chen *et al.* created atomically Fe-doped MoS_{2-x} with cooperative interactions between Fe–Mo dual sites. Fe centres reduced the N–O bond cleavage barrier, while Mo stabilised the N* intermediate. *Operando* XPS confirmed the transient appearance of Fe^{2+} and Mo^{4+} during NO activation, with ammonia yields reaching 288.2 μmol h^{-1} cm^{-2} at −0.6 V and a faradaic efficiency of 82.5%. DFT simulations attributed the high activity to a dissociative NO adsorption mechanism involving alternating hydrogenation steps that completely bypassed the NOH* intermediate.[139] These findings imply that the dissociative mechanism may be most useful on materials capable of stabilising atomic nitrogen while tolerating strongly bound oxygen. Design efforts can prioritise the development of multi-electron active sites and the incorporation of oxygen-buffering co-catalysts such as CeO_2 or perovskite-type oxides to ensure prolonged operation under steady-state or pulsed electrolysis conditions, based on principles from oxygen-evolving and oxidation-tolerant systems.

4.3.2 Associative pathway catalysts. The associative pathway maintains the N–O bond through the first proton-coupled electron transfer, resulting in NOH*, HNO*, or NH_2OH* intermediates before cleavage. On moderate-binding surfaces, the associative route shortens the overall free-energy span by stabilising polar NOH*, HNO*, and NH_2OH* intermediates while avoiding strongly bound O*, which hinders dissociative catalysis. Tuning ΔG_{*NO} to the −0.40 to −0.55 eV window results in quasi-equilibration of the first proton-coupled electron-transfer, with a theoretical Tafel slope close to 60 mV dec^{-1}.[46] Cu exhibits associative catalysis, with detailed DFT and *operando* spectroscopic studies confirming a stepwise NOH* → HNO* → NH_2OH* pathway. While Ag has weak *NO binding, which may favour similar intermediates, experimental validation has thus far been limited to modified systems based on outer-sphere complexes. The constant-potential DFT on Cu(111) predicts a barrier of 0.42 eV between NO and NOH, followed by a 0.38 eV step from NOH* to HNO*. Cu foil maintains >80% FE_NH_3 between −0.15 and −0.35 V, with *operando* ATRSEIRAS detecting a NOH* band at ∼1640 cm^{-1} that diminishes as NH_2OH* appears at ∼1550 cm^{-1}, confirming sequential hydrogenation.[126] While Ag has been investigated for NORR due to its weak *NO binding and low HER activity, most reported improvements come from modified systems. Kim *et al.* found that adding an EDTA–Fe^{2+} outer-sphere complex to a nanostructured Ag electrode result in near-quantitative selectivity under neutral conditions. While unmodified Ag foil has not demonstrated high faradaic efficiency or *operando* vibrational signatures comparable to Cu, Ag systems modified with outer-sphere complexes such as EDTA–Fe^{2+} highlight how weak-binding surfaces can be co-engineered to promote associative NO reduction pathways under mild conditions. Proton delivery often restricts coinage metal selectivity. The researchers addressed the bottleneck by using an outer-sphere EDTA–Fe^{+} complex to capture NO in solution and transport electrons from a nanostructured Ag cathode. The hybrid system maintains 50 mA cm^{-2} at −0.17 V with approximately 100% faradaic efficiency for 120 hours.[108] Outer-sphere transfer reduces the activation barrier for *NOH formation by approximately 0.15 eV by avoiding the entropic penalty of surface adsorption, according to DFT calculations.

4.4 Metal compound catalysts

As a logical extension of the bifurcated mechanistic routes discussed in Section 4.3, metal compound catalysts provide a

structurally and electronically diverse platform for selectively expressing either associative or dissociative NO reduction pathways. These compounds, which frequently exhibit tuneable surface terminations, lattice strain, or vacancy configurations, modulate the reaction coordinate in ways that correspond directly to the elementary steps outlined for NORR. For example, oxygen vacancies in oxides promote dissociative cleavage of the N–O bond, whereas hetero-anionic phosphides or sulphides promote stepwise hydrogenation *via* stabilised NOH* and HNO* intermediates. As a result, the materials discussed in this section are not only organised by chemical identity but also serve as archetypes for how structural control dictates mechanistic expression, providing experimental validation of the theoretical constructs introduced previously.

The mechanistic divergence described in Section 4.3 between associative and dissociative NORR pathways governs not only the kinetic profile of NO conversion but also closely aligns with the electronic structure and bonding environments provided by compound catalysts. Metal oxides, phosphides, sulphides, and carbides have unique orbital hybridisations, vacancy chemistries, and lattice-induced field effects that selectively stabilise either intact intermediates (NOH* and NH_2OH*) or dissociated fragments (N* and O*). For example, oxygen-deficient oxides and sulphides frequently lower the activation barrier for NO cleavage, favouring dissociative routes. In contrast, hetero-anionic systems such as phosphides modulate the proton–electron transfer energies required for associative hydrogenation. As a result, the catalyst classes examined in this section are not arbitrarily grouped, but rather reflect underlying mechanistic tendencies, demonstrating how structural motifs influence pathway selection and catalytic efficiency under realistic NORR conditions.

As defined in Section 3.5, all catalyst classes considered here are evaluated against three key molecular descriptors: ΔG_{*NO} adsorption between −0.45 and −0.60 eV, an activation barrier for *NO → *NOH below 0.45 eV, and a hydrogen evolution exchange current at least tenfold lower than the ammonia partial current. Rather than restating these metrics throughout, we now analyse how each material family aligns with or diverges from these thresholds.

This distinction is frequently corroborated by *operando* FTIR spectroscopy, which identifies transient vibrational features attributable to NOH*, HNO*, and related intermediates. For example, in Ru-LCN, Co_1/MoS_2, and Cu_1/MoS_2 systems, detection of bands in the 1550–1650 cm^{-1} range confirms stabilisation of key associative intermediates, validating DFT predictions and reinforcing the pathway assignments.[126,139,140] These observations link spectroscopic signatures directly to mechanistic function, providing a critical diagnostic tool in determining how catalysts navigate the NO reduction network.

The concurrent modulation of NO adsorption and hydrogen evolution dynamics by the same electronic or structural feature is a recurring theme in a variety of systems, including Bi nanodendrites,[141] Sb-doped MoO_3,[142] Ni@NC,[143] Fe_1/MoS_{2-x},[144] and W_1/MoO_{3-x}.[145] Electron-rich p-block dopants, encapsulating carbon frameworks, and vacancy-rich oxides are examples of design elements in these catalysts that promote NO activation while inhibiting competing hydrogen evolution pathways. The coupling effect is caused by a unified modulation of the local electronic environment, which lowers the energy barrier for NORR intermediates and disfavours H* adsorption or proton-coupled electron transfer to H_2. Recognising this synergy allows for more rational integration of HER resistance and NORR activity in future catalyst design, especially for systems operating at high current densities or with fluctuating gas compositions.

4.4.1 Noble metal catalysts. Noble metals (*e.g.*, Pt, Au, Pd, Ru, and Ag) have received extensive attention in NORR due to their high conductivity and efficient electron-transfer kinetics. However, *NO and other intermediates have different adsorption energies, resulting in diverse product selectivity.[146] Vooys *et al.*[124] found that the product distribution of NO electroreduction on Ru, Rh, Ir, Pd, Pt, and Au is highly dependent on the applied potential. Low potentials favour NH_3 formation, intermediate potentials produce N_2, and high potentials promote N_2O formation. Strong metal–hydrogen bonds frequently enable competitive HER.

Crystal facet engineering has been used to enhance catalytic performance. Chun *et al.* used DFT and kinetic Monte Carlo simulations to study Pt(100) surfaces in acidic media. They found that the barrier for *NO to *NOH is only 0.38 eV. This promotes efficient N–O bond cleavage while preventing the formation of N_2 and N_2O.[125] Long *et al.* found that Ag(111) shifts product selectivity from N_2O to NH_3 and then to H_2 as the potential decreases (Fig. 9a). The electrochemical protonation step governed NH_3 formation, with HER becoming significant below −0.65 V.[102] Yu *et al.* plasma etched high-coordinate Ru-HCN nanosheets to prepare low-coordinate Ru-LCN, which reduced costs and increased active site exposure. At −0.2 V, these catalysts achieved 65.96% FE and 45.02 μmol h^{-1} mg^{-1} yield, which increased to 80.2 μmol h^{-1} mg^{-1} in flow operation.[126] *Operando* FTIR confirmed an alternating associative pathway.

Kim *et al.* improved NO capture by combining a nanostructured Ag electrode with an EDTA–Fe^{2+} complex (EFeMC).[108] The electrolyte absorbs NO, and the Ag electrode transfers electrons to regenerate EFeMC and produce NH_3. This system provided ∼100% FE at 50 mA cm^{-2} across 0.04–0.34 V and remained stable for 120 hours. Donor–acceptor interactions between Ag and oxygen atoms in anchored intermediates improve intermediate stability.

4.4.2 Non-noble metal catalysts. Non-noble metals offer low-cost alternatives with superior performance. Long *et al.* used DFT to screen transition metals and found Cu to have the best *NO adsorption energy (Fig. 9b).[46] Cu(111) has high barriers for N–N and H–H coupling, preventing the formation of N_2 and H_2 molecules. Porous Cu foam produced 517 μmol h^{-1} mg^{-1} and 93.5% FE at −0.9 V.[46] Xiao *et al.* found that Cu(111) nanosheets outperform (100) facets, achieving 371.89 μmol cm^{-2} h^{-1} and 93.19% FE at −0.59 V.[147] ATR-IRAS and DFT analysis revealed σ–π donation from Cu to NO, weakening the N≡O bond (Fig. 9c).

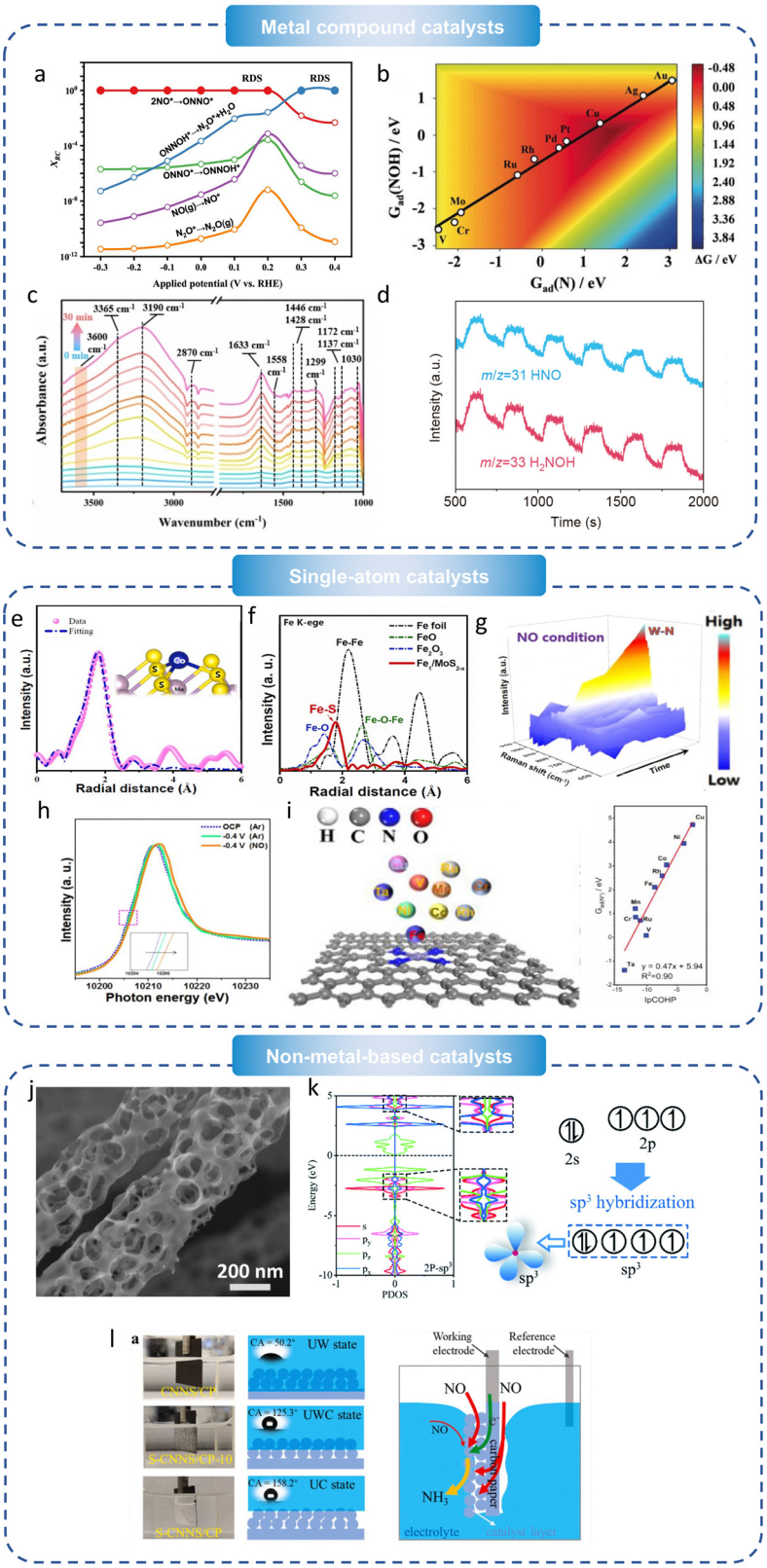

Fig. 9 (a) Nitrogen reduction products under different operating potentials.[125] Copyright 2021, American Chemical Society. (b) Two-dimensional activity map for ammonia production on different metal catalysts, with all reaction free energies calculated at 0 V *vs.* RHE.[46] Copyright 2020, Wiley. (c) *In situ* ATR-IRAS spectra of electrocatalytic NO reduction at −0.59 V *vs.* RHE in 0.1 M K_2SO_4 electrolyte.[147] Copyright 2024, Wiley. (d) Online DEMS easurements of $Ru_{0.5}Cu_{0.5}$ during NORR.[127] Copyright 2021, Spinger. (e) EXAFS Fitting curve of Co_1/MoS_2.[155] Copyright 2023, Elsevier. (f) EXAFS spectra of Fe_1/MoS_{2-x} and reference samples of Fe foil, FeO and Fe_2O_3.[144] Copyright 2023, Elsevier. (g) Time-dependent *operando* Raman spectra of W_1/MoO_{3-x} under NO conditions at −0.4 V.[145] Copyright 2023, American Chemical Society. (h) Potential-dependent *operando* W L_3-edge XANES.[145] Copyright 2023, American

Chemical Society. (i) Correlation curve between the integrated crystal orbital Hamilton population (ICOHP) of TM–N_4 and the adsorption free energy of nitrogen species (G_{ads}(N*)).[158] Copyright 2023, Elsevier. (j) SEM image of HCNF.[160] Copyright 2023, Elsevier (k) PDOS of 2P@C_2 society N and electronic configuration showing orbital hybridization between sp^3 atoms and sp^2/sp^3 orbitals.[163] Copyright 2021, Royal Society of Chemistry. (l) Photographs and water contact angles of the distinct electrodes and illustrations of underwater UW, UWC, and UC statess and Schematic illustration of the gas–liquid–solid triphase interface electrocatalysis with UWC state[167] Copyright 2023, Elsevier.

Cu–Sn alloys like Cu_6Sn_5 are efficient at industrial scales. Shao *et al.* demonstrated >96% FE and 10 mmol h^{-1} cm^{-2} at 1400 mA cm^{-2}.[130] DFT and TEM demonstrated improved NO protonation and resistance to oxidation. Wu *et al.* engineered Cu@Co catalysts with interfacial strain to improve NO adsorption and lower the NO–NOH barrier.[148] This yielded 627.2 μg h^{-1} cm^{-2} at 76.54% FE. When used in Zn–NO batteries, it produced 3.08 mW cm^{-2} and 273.37 μg h^{-1} cm^{-2}.

Other non-noble metals have yielded promising results. Wang *et al.* produced hcp-Co nanosheets that outperformed fcc-Co, yielding 439.5 μmol cm^{-2} h^{-1} at 72.6% FE.[62] Cheon *et al.* utilised zero-valent Fe/C to attain 96% FE at 1% NO and 1239 μmol h^{-1} cm^{-2} at 10% NO.[70] Zhao *et al.* investigated Ni single-crystal facets and discovered that Ni(210) provides almost 100% FE.[70] Ni@NC, synthesised *via* co-precipitation and graphitisation, achieved 34.6 μmol cm^{-2} h^{-1} at 72.3% FE and resists dissolution in acid.[143] p-Block metals provide HER suppression.[149] Bi nanodendrites produced 1194 μg h^{-1} mg^{-1} with 89.2% FE.[141] Bi@C achieved 1592.5 μg h^{-1} mg^{-1} at 93% FE.[150] Sb_1/a-MoO_3 stabilised *NO and suppressed HER, yielding 273.5 μmol h^{-1} cm^{-2} and 91.7% FE.[142]

4.4.3 Metal alloys and intermetallic compounds. Alloying noble and non-noble metals provides synergistic control over *NO adsorption, NOH formation, and proton supply. Shi *et al.* produced $Ru_{0.05}Cu_{0.95}$ alloys through *in situ* electroreduction.[127] Ru doping shifted Cu's d-band and reduced hydrogenation barriers, resulting in 17.68 μmol h^{-1} cm^{-2} at 64.9% FE. DEMS confirmed the alternating associative mechanism (Fig. 9d). Lu *et al.* created bcc RuGa intermetallic, resulting in isolated Ru^0 centres. These produced 320.6 μmol h^{-1} mg^{-1} and 72.3% FE at −0.2 V.[128] The Ga matrix shifted Ru from fcc to bcc, promoting electron transfer and lowering the *HNO/NH barrier to 0.32 eV.

Cu–Sn alloys, such as Cu_6Sn_5, show industrial scalability, with >96% FE and 10 mmol h^{-1} cm^{-2}.[130] DFT revealed lower NO protonation barriers. Wu *et al.* used tensile strain at the bimetallic interface to enhance NO adsorption, resulting in 627.2 μg h^{-1} cm^{-2} at 76.54% efficiency[148] Zn–NO battery integration resulted in 3.08 mW cm^{-2} power density and 273.37 μg^{-1} cm^{-2} NH_3 yield.

Phosphides promote metal–nonmetal synergy. CoP nanowires grown on Ti mesh showed ultra-low onset (−0.012 V) and produced 47.22 μmol^{-1} cm^{-2} NH_3 at 88.3% efficiency.[47] FeP nanorods on carbon cloth demonstrated 85.62 μmol h^{-1} cm^{-2} and 88.49% efficiency.[134] Ni_2P nanosheets used bidirectional charge transfer to achieve 33.47 μmol h^{-1} cm^{-2} at 76.9% FE. Zn–NO batteries generated 1.53 mW cm^{-2} and 62.05 mg h^{-1} mg^{-1} NH_3.[151]

Sulphides use defect engineering to activate NO. TiS_2(011) elongates the N–O bond *via* end-on adsorption, yielding 153.8 μmol h^{-1} cm^{-2} with 91.6% F.[152] P–MoS_2 nanospheres produced 388.3 μg h^{-1} mg^{-1} NH_3 in ionic liquids[123] Fe_1/MoS_{2-x} with sulphur vacancies achieved 288.2 μmol h^{-1} cm^{-2} and 82.5% efficiency.[144] CoS_{1-x} achieved 44.67 μmol h^{-1} cm^{-2} at 53.6% FE,[153] while SnS_{2-x} with dual Sn-VS sites achieved 78.6 μmol h^{-1} cm^{-2} and 90.3% FE.[149] These catalysts show that rational design of metal alloys and intermetallics, including electronic tuning, facet exposure, strain engineering, and defect incorporation, can improve NORR selectivity and activity while lowering noble metal content.

4.5 Single-atom catalysts and atomic-level precision

Single-atom catalysts (SACs), with their maximised atom utilisation, highly dispersed active sites, and tuneable coordination structures, have emerged as a potent class of materials for NORR. SACs isolate metal atoms on conductive supports, allowing for fine adjustment of adsorption energies, lower reaction barriers, and control of proton–electron transfer steps while suppressing HER and N_2O formation. Research focuses on transition metal SACs anchored on MoS_2, doped carbons, and defective oxides, supported by DFT, *in situ* spectroscopy, and advanced microscopy techniques.

4.5.1 Transition-metal decorated layered chalcogenide. Chen and coworkers showed that anchoring isolated Co atoms on MoS_2 basal planes results in a Co–S_3 motif (Co–S distance 2.19 Å, EXAFS) (Fig. 9e).[140] Co_1/MoS_2 produced 217.6 μmol h^{-1} cm^{-2} NH_3 at 87.7% FE in 0.5 M Na_2SO_4 at −0.5 V *vs.* RHE.[154] DFT analysis shows that pristine MoS_2 has a 0.80 eV barrier for *NO adsorption. However, Co incorporation makes *NO binding exergonic (ΔG = −0.12 eV), shifting the rate-determining step to *NOH formation with a lower barrier of 0.48 eV. The *operando* FTIR at 1850 cm^{-1} confirmed the DFT-predicted intermediate landscape and explained a 35% increase in partial current density.

In parallel, the Cu_1/MoS_2 SAC with the same S_3 coordination achieved 337.5 μmol h^{-1} cm^{-2} NH_3 at 90.6% FE at −0.6 V.[155] Combined *operando* FTIR (peaks at 1660 cm^{-1} for *HNO and 1620 cm^{-1} for *NOH) and DFT revealed a mixed associative/dissociative pathway where *NO protonation to *HNO (E_a = 0.54 eV) competes with direct NO–H coupling to *NOH (E_a = 0.58 eV). The single Cu site effectively suppresses HER by limiting surface proton coverage ($\theta_H \leq 0.12$ at −0.6 V), even at 150 mA cm^{-2}. This finding suggests that using the right metal and support can decouple NO hydrogenation from competing hydrogen evolution at industrially relevant current densities.

Fe_1/MoS_{2-x} extends the chalcogenide platform by integrating atomic Fe into sulfur-vacancy-rich MoS_2.[144] EXAFS confirms Fe–Mo dual sites (Fig. 9f). DFT coupled with molecular dynamics shows these sites stabilise *NO (ΔG_{ads} = −0.22 eV) while lowering the N–O cleavage barrier by 0.35 eV relative

to Fe–S coordination. At −0.6 V, this catalyst produced 288.2 μmol h^{-1} cm^{-2} NH_3 with 82.5% FE. Time-resolved *in situ* Raman (M–N stretch at 575 cm^{-1}) captured rapid NO dissociation, demonstrating how vacancy engineering can anchor and activate NO for hydrogenation. This study suggests a general strategy for optimising multi-step reaction sequences: create proximal hetero-metal pairs to overcome the nitrite-desorption bottleneck *via* dual-site synergy.

4.5.2 Oxide and vacancy-engineering. Atomically dispersed W in an amorphous MoO_{3-x} matrix (W_1/MoO_{3-x}) forms W–O_5 motifs that perform two critical functions simultaneously: electron back-donation into NO π* orbitals (lowering the limiting potential by ∼120 mV) and catalytic H_2O dissociation to supply protons *in situ*.[145] Under −0.4 V *vs.* RHE, this dual-function SAC achieved 308.6 μmol h^{-1} cm^{-2} NH_3 at 91.2% FE. *In situ* Raman (broad band at 950 cm^{-1} for *OOH intermediates) (Fig. 9g) and X-ray absorption spectroscopy (W–O bond length ≈1.80 Å) (Fig. 9h) revealed a direct correlation between local proton-generation activity and increased intermediate coverage. This approach addresses the mass-transport limitation of protons in aqueous media and provides a blueprint for integrating proton sources into the active site. This insight can be applied to other electrocatalytic reductions, such as CO_2RR, where local proton availability is rate-limiting.

4.5.3 Carbon-supported heteroatoms. Atomic-site migration and metal leaching present a unique durability challenge in acidic NORR. Peng *et al.* addressed this by embedding single Nb atoms into a boron- and nitrogen-co-doped porous carbon scaffold, forming covalent Nb–B_2N_2 centres (Nb–N 1.98 Å and Nb–B 2.05 Å by FT-EXAFS).[156] In 0.1 M HCl at −0.5 V, this Nb SAC produced 8.2 × 10^{-8} mol cm^{-2} s^{-1} NH_3 (approximately 295 μmol h^{-1} cm^{-2}) with >87% FE and maintained >95% activity for 15 hours. Covalent Nb–ligand bonds prevent metal aggregation or loss during long-term operation. This design principle, which employs heteroatom-doped carbon to form strong, non-labile bonds with single atoms, can be applied to other challenging environments, such as alkaline media or flow reactors, to ensure long-term performance.

4.5.4 Theoretical coordination frameworks and descriptor development. Beyond experimental demonstrations, theoretical frameworks provide a rational basis for SAC design and high-throughput screening. Yao *et al.* proposed a two-step self-regulation model for graphene vacancies: initial vacancy formation thermodynamically stabilises TM atoms, while adsorbate-assisted vacancy migration dynamically adapts the coordination shell under reaction conditions, lowering activation energies by up to 0.42 eV and maintaining atomic dispersion.[157] Wang and colleagues conducted a comprehensive DFT survey of TM–N_4 SACs (TM = V, Cr, Mn, Fe, Co, Ni, Cu, Ru, Rh, Ta).[158] They established a linear scaling relation between integrated crystal orbital Hamilton population (ICOHP) and ΔG_{ads}(N*) (Fig. 9i). This descriptor identified Fe–N_4 as the optimal motif for balancing N-binding strength and HER suppression. Wu *et al.* used spin-polarized DFT and Bader charge analysis to show that Cu@g-C_3N_4 has a limiting potential of 0.371 V due to interfacial charge transfer (+0.62*e* on Cu), resulting in high NH_3 selectivity.[159] Theoretical studies can provide a road map for future SAC discovery: identify coordination motifs that optimise adsorption energetics using ICOHP or related electronic descriptors, then stabilise them using dynamic, self-healing vacancy architectures or strong heteroatom–metal covalent bonds.

When comparing single-atom catalysts to vacancy- and intermetallic-based designs, both strategies aim for the same fundamental goal: precise modulation of the NO adsorption environment while simultaneously suppressing HER. However, they used different structural paradigms. SACs isolate sites using tailored coordination environments on supports like MoS_2 or doped carbon. This creates uniform active centres that minimise hydrogen affinity while stabilising key NORR intermediates. Intermetallic and vacancy-engineered compounds, on the other hand, achieve similar control through ensemble effects, which involve modifying the electronic density of states, lattice strain, or charge transfer to optimise reactivity across a larger, often cooperative surface. Single-atom catalysts excel in atom economy and mechanistic specificity, but their synthesis and stability under industrial conditions are challenging. Intermetallic and vacancy-based systems, while occasionally less selective, provide greater scalability and structural robustness. A comparative understanding of these approaches enables researchers to navigate the trade-offs between molecular precision and device-level practicality, potentially designing hybrid systems that benefit from the advantages of both regimes.

4.6 Non-metal-based catalysts

Because of their abundant availability and low cost, nonmetal-based materials provide compelling advantages for scalable electrochemical ammonia synthesis. Metal-free carbon frameworks, particularly those incorporating p-block elements or engineered heteroatoms, have emerged as promising candidates for NO electroreduction, with increasing experimental and theoretical evidence demonstrating their catalytic potential in mild, aqueous conditions. Ouyang *et al.*'s early experimental work demonstrated the effectiveness of structured carbon nanomaterials. A honeycomb-like carbon nanofiber catalyst (Fig. 9j), fabricated *via* electrospinning and calcined at 800 °C, exhibited a yield of 22.5 μmol^{-1} cm^{-2} and a faradaic efficiency of 88.3% at −0.6 V in 0.2 M Na_2SO_4 under a NO/Ar gas mixture (1 : 3).[160] This high selectivity is attributed to the honeycomb structure's hierarchical porosity, which increases electrochemically active surface area and allows for NO gas capture *via* interconnected nanocavities. Surface hydroxyl groups aid in NO adsorption and hydrogenation, reducing energy input and increasing selectivity.

Because of its large surface area, electrical conductivity, and tuneable electronic structure, graphene, particularly in its nitrogen- and boron-doped forms, serves as the prototypical platform. Saeidi *et al.* found that adding silicon to N_4 graphene (Si–N_4Gr) reduces the limiting potential to 0.56 V and promotes NH_3 formation at low NO surface coverage, while higher coverages favour N_2 evolution.[161] This dual-pathway modulation emphasises the importance of NO surface coverage in determining selectivity outcomes. Zhao *et al.* used spin-

polarized DFT to show that boron doping in graphene improves HNO* intermediate stabilisation, lowers the energy barrier for NO reduction, and allows for electrocatalysis at a limiting potential as low as −0.35 V.[162] The intermediate (HNO*) also has a coupling site for N_2O formation, highlighting the importance of intermediate binding energies in determining selectivity bifurcations.

Recently, the development of heteroatom-doped, extended carbon frameworks has expanded the non-metallic catalyst landscape. Wu *et al.* proposed a phosphorus-doped monolayer C_2N system (2P@C_2N) with sp^3-hybridized phosphorus centres that promote strong NO adsorption and a high turnover frequency of 8.9×10^5 s^{-1} per site at 400 K, surpassing Pt(111) benchmarks (Fig. 9k).[163] Zang *et al.* improved on this design by combining dual-atom motifs with p-orbital dopants, resulting in cooperative activation of NO *via* synergistic orbital overlap and reinforcing the utility of co-doping strategies for increasing selectivity and reaction rates.[164] The wide-bandgap graphene analogue, hexagonal boron nitride, only shows NORR activity when doped. Mudchimo *et al.* demonstrated that carbon-doped armchair-edged boron nitride activates NO *via* exposed boron edge sites, allowing for spontaneous NO-to-NH_3 conversion at zero overpotential and a low kinetic barrier of 0.83 eV.[165] However, undoped hexagonal boron nitride basal planes have insufficient NO adsorption, as evidenced by follow-up studies. Carbon doping provides favourable adsorption energies and low limiting potentials (0.28 V at C sites; 0.35 V at B sites), whereas O-doped variants bind NO too strongly, preventing further hydrogenation steps.[166] These results demonstrate the delicate Sabatier balance required: excessively strong adsorption impedes intermediate turnover, whereas weak adsorption reduces site occupation and activity.

Graphitic carbon nitride (g-C_3N_4) exhibits NORR activity in both pristine and doped forms. Li *et al.* used carbon paper to support g-C_3N_4 nanosheets (CNNS/CP), achieving 15.1 μmol h^{-1} cm^{-2} NH_3 with 41.5% faradaic efficiency at −0.6 V.[167] Hydrophobic modification of the catalyst surface enhances gas–liquid–solid three-phase interfaces and doubles NH_3 output, highlighting the significance of interfacial mass transfer and microenvironmental tuning in NORR systems (Fig. 9l). Saeidi *et al.* studied boron-doped monolayer C_3N structures and found that substitutional BC and BN motifs are active NO adsorption sites. DFT calculations revealed strong B-vacancy bonding, which improves both adsorption energy and electron transfer, thereby stabilising the catalytic framework under reaction conditions.[168] Nulakani *et al.* embedded B_4 clusters into g-C_3N_4 nanosheets (B_4@g-C_3N_4) and found adsorption energies of −1.15 eV and −2.46 eV for N-terminal and side configurations, respectively.[169] The limiting potential decreases from −0.29 V in gas to −0.10 V in solvent, with charge-state modulation improving kinetic favourability and selectivity. This emphasises the importance of the local dielectric environment and electrostatic tuning in maximising catalyst performance.

When combined, nonmetal-based catalysts provide a promising and cost-effective route to selective NORR catalysis. They meet the mechanistic criteria outlined in Section 3, including tuning ΔG_{NO} and limiting overpotentials without strong HER competition. Their modularity, dopability, and interfacial versatility indicate compatibility with advanced reactor designs like gas diffusion electrodes and hybrid solid–liquid electrolytes. To advance these metal-free systems from theoretical constructs to practical NORR platforms, theory-guided descriptor screening and *operando* validation must be integrated further.

Despite the promise demonstrated by the non-metallic and metal-free systems discussed in this section, it is essential to note that many of these catalysts are based on theoretical projections or low-throughput laboratory evaluations. Doped carbon frameworks, boron nitride variants, and g-C_3N_4 structures offer clear pathways towards low-cost and scalable NORR platforms. Representative catalysts and key metrics are summarised in Table 1. However, their catalytic mechanisms are often derived from DFT predictions with limited experimental corroboration under *operando* or industrially relevant conditions. To bridge this gap, systematic benchmarking, durability testing, and real-time spectroscopic validation will be required to ensure that predicted selectivity and turnover rates can be reliably achieved at scale. Until then, the potential of these systems is strong but provisional, emphasising the importance of concurrent development in both computational discovery and experimental validation.

4.7 Forward-looking catalyst development strategies

In addition to the mentioned descriptors, future catalyst development should specifically focus on underexplored areas that exhibit considerable potential when aligned with *operando* insights and techno-economic requirements. Specifically, three forward-looking strategies emerge to form a cohesive forward-looking agenda: real-time adaptability, combined structural and site-specific engineering, and explicit interface design.

Catalysts exhibiting moderate NO binding energies (∼−0.4 to −0.6 eV) and adaptable electronic structures, such as vacancy-rich nitrides, provide a transitional zone where both pathways operate concurrently, distributing the free-energy range across two reduced barriers and flattening the Tafel slope.[83,84] Modifying the catalyst microenvironment through hydrophobic ionomers that regulate water, atomic dopants that adjust d-band occupancy, and sub-nanometer confinement that increases local NO pressure offers additional mechanisms for directing the bifurcation.[85] Subsequent theoretical research should delineate both the minimum-energy pathway and the flux-weighted ensemble of trajectories in the context of oscillatory potentials and stochastic proton delivery, while experimental initiatives utilise *operando* spectroscopy to monitor NOH* and NH_2OH* coverages in real time.[86] Integrating these insights will finalise the design principles for catalysts that facilitate rapid N–O activation alongside unobstructed NH_3 desorption, bridging the mechanistic divide between milligram-scale demonstrations and kiloampere-scale plasma-integrated stacks.

It will be essential to develop *operando* spectroscopic tools that can direct catalyst adjustments in real time. Dynamic

Table 1 Comparative performance metrics of the state of art NORR electrocatalysts

Catalytic materials	Catalyst type	Electrolyte	NH_3 yield (*vs.* RHE)	NH_3 FE/% (*vs.* RHE)	Operating condition	Ref.
Nanostructured Ag	Noble metal catalysts	EFeMC (99.9% NO)	2.29 mol h^{-1} m^{-2} (−0.165 V)	~100% (−0.165 V)	H-type electrolytic cell	108
Ru-LCN	Noble metal catalysts	0.5 M Na_2SO_4 (1% NO)	45.02 μmol h^{-1} mg_{cat}^{-1} (−0.2 V)	65.96% (−0.2 V)	H-type electrolytic cell	126
$Ru_{0.05}Cu_{0.95}$	Noble metal catalysts	0.5 M Na_2SO_4 (20% NO)	17.68 μmol h^{-1} cm^{-2} (−1.1 V *vs.* Ag/AgCl)	64.9% (−1.1 V *vs.* Ag/AgCl)	H-type electrolytic cell	127
RuGa	Noble metal catalysts	0.1 M K_2SO_4 NO/Ar (20% NO)	320.6 μmol h^{-1} mg_{Ru}^{-1} (−0.2 V)	72.3% (−0.2 V)	H-type electrolytic cell	128
Cu(111) nanosheets	Non-noble metal catalysts	0.1 M K_2SO_4 (99% NO)	371.89 μmol h^{-1} cm^{-2} (−0.59 V)	93.19 ± 1.99% (−0.59 V)	H-type electrolytic cell	147
Cu_6Sn_5	Non-noble metal catalysts	—	10 mmol h^{-1} cm^{-2} (−0.23 V)	> 96% (−0.23 V)	Flow cell	130
Cu@Co	Non-noble metal catalysts	0.1 Na_2SO_4 (1% NO)	627.20 μg h^{-1} cm^{-2} (−0.5 V)	76.54% (−0.5 V)	Flow cell	148
hcp-Co nanosheets	Non-noble metal catalysts	0.1 M Na_2SO_4 NO (10%)/He	439.5 μmol h^{-1} cm^{-2} (−0.6 V)	72.58% (−0.6 V)	H-type electrolytic cell	62
Zero-valent Fe/C	Non-noble metal catalysts	—	1239 μmol h^{-1} cm^{-2} at 10% NO	96% FE at 1% NO	—	70
Ni@NC	Non-noble metal catalysts	0.1 M HCl (100% NO)	34.6 μmol h^{-1} cm^{-2} (0.16 V)	72.3% (0.16 V)	H-type electrolytic cell	143
Bi@C	Non-noble metal catalysts	0.1 M Na_2SO_4	1592.5 μg h^{-1} mg_{cat}^{-1} (−0.4 V)	93% (−0.5 V)	H-type electrolytic cell	150
Sb_1/a-MoO_3	Non-noble metal catalysts	0.5 M Na_2SO_4 (100% NO)	273.5 μmol h^{-1} cm^{-2} (−0.6 V)	100% (−0.6 V)	H-type electrolytic cell	142
Co_1/MoS_2	Transition-metal decorated layered chalcogenide	0.5 M Na_2SO_4 (100% NO)	217.6 μmol h^{-1} cm^{-2} (−0.5 V)	87.7% (−0.5 V)	H-type electrolytic cell	154
Cu_1/MoS_2	Transition-metal decorated layered chalcogenide	0.5 M Na_2SO_4 (100% NO)	337.5 μmol h^{-1} cm^{-2} (−0.6 V)	90.6% (−0.6 V)	H-type electrolytic cell	155
Fe_1/MoS_{2-x}	Transition-metal decorated layered chalcogenide	0.5 M Na_2SO_4 (100% NO)	88.2 μmol h^{-1} cm^{-2} (−0.6 V)	82.5% (−0.6 V)	H-type electrolytic cell	144
W_1/MoO_{3-x}	Oxide and vacancy-engineering	0.5 M Na_2SO_4 (100% NO)	308.6 μmol h^{-1} cm^{-2} (−0.5 V)	91.2% (−0.4 V)	H-type electrolytic cell	145
Nb-B_2N_2	Carbon-supported heteroatoms	0.1 M HCl (100% NO)	8.2×10^{-8} mol^{-2} s^{-1} (−0.6 V)	77.0 ± 0.6% (−0.6 V)	Flow cell	156
Honeycomb-like carbon nanofiber	Non-metal-based catalysts	0.2 M Na_2SO_4 (10% NO)	22.35 μmol h^{-1} cm^{-2} (−0.6 V)	88.33% (−0.6 V)	H-type electrolytic cell	160
g-C_3N_4	Non-metal-based catalysts	0.1 M PBS (20% NO/Ar)	30.7 μmol h^{-1} cm^{-2} (−0.8 V)	45.6% (−0.8 V)	H-type electrolytic cell	167
2P@C_2N	Non-metal-based catalysts	—	8.9×10^5 per s per site (400 K)	—	—	163

environmental conditions have a significant impact on catalyst performance, as was mentioned in the interfacial pH management. As we discussed in this section, *operando* EPR studies on oxygen-deficient TiO_{2-x} surfaces have revealed dynamic changes in Ti^{3+} sites. This evidence suggests that catalysts that can modify defects reversibly may respond actively to shifting operating circumstances. To use reversible defect formation or ion exchange, future catalysts must incorporate responsive architectures that can self-modulate their electronic structure or surface composition in real time. These adaptable catalysts might continue to function optimally under the variable NO feed conditions found in actual plasma-coupled electrolyser operations.

Furthermore, integrating dual-site motifs with vacancy engineering presents a largely unexplored opportunity to synergistically enhance both adsorption and hydrogenation kinetics. An example is the Ru–Cu alloy system, where isolated Ru sites embedded in a Cu matrix significantly reduced the activation barrier for *NOH formation, resulting in an order-of-magnitude improvement in ammonia production rates compared to monometallic Cu. Embedding such dual-sites within vacancy-rich substrates, like vacancy-engineered TiO_2 or transition metal carbides, could simultaneously tackle stability concerns identified for carbides, oxides, and MBenes. These hybrid designs may thus deliver the required durability ($\geq$100 h at industrial current densities) without sacrificing the kinetic and selectivity advantages of dual-site catalysis.

Finally, the catalyst–electrolyte interface itself must become a designed component rather than merely an operational boundary. Leveraging insights from advanced CO_2 electrolysis, deliberate structuring of the electrolyte–catalyst interface *via* ionomer engineering or structured ionic liquids could ensure stable proton and electron transport under aggressive conditions. Hierarchical gas-diffusion electrodes (*e.g.*, Cu) can markedly improve interfacial pH stability and alleviate flooding by shortening proton-diffusion pathways. These engineered interfaces could increase the number of feasible catalysts, especially among metal-free or weakly binding frameworks. Thus, by adjusting interface properties to stabilize intermediates and suppress HER independently of the underlying catalyst material.

5. System-level integration and engineering constraints

5.1 Quantitative milestones and integration

This section translates the catalyst-level metrics of the previous section into stack- and plant-level engineering requirements. To transition from component-level improvements to integrated systems, a quantitative framework must align electrocatalyst performance with stack architecture, balance-of-plant requirements, and upstream plasma integration constraints.

5.1.1 Molecular performance descriptors. The primary molecular descriptors defining catalyst performance include the adsorption free energy of nitric oxide (ΔG_{*NO}), which should lie between -0.45 and -0.60 eV to balance residence time and prevent surface poisoning; the activation barrier for the first hydrogenation step (*NO $\rightarrow$ *NOH), $\Delta G^{\ddagger}_{*NOH}$, which must remain below 0.45 eV to enable efficient turnover at moderate overpotentials; and the relative kinetics of hydrogen evolution, such that the exchange current density for HER ($i_{0,HER}$) is at least one order of magnitude lower than that for nitric oxide reduction to avoid parasitic H_2 generation. Together, these energetic and kinetic thresholds delineate a performance envelope in which high selectivity and adequate activity can be sustained at practical current densities. Empirical studies in nitrate and CO_2 electroreduction systems demonstrate that catalysts conforming to these criteria maintain faradaic efficiencies exceeding 90% over extended operation.[170] A concise energy-level diagram of plasma-assisted N_2 activation is shown (Fig. 10a).

5.1.2 Electrolyte speciation window. Electrolyte selection must reconcile ionic conductivity with interfacial speciation. Highly alkaline media minimise ohmic drop and have demonstrated durability in water electrolysis, yet they destabilise key *NOH and NH_2OH intermediates and favour N_2O formation when hydroxide accumulates. At the opposite extreme, strongly acidic solutions (pH $<$ 2) supply protons so readily that the Heyrovsky step outpaces *NO hydrogenation, diverting current to HER and accelerating membrane corrosion. Weakly buffered near-neutral electrolytes (pH 5–8) offer the most promising compromise: their moderate proton activity suppresses HER while preserving NOH kinetics, and they remain compatible with polymer membranes under humidified gas-phase operation.[171] Guided by this rationale, we provisionally target phosphate- or borate-buffered media of ionic strength $\approx$0.5 M and pH 6 $\pm$ 1 as the baseline for integrated NORR stacks until a dedicated electrolyte-optimisation campaign identifies an even narrower optimum.

5.1.3 Stack-level voltage milestone. A third filter translates component-level gains into stack performance targets. To approach energy efficiencies exceeding 50% under continuous operation, thresholds identified by techno-economic models for viability at US \$0.02 kWh^{-1} electricity, stack-level operation must achieve $<$0.6 V *iR*-free at $\geq$300 mA cm^{-2}.[32,172] While similar metrics have been approached in nitrate reduction systems, sustained operation at these current densities remains a forward-looking benchmark for NORR. Explicitly calling out this voltage milestone as its own filter ensures it can be directly referenced in subsequent stack- and plant-level design discussions.

5.1.4 System integration and stack engineering. Single-cell performance alone does not guarantee scale-up success. Stack integration introduces new constraints in gas distribution uniformity, pressure regulation, thermal management, and long-term component durability. Nevertheless, decades of alkaline water–electrolyser operation show that membranes, bipolar plates, and sealants tolerate high OH^- activity when oxygen and carbonate ingress are rigorously managed, providing a valuable durability benchmark for emerging NORR stacks. However, even if individual catalyst descriptors are optimised, economic viability hinges on achieving these targets at the stack level, where power losses, heat accumulation, and impurity management can negate molecular-scale gains.

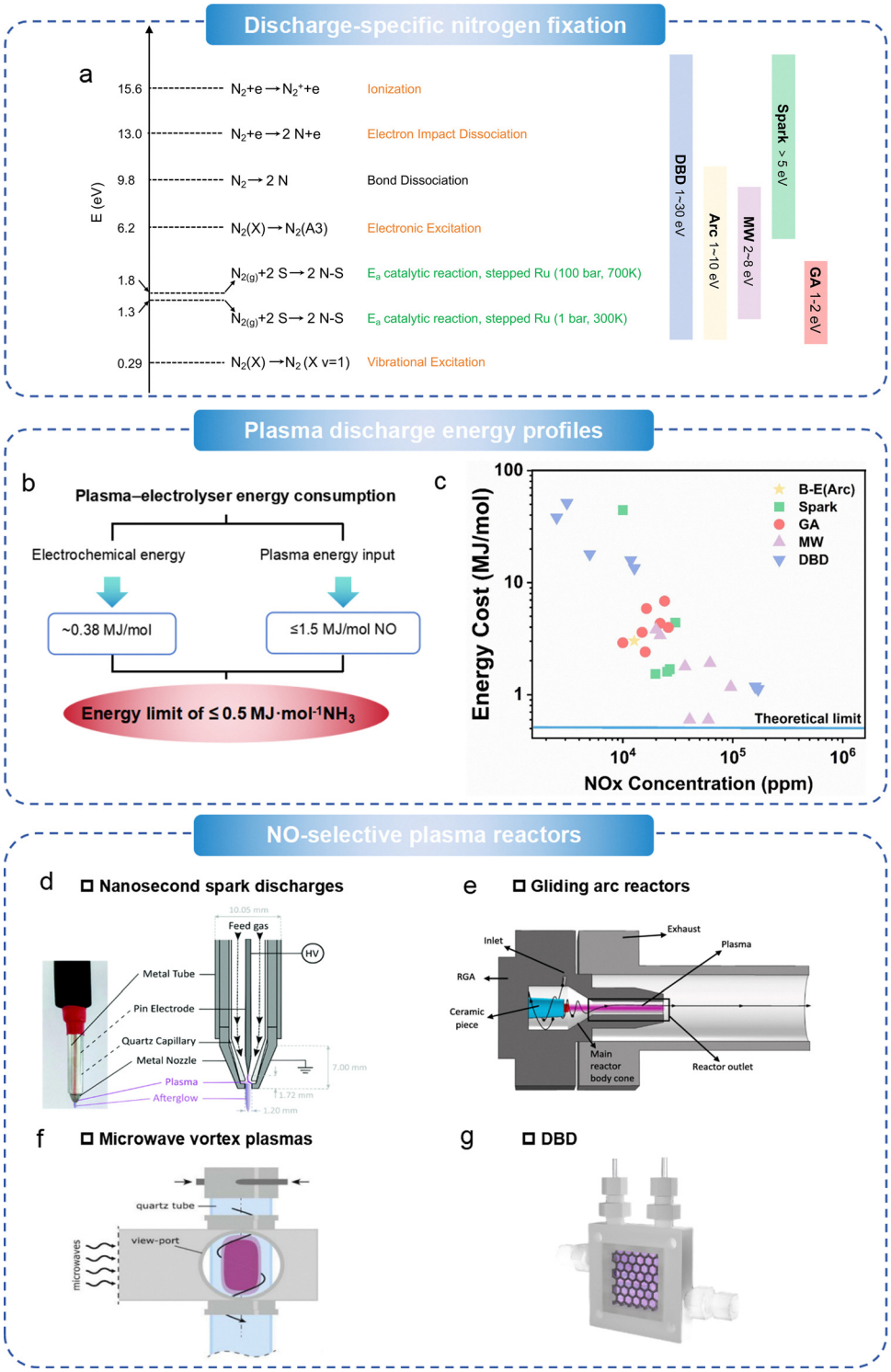

Fig. 10 (a) Nitrogen-fixation pathways associated with different plasma-discharge modes. (b) Theoretical emption limits of plasma-assisted electrocatalysis. (c) Comparative specific energy consumption of the various discharge modes. (d) Spark discharge plasma.[183] Copyright 2022, The Royal Society of Chemistry (e) sliding-arc discharge.[181] Copyright 2023, American Physical Society. (f) Microwave plasma discharge.[180] Copyright 2025, Elsevier (g) dielectric-barrier discharge.

5.1.5 Pilot-scale benchmarks

5.1.5.1 Durability. Operational continuity is another non-negotiable metric. Target durability of 1000 hours with less than 5% degradation in current density or selectivity remains the minimum threshold for pilot deployments. Encouragingly, alkaline electrolysers for water splitting have demonstrated similar endurance.[173] While long-duration testing in NORR systems is still limited, recent studies have shown promising

signs of catalyst and membrane stability over tens to hundreds of hours, implying that with improved gas handling and material durability, these lifespans could approach the 1000-hour mark. The use of corrosion-resistant bipolar plates, hydrophobic gas diffusion layers, stable ionomers, and ionomers resistant to NO-induced nitration will be critical in meeting this standard.

An integrated module achieving 300 mA cm^{-2} at 0.6 V (*iR*-free) with 90% FE would yield approximately 0.963 mmol h^{-1} cm^{-2} of ammonia, or 0.0164 g h^{-1} cm^{-2}. This could serve as a minimum viable benchmark for early-stage pilot systems, ensuring meaningful productivity while remaining within conservative design and power targets. For a 100 cm^2 active area stack operating 24/7, this equates to 47 kg $year^{-1}$ NH_3. To meet a target of t day^{-1} NH_3, approximately 21 m^2 of active area would be required, assuming continuous operation and negligible downtime. With cell-level durability metrics established, we next translate the current-density and voltage targets into power, footprint, and thermal loads at the stack and plant scales.

5.1.5.2 Productivity. From a system integration standpoint, this productivity is consistent with the capabilities of compact non-thermal plasma units reviewed by Deepak *et al.*[174] An additional illustration would be a cascade discharge reactor, which can produce NO_x at power inputs lower than 40 W per 10 cm^2 reactor area. Gallo *et al.*[41] found that 20 W modules with a 5 cm^2 footprint produced stable NO at an energy cost of 0.72 MJ mol^{-1}. At m^2 scales, sub-kW plasma sources can sustain the NO flux needed for $\geq$50 kg NH_3 day^{-1} production.

While these architectural and operational considerations define the performance ceiling for integrated NORR stacks, translating them into viable pilot and commercial systems requires a structured, milestone-driven development pathway.

5.2 Plasma delivery and primary gas conditioning

Plasma, often referred to as the fourth state of matter, consists of partially ionised gases containing a complex mixture of electrons, ions, excited molecules, and radicals.[175] In non-thermal plasma (NTP), the electron temperature is significantly higher than the gas temperature, enabling activation of strong chemical bonds.[176] This unique property allows plasma systems to operate flexibly and efficiently under ambient conditions, making them well-suited for integration with intermittent renewable energy sources.[177] As a result, plasma-assisted synthesis of nitrogen oxides (NO_x) presents a sustainable and decentralised alternative to conventional high-temperature, high-pressure routes for activating inert molecules like N_2. To ensure effective integration with downstream MEA cells, several factors must be carefully managed. The trade-off between NO_x concentration and specific energy input for various discharges is illustrated. Ideally, the target NO concentration should be maintained between 1% and 6% to provide a sufficient supply of reactants. The presence of NO_2, O_3, and other impurities must be minimised to prevent electrode degradation and efficiency loss.

Plasma-assisted NO_x synthesis is strongly influenced by the type of plasma discharge employed. Each discharge type presents trade-offs in energy efficiency, NO yield, NO/NO_2 selectivity, and feasibility of integration with downstream electrochemical systems. As a pioneering plasma-based technology for NO_x synthesis, the Birkeland–Eyde (B–E) process utilized arc discharge, achieving an energy consumption of 2.41 MJ mol_N^{-1} and producing NO_x concentrations of 1–2%.[178] Since B–E process first commercialized plasma-based NO_x synthesis in 1903, a wide range of plasma discharge types and reactor designs have been investigated for NO_x production, including nanosecond spark discharges,[179,180] gliding arc discharge (GAD),[181] Microwave vortex plasma,[180] and dielectric barrier discharge (DBD),[182] among others.

5.2.1 Performance targets at the plasma–electrolyser interface. Having surveyed plasma discharge types and their trade-offs, we now quantify the energy and purity requirements at the plasma–electrolyser interface. The plasma effluent must reach the gas-diffusion electrode as a narrowly specified reagent stream whose thermodynamic quality and flow condition sustain NORR at module-level current densities $\geq$ hundreds of mA cm^{-2} and faradaic efficiencies >90%. Energy is the primary constraint: the five-electron conversion of NO to NH_3 carries a minimum Gibbs work of 0.24 MJ mol^{-1}. Allowing realistic kinetic overpotentials and a stack efficiency of 95% lifts the electrochemical budget to $\approx$0.38 MJ mol^{-1}. To keep the complete plasma–electrolyser route below 1.5 MJ mol^{-1} NH_3, the plasma stage may therefore consume no more than 0.50 MJ mol^{-1} NO. Nanosecond spark discharges already approach this figure, reporting 0.42 MJ mol^{-1} NO at 1 bar.[183] By contrast, gliding arc devices still require 2.4–3.6 MJ mol^{-1} NO[184] (Fig. 10b).

It is important to note that the reported energy cost accounts only for the power consumed during the pulse duration, excluding inter-pulse (*i.e.* standby) power losses. Despite their advantages, scaling up high-voltage pulsed power supplies remains a significant challenge. A thorough and accurate evaluation of energy consumption is essential before further industrial deployment of plasma-assisted NO_x synthesis, particularly given that the high yields and low energy inputs reported for MW discharges in the 1980s have not been reliably reproduced in recent studies. This is especially critical when nanosecond-repetition pulsing is used to drive the plasma, as voltage and current signals exhibit rapid rise and fall times on the nanosecond scale, making precise power measurement and calculation increasingly vital.

Transient diffusion–reaction simulations of a 50 μm catalyst layer show that a 1.5% NO feed at 298 K and 1 bar delivers the stoichiometric flux to sustain >100 mA cm^{-2}. Increasing the mole fraction beyond 5% yields no further gain because proton transport becomes limiting. Experiments with microwave vortex plasmas report 3.8% NO_x at 2 MJ mol^{-1}, safely within the 1.5–5% design window.[185]

DFT-driven micro-kinetics demonstrate that trace oxidants displace key *NOH and $*NH_2$ intermediates, depressing selectivity once the combined partial pressure of O_2 and NO_2 exceeds 5×10^{-5} bar. To maintain $\geq$95% surface probability for the associative path, the plasma effluent must therefore contain <50 ppm total O_2 + NO_2. Nanosecond-spark reactors satisfy

this criterion, routinely delivering NO_2 below 10 ppm at 4–11 g kWh^{-1}.[183]

Pressures above 1.3 bar accelerate GDE flooding, whereas sub-ambient operation introduces compression penalties. Consequently, the interface should operate at 0.9–1.1 bar. Humidity must be similarly balanced: membrane conductivity falls sharply below 25% RH, yet dew points above 15 °C promote homogeneous hydrolysis of NO to HNO_2. Empirical screening identifies a dew point of 5 ± 3 °C (0.8–1.2 wt% H_2O in the gas phase) as the optimum.

5.2.2 Achieving energy-efficient, high-selectivity NO generation. Meeting the 0.50 MJ mol^{-1} NO ceiling while holding O_2 + NO_2 below 50 ppm requires a discharge that maximises electron-impact dissociation of N_2 and O_2 yet forestalls secondary oxidation. Four reactor classes illustrate how pulse shaping, vibrational activation, and rapid quench can be tuned toward that dual objective. Fig. 10c summarises and compares the energy consumption of different plasma reaction types for nitrogen fixation.

A schematic demonstration of nanosecond-spark discharge reactor is presented in Fig. 10d. 10 to 50-nanosecond voltage spikes produce electron temperatures >8 eV at average gas temperatures ≤450 K, creating a strong non-equilibrium wherein the e-V ladder of N_2 ($v \geq 7$) is efficiently climbed and dissociation proceeds through the $N_2(A\ ^3\Sigma_u^+)$ channel. When operated at 1% duty cycle and flow velocities >10 m s^{-1}, a residence time around 2 ms limits the NO → NO_2 back-reaction; combined with water-cooled pin electrodes, this yields 0.42 MJ mol^{-1} and <10 ppm NO_2.[183] Recent kinetic modelling reproduces these figures and attributes the high selectivity to the rapid collapse of O + NO recombination once T_g drops below 600 K.[183]

Gliding-arc reactors operate in a mixed thermal and non-thermal regime (Fig. 10e). The expanding arc column attains local gas temperatures above 2000 K that raise the equilibrium NO yield but simultaneously sustain NO_2 formation through O + NO. Energy costs of 2.4–3.6 MJ mol^{-1} NO remain typical.[184] Nevertheless, two engineering levers can narrow the gap. First, introducing a nanosecond pilot pulse just ahead of the gliding arc reduces the ignition voltage and shortens the high-enthalpy phase, trimming energy per mole by ≈40%. Second, a double-swirl vortex insert accelerates convective quench and has been shown to cut NO_2 from 180 ppm to 45 ppm at constant throughput.[186] With both measures, the gliding-arc platform could plausibly reach 1 MJ mol^{-1}.

Microwave vortex plasmas (Fig. 10f) confine the discharge in a cold-wall resonator where azimuthal swirl stabilises a low-pressure plasma core (<10 torr equivalent) inside an ambient-pressure sheath. Electron densities of 10^{14} cm^{-3} and mean electron energies near 4 eV preferentially populate vibrationally excited N_2 without raising bulk gas temperature above 600 K. Kelly and Bogaerts achieved 3.8% NO_x at 2 MJ mol^{-1}.[187] Scaling studies demonstrate a linear rise in NO output with microwave power up to 5 kW while the specific energy cost plateaus near 2 MJ mol^{-1} NO, indicating appreciable headroom for optimisation. Pulse-width modulation that interleaves 200 μs high-power bursts with 800 μs low-power holds increases the $N_2(v)$ fraction and curtails wall losses, suppressing NO_2 from 60 ppm to 30 ppm.[188]

DBD (Fig. 10g) is frequently applied due to its simplicity, atmospheric-pressure operation, and scalability. However, their performance in NO_x synthesis is limited by high energy costs (typically >15 MJ mol_N^{-1}) and modest NO_x concentrations (<1%) regardless of the catalyst packing. The presence of a high reduced electric field (generally >100T_d) results in elevated electron energies being primarily consumed in electronic excitation, thereby leading to low overall energy efficiency.[189] The low NO concentration and high energy consumption make it challenging for DBD to be directly coupled with gas-fed MEA for efficient NORR when using air as the feedstock, despite its relative ease of scalability.

Across all modes, shaping the reduced electric field to 5–100T_d emerges as the universal design rule: below 5T_d N_2 excitation is too weak, above 100T_d the density of vibrationally excited N_2 species rapidly decreases and is instead dominated by electron-impact dissociation, which leads to increased energy consumption.[184] High-peak-power pulse modulators therefore adopt rise times <5 ns and repetition rates tuned so that the root-mean-square E/N sits in the 50T_d window while maintaining average current densities of 5–10 A cm^{-2}. Complementary rapid-quench hardware is indispensable. Water-jacketed quartz tubes provide 400 K s^{-1} cooling but add 15 kPa pressure drop; supersonic Laval-nozzle ejectors achieve >10^6 K s^{-1} with <5 kPa penalty and are increasingly favoured in compact modules, mirroring quench concepts borrowed from steam-cracking furnaces.

5.2.3 Effluent conditioning: quench, purification and humidity control. The plasma reactor must hand over a gas stream whose temperature, composition and humidity lie inside the narrow envelope without erasing the energy gains of the discharge, which demands a tightly integrated conditioning train whose total overhead remains below 0.20 MJ mol^{-1} NO. Four hardware blocks are required: rapid quench, catalytic scrubbing, membrane drying and low-pressure adsorption.

Quench exchangers arrest homogeneous NO oxidation by removing enthalpy within the first 2 ms of residence. Water-jacketed quartz tubes provide cooling rates near 4 × 10^2 K s^{-1} but impose a 15 kPa pressure drop, equivalent to 0.03 MJ mol^{-1} compression work at 40% blower efficiency.[190] Laval-nozzle ejectors accelerate the stream to Mach 1.6, removing heat at >10^6 K s^{-1} while limiting back-pressure to <5 kPa and cutting the parasitic load to 0.01 MJ mol^{-1} NO.[187] This step arrests NO_2 formation and freezes the vibrational distribution that underpins the favourable energy cost of the discharge.

Residual O_2 and NO_2 are removed in a short-contact catalytic scrubber that operates at 350 K and 1 bar. A bimetallic Pt–Ru gauze converts O_2 to H_2O and reduces NO_2 to NO using a 1% H_2 bleed, achieving complete removal at space velocities up to 60 000 h^{-1}.[191] The exotherm raises gas temperature by only 8 K, and the additional hydrogen consumption contributes <0.02 MJ mol^{-1} to the specific energy cost.

Humidity control follows in a polymeric hollow-fibre membrane dryer. At 298 K and 1 bar, a polypropylene shell-side

sweep can depress the dew point to 5 °C, equivalent to ≈1 wt% H_2O. Bench permeance values of 3×10^{-7} mol m^{-2} s^{-1} Pa^{-1} imply that treating a 10 slm plasma effluent (7.4×10^{-3} mol s^{-1}) and removing $\approx 1.5 \times 10^{-4}$ mol s^{-1} H_2O requires about 0.18 m^2 active area, not 0.02 m^2 as originally stated.[192] The associated pressure drop remains <2 kPa, and blower work therefore adds <0.001 MJ mol^{-1} NO to the energy balance.

Finally, trace N_2, Ar and H_2O that would otherwise dilute the electrolyser feed are stripped in a single-bed pressure-swing adsorber loaded with Li-LSX zeolite. Cycling between 1.1 bar and 0.25 bar at a 30 s period removes inert ballast and raises the NO mole fraction from 2.0% to 4.0% while recovering 92% of the NO mass. Vacuum desorption and repressurisation together incur an energy penalty of ≈0.08 MJ mol^{-1} NO at 45% blower efficiency, consistent with adsorption-cycle audits for low-pressure Li-LSX units operating at similar step times.[193]

5.3 Secondary gas-handling constraints

5.3.1 Impurity removal. In plasma-integrated NORR systems, one of the most critical requirements is the delivery of NO streams to the electrolyser with sufficient purity to preserve catalyst selectivity and membrane stability.[172,194] While plasma air oxidation typically yields low-conversion gas mixtures containing a few percent NO, downstream gas-conditioning modules must remove excess O_2 and co-produced NO_2 to achieve post-treatment impurity levels below 50 ppm. These purification steps, *via* catalytic absorption, quenching beds, and controlled drying, are essential to prevent side reactions and maintain electrochemical efficiency, even if the NO fraction entering the electrolyser remains in the low percentage range.

5.3.2 Humidity management. Analogous challenges in CO_2 electrolysis offer practical lessons: in gas-fed CO_2RR cells, membrane performance and product selectivity deteriorate rapidly if the feed gas is not adequately conditioned.[173] Maintaining relative humidity within ±2 °C of the target dew point is critical to avoid two competing failure modes: membrane dehydration, which increases ionic resistance and destabilises adsorbed intermediates, and flooding, which blocks gas-accessible pores within the gas diffusion electrode. Moreover, even low-level oxygen ingress, exceeding 10 ppm, can oxidise catalysts, shift reaction pathways, and lower CO_2 conversion. These findings are highly transferable to NORR systems, where NO's volatility and its partially reduced intermediates (NOH*, NH_2OH*, HNO*) make the local hydration state and electric field at the membrane interface particularly sensitive. Inadequate humidification promotes membrane dehydration and desorption instability, while excess humidity fosters flooding, impeding gas–liquid contact that is essential for NO delivery and intermediate turnover. Trace O_2 levels further complicate selectivity by oxidising NO to NO_2 or N_2O, redirecting the reaction away from ammonia. Empirical studies in related electrochemical systems have shown that even transient deviations from optimal humidity or oxygen content, such as ±5% relative humidity or O_2 spikes above 100 ppm, can reduce membrane lifetimes by 20–40%, due to cumulative oxidative damage and ionic transport disruption.[195] Therefore, precise regulation of dew point and O_2 content is not merely an operational parameter; it is a quantitative durability constraint that must be embedded into the gas-handling architecture of NORR stacks.

5.3.3 Pressure control. Nevertheless, it is neither necessary nor desirable for the NO stream to be pure. In fact, NO concentrations in the range of 0.5–2% (5000–20 000 ppm) are already consistent with plasma air oxidation outputs and are well within the operational range of GDE-based electrolysers. These dilute concentrations are sufficient to sustain selective NO reduction provided the system architecture supports rapid mass transport and maintains adequate surface coverage. GDEs with engineered porosity, hydrophobicity, and gas-channel geometry can accommodate low-partial-pressure NO feeds while still achieving partial current densities exceeding 100 mA cm^{-2}.[196] At these levels, HER remains suppressed, and the production rate is predominantly limited by interfacial mass transfer rather than thermodynamic NO activity. Operating at 0.5–2% NO (5000–20 000 ppm) is sufficient for selective reduction; maintaining a slight positive pressure differential ($\Delta p = p_{gas} - p_{liq} \approx$ 0–5 kPa) prevents flooding and electrowetting.

5.4 Electrolyser interface design

In electrocatalytic NORR systems, sustaining high faradaic efficiency and long-term stability hinges critically on the purity and concentration of the NO feedstock. Real-world NO_x effluents, however, are rarely pure and often contain a mixture of NO, NO_2, O_2, water vapour, and other minor components. These impurities can poison active sites, alter reaction pathways, and accelerate membrane degradation. This requirement underscores why we identified plasma as the most reliable method for generating NO at low concentrations on demand.

The literature indicates that even trace amounts of O_2 and NO_2 can negatively impact the selectivity of ammonia formation.[197] In particular, O_2 has been shown to promote the competitive reoxidation of NO back to NO_2 and N_2O, thereby redirecting the reaction away from the desired NORR pathway.[198] Moreover, the presence of O_2 and other reactive oxygen species can modify the reaction network by enabling additional pathways for nitrite formation and N_2O evolution, both of which deplete NO from the catalytic cycle. Consequently, pre-treatment strategies to reduce the oxygen content of the feed gas are indispensable. Industrial gas-separation processes, including membrane separation and gas-absorption scrubbing, have been investigated to lower O_2 concentrations at the source.[199,200]

In the context of NORR, membrane separation technologies have emerged as particularly promising. Zeolite membranes, for instance, have demonstrated excellent molecular-sieving properties due to their well-defined microporous structures and high selectivity for NO. Pasichnyk *et al.* employed molecular dynamics simulations to systematically evaluate the performance of purely siliceous CHA and DDR zeolite membranes for ternary $NO/N_2/O_2$ gas mixtures.[201] Their findings showed that both membrane types effectively retained NO, blocking its permeation while allowing relatively high fluxes of N_2 and O_2.

Potential-of-mean-force calculations revealed a substantial energy barrier for NO transport across the zeolite pores, underscoring the physical mechanism of selective NO retention.

Beyond zeolites, MOFs with coordinatively unsaturated metal sites have been explored for their superior NO capture performance. Hu *et al.* synthesised a bimetallic $Ni_{0.37}Co_{0.63}$-MOF-74 *via* solvothermal routes and demonstrated an impressive NO adsorption capacity of 174.3 cm^3 g^{-1} at ambient conditions.[202] Inspired by this success, Pan *et al.* integrated a MOF layer onto GDEs to create a multifunctional electrocatalytic flow reactor.[203] In this hybrid system, the MOF layer concentrated NO from a dilute 2% feed, directing it to a bifunctional Cu|Ni/NiO catalytic interface that converted NO to NH_4^+ and NO_3^-, which coupled to form NH_4NO_3 *in situ*. Even at ultra-low inlet concentrations of 20 ppm NO, the MOF-modified GDE doubled the yields of NH_4^+ and NO_3^- compared to an unmodified GDE, highlighting the potential of MOF-functionalised interfaces to simultaneously address capture, mass transfer, and catalytic conversion.

Such integrated purification-conversion designs resonate strongly with strategies developed in the CO_2 and CO reduction communities. For instance, in gas-fed CO_2 reduction cells, trace O_2 in captured CO_2 streams can poison active sites and degrade membrane performance. Researchers have employed pressure-swing adsorption, membrane-based gas purification, and chemical absorbents (like amine scrubbing) to selectively remove O_2 and other oxidants prior to electroreduction.[204] Analogous principles can be directly applied to NORR: low-pressure swing adsorption modules or amine-based O_2 scavenging can mitigate reoxidation challenges at the NO feed interface. Moreover, GDE-based flow cells in CO_2RR have integrated CO_2 capture directly within the cathode architecture using amine-functionalised layers.[205] This approach has shown stable performance and high faradaic efficiency for carbon products over long operation periods, providing a robust basis to mirror in NORR systems. However, direct applicability remains to be experimentally verified.

Dew-point management is another vital aspect of gas conditioning. In NORR, water vapour levels must be carefully managed: some hydration is essential for proton conductivity, but excess moisture can promote NO disproportionation to nitrite (NO_2^-), an intermediate that diminishes ammonia yields, as observed in plasma nitrogen fixation studies.[206] Conversely, insufficient hydration can lead to membrane dehydration, increasing the area-specific resistance and destabilising adsorbed NO-derived intermediates. Analogous challenges have been documented in CO_2-fed GDEs, and recent studies have explored mitigation strategies such as precise humidification control and membrane optimisation to overcome these challenges, a promising avenue that could be adapted for NORR.[207] These findings underscore the need for precise dew-point control to ensure consistent gas–liquid equilibrium at the triple-phase boundary.[208]

For NO feeds, this translates to a delicate balance: humidification must maintain membrane hydration and proton conductivity while minimising water-induced NO conversion to nitrite. Membrane humidifiers and enthalpy exchange modules, as widely adopted in PEM fuel cell systems, offer well-established engineering strategies that can be adapted for NORR stacks. These modules operate by exchanging heat and moisture between the incoming and outgoing gas streams, ensuring thermal and moisture stability even under fluctuating loads. While direct studies in NORR are limited, these concepts align with insights from CO_2RR and other gas-fed electrochemical processes.[209] Applying these strategies to NORR could prove similarly effective, although direct applicability remains to be validated through systematic experimental studies.

Beyond purification and hydration control, the composition of the gas feed itself is a crucial determinant of NORR performance. While conventional wTable 1ater electrolysers can operate with near-pure hydrogen and oxygen streams, NORR must contend with NO streams containing 0.5–5% NO, co-produced O_2, and variable humidity levels. Studies on CO_2 electrolysis indicate that even low concentrations of O_2 can significantly diminish selectivity and catalyst stability due to the preferential reduction of O_2 over CO_2.[207] For NORR, the challenge is compounded by the fact that NO-derived intermediates (such as NOH*, NH_2OH*) are themselves prone to oxidation. Therefore, while achieving impurity levels below 50 ppm O_2 is a critical design target for downstream gas-conditioning modules, it is also possible to explore catalysts that are more resilient and selective under these conditions, an avenue that warrants parallel investigation to reduce system-level purification burdens.

Strategies to meet these targets include catalytic deoxidation beds, typically composed of noble metal catalysts (like Pt/Al_2O_3) that selectively scavenge O_2 without perturbing NO partial pressures. These have been demonstrated in CO_2 feed gas conditioning for electrolyser applications and can be adapted for NO streams. In addition, controlled drying (*via* molecular sieves or membrane dryers) is essential to stabilise dew-point fluctuations and prevent downstream flooding of the GDE. In PEM fuel cells, drying strategies have evolved to leverage membrane-integrated dew-point control,[210] an approach that can inform future NORR system designs.

In perspective, the interplay of gas conditioning, impurity management, and dynamic humidification represents a complex but tractable engineering challenge. The lessons learnt from CO_2 and CO electroreduction, where gas capture, impurity removal, and water management are already commercialised at multi-MW scales, provide a robust foundation for NORR adaptation. However, the distinct chemical reactivity of NO and its intermediates necessitates tailored gas-conditioning strategies that address both the unique challenges of NO chemistry (notably, the reactivity of NO-derived species with trace oxidants) and the mechanical stability of the overall system. This perspective argues that such integration is not merely ancillary but central to realising the high selectivity and long-term stability of NORR, particularly when coupled to non-thermal plasma modules producing NO in dilute air feeds.

Looking forward, emerging materials such as dual-phase zeolite–MOF composites, ionomer-stabilised MOFs, and

nano-engineered perovskite oxygen scavengers offer exciting avenues for gas-conditioning modules that simultaneously capture, purify, and modulate the chemical microenvironment of NO streams.[211,212] For instance, metal-free carbon–MOF composites, recently demonstrated in CO_2RR gas handling, could offer high selectivity for NO adsorption while preserving the integrity of downstream ionomer membranes.[213–215]

5.5 Gas diffusion electrolysers

5.5.1 Cell configurations & GDE fundamentals. Modern electrocatalytic NO-to-NH_3 synthesis employs two primary reactor formats: conventional aqueous-phase electrolysers and gas-diffusion electrode flow cells (GDEs, Fig. 11a).[194] In the latter, a membrane electrode assembly (MEA, Fig. 11c), comprising an ion-exchange membrane sandwiched between catalyst layers deposited on porous gas-diffusion layers, facilitates simultaneous gas- and liquid-phase transport to the reaction interface.

Conventional single-chamber, three-electrode cells remain popular for early research due to their simplicity and ease of control. However, they suffer from cathode–anode crossover: oxidized intermediates diffuse through the electrolyte or membrane back to the cathode, consuming NH_3 and deactivating active sites.[216] These systems also exhibit sluggish NO mass transfer, as gas must first dissolve into the bulk electrolyte before reaching the catalyst.

To overcome these limitations, dual-chamber electrolysers physically separate anodic and cathodic compartments with a proton-exchange membrane (*e.g.*, Nafion).[217] his arrangement curbs product crossover and side-reaction interference, preserving selectivity by isolating the NH_4^+/NH_3 stream from oxidizing species.[218] Yet even dual-chamber devices face mass-transfer constraints for sparingly soluble gases like NO, prompting a shift toward continuous-flow GDE architectures.

In GDE flow cells, the electrocatalyst resides at a gas–liquid–solid triple-phase boundary: gaseous NO is fed directly through a hydrophobic gas-diffusion layer while liquid electrolyte contacts the catalyst from the opposite side.[219,220] This configuration drastically shortens diffusion paths, immediately removes NH_3 from the reaction zone to prevent secondary oxidation,[126] and decouples gas- and liquid-phase flows, enabling stable operation at high current densities.

5.5.1.1 Design implications. Dual-layer carbon GDLs containing 15–20 wt% PTFE in the macroporous substrate and $\leq$10 wt% in the microporous layer provide a break-in pressure exceeding the Laplace threshold of sub-micrometre pores while keeping gas-phase mass-transfer resistance below 0.5 s cm^{-1}, meeting the same criteria already validated for high-rate CO_2 flow-by cells.[221] Differential-pressure controllers (electronic proportional valves linked to Δp transducers) must hold $p_{gas} \leq p_{liq} + 5$ kPa under dynamic load to pre-empt electrowetting events that would displace the gas–liquid interface.

Recent advances leverage 3D-structured flow-fields, embedding baffles, pillars or micro-turbulators to disrupt laminar layers and homogenise gas distribution in deep stacks.[222] Feed-segmentation schemes subdivide the inlet manifold into parallel sub-streams, ensuring balanced NO loading cell-to-cell,[223] while asymmetric inlet–outlet layouts tune local residence times to mitigate edge effects and assembly variances.[224] All of these innovations must be benchmarked against the target of $\Delta p < 5$ kPa under nominal load to avoid excessive OPEX and preserve stable gas-phase operation.

GDEs, as extensively studied in CO_2RR applications, create short diffusion paths and large gas–liquid–solid triple-phase boundaries.[225–227] This proven enhancement of mass transport and active-site delivery in CO_2RR systems suggests a directly analogous advantage for improving NO delivery and selectivity in NORR. Cheon *et al.* developed a GDE-integrated flow electrolyser by doping nanoscale zero-valent iron onto a carbon-black support and immobilising the composite on the GDE surface.[227] Under a 1% NO feed, the system achieves an NH_3 faradaic efficiency as high as 96%, reflecting a strong synergy between reactant transport across the gas–liquid–solid triple phase boundary and catalytic activity. Density-functional-theory calculations indicate that Fe sites effectively facilitate N–O bond cleavage in the key H_2NO intermediate, thereby enhancing pathway selectivity toward NH_3. Further modulation of proton concentration in the electrolyte enables an NH_3 production rate of 1239 μmol cm^{-2} h^{-1} under a 10% NO stream, fully validating the GDE architecture's pronounced advantages in accelerating NO mass transfer and converting low-concentration reactants.

Shao *et al.* constructed a Cu_6Sn_5 alloy catalytic layer on a gas-diffusion electrode and systematically assessed its NO-to-NH_3 performance in both flow-cell and membrane-electrode assembly electrolyser.[130] In the flow cell, the directed flow field and a stable gas–liquid–solid triple-phase interface enabled the electrode to reach an ammonia partial current density of 1.373 A cm^{-2} at −0.23 V (*vs.* RHE), corresponing to an NH_3 production rate of 10 mmol cm^{-2} h^{-1} with a faradaic efficiency exceeding 96% (Fig. 11b). Singh-Morgan *et al.* utilised a porous nickel catalyst in a membrane electrode assembly electrolyser, achieving a faradaic efficiency for ammonia of 93% at 60 mA cm^{-2} with a 1% NO feed (Fig. 11d).[228] Long *et al.* reported a Cu foam electrocatalyst exhibiting a faradaic efficiency of 93.5% and a yield of 517 μmol cm^{-2} h^{-1}, although the reliance on high-concentration NO gas poses limitations for commercial applications.[194] Subsequent scale-up in a MEA test delivered ~2.5 mol h^{-1} of ammonia at ~2.6 V and 400 A, decisively demonstrating the laminated membrane–electrode architecture's ability to lower ohmic resistance and sustain industrial-level current densities.

Building on this concept, Pan *et al.* integrated a metal–organic framework (MOF) layer with high NO-capture capacity onto gas-diffusion electrodes.[203] Adopting this strategy allows creating an all-in-one electrocatalytic flow reactor that synergistically captures and efficiently converts dilute NO streams, as illustrated schematically in Fig. 11a. This approach mirrors strategies in CO_2RR, where amine-functionalised layers within GDEs improve capture and conversion.[205] Dew-point management, critical for maintaining membrane hydration, also borrows lessons from CO_2RR, where improper humidification

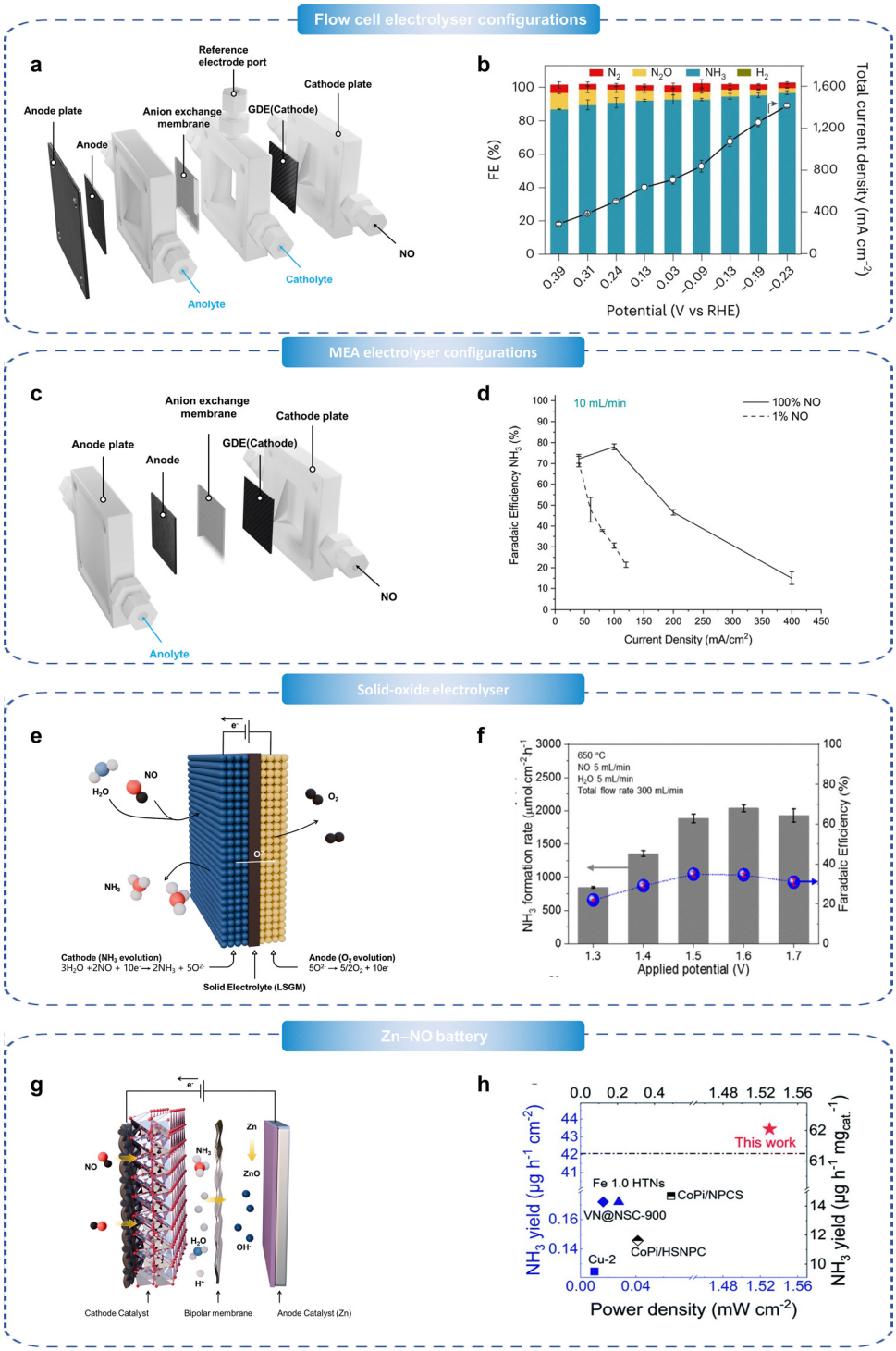

Fig. 11 (a) Schematics of the flow cell electrolyser configurations (b) A GDE flow electrolyser delivers an NH_3 partial current density of 1417 mA cm^{-2} at −0.23 V (*vs.* RHE) with a FE > 96%[130] Copyright 2023, Springer Nature. (c) Schematics of the MEA electrolyser configurations. (d) An MEA electrolyser equipped with a porous Ni cathode achieves 93% NH_3 selectivity at 60 mA cm^{-2} under a 1% NO feed.[228] Copyright 2025 Cellpress (e) Schematic illustration of electrochemical NH_3 synthesis using a solid-oxide electrolyser. (f) A solid-oxide electrolyser operating at 650 °C attains an NH_3 formation rate of 1885 μmol cm^{-2} h^{-1} with a faradaic efficiency of 34.8%, underscoring the benefits of gas–solid separation[50] Copyright 2022 American Chemical Society (g) diagram of the Zn–NO battery (left) and the open-circuit voltage (OCV) of the assembled Zn–NO battery equipped with a Ni_2P/CP cathode (right). (h) A Zn–NO metal battery employing a Ni_2P/carbon-paper cathode yields 62.05 μg h^{-1} mg_{cat}^{-1} of NH_3 while simultaneously delivering a power density of 1.53 mW cm^{-2} and an open-circuit voltage of 2.06 V, demonstrating pollutant valorisation coupled with energy conversion[151] Copyright 2021 Royal Society of Chemistry.

causes carbonate build-up and performance loss.[229] Membrane humidifiers and enthalpy exchange modules from PEM fuel cell systems provide a starting point for NORR stack engineering.[210]

Beyond these examples, other GDE and MEA optimisations draw directly from the CO_2RR field. In CO_2RR, engineering the catalyst layer to control porosity, hydrophobicity, and ionic pathways has been shown to improve triple-phase boundary density and maintain long-term stability.[209] These strategies, such as adjusting ionomer content, controlling catalyst-layer thickness, and employing mesoporous supports, are directly transferable to NORR. Implementing ionomer-optimised catalyst layers stabilises the electrolyte environment and enhances selective NO conversion.

The integration of ionomer-stabilised MOFs, dual-phase zeolite–MOF composites, and nano-engineered perovskite oxygen scavengers further extends these lessons.[211,212] These materials offer promising avenues for gas conditioning and NO purification, potentially reducing the purification burden on the system while ensuring high selectivity and long-term durability. Within this system, the MOF adsorptive layer first selectively concentrates NO. Guided by the adsorption-energy gradient across the bifunctional Cu|Ni/NiO interface, the enriched NO is directionally conveyed to the catalytic layer, where it is respectively converted into NH_4^+ and NO_3^-; these species subsequently couple in the shared electrolyte to form NH_4NO_3. Relative to the bare GDE, the MOF-modified GDE substantially increases both the NH_4^+ production rate and its faradaic efficiency under a 2% NO feed. Even at an inlet NO concentration of 20 ppm, the yields of NH_4^+ and NO_3^- are enhanced by roughly twofold, confirming the superior capture-and-mass-transfer capability of this novel gas-diffusion electrode at ultralow NO levels.

5.5.2 Advanced flow-field engineering. Scaling up these architectures also demands insights from industrial CO_2RR stacks. In large-scale CO_2RR electrolysers, flow-field design and channel geometry have been critical for maintaining uniform current distribution and minimising ohmic losses, concepts that apply equally to NORR. Pressurised electrolyzers, like those demonstrated by Yang *et al.* for NO-to-NH_3 conversion,[212] highlight the potential of high-pressure operation for enhancing gas solubility and reaction rates. Their monolithic Cu nanowire array electrodes sustained industrial-level current densities of 1000 mA cm^{-2} for over 100 hours, a benchmark for future NORR systems. Featuring a high density of Fe^{2+} active sites, the Fe[S]/C-GDE achieves an NH_3 faradaic efficiency of 97.2% and a 95.2% conversion rate under a 1% NO feed at −1.3 V (Ag/AgCl), highlighting the flow-cell/GDE design's exceptional current–density capacity (90.8 mA cm^{-2}) and long-term operational stability.

Beyond GDE-based flow electrolysers, researchers are also exploring a variety of reactor architectures to further enhance the conversion efficiency from NO to NH_3. For example, Kwon *et al.* devised a high-temperature solid-state electrolyser employing an oxygen-ion-conducting ceramic electrolyte, achieving NORR under ambient atmospheric conditions (Fig. 11e).[58] Operating at 650 °C, the device attained an NH_3 production rate of 1885 μmol cm^{-2} h^{-1} with a faradaic efficiency of 34.8% (Fig. 11f). Its solid-state electrolyser architecture, characterised by facile gas–solid separation and a minimal risk of electrolyte cross-contamination, shows strong promise for industrial implementation. Although the present system relies on elevated temperatures, strategic improvements such as boosting the catalyst's intrinsic activity and increasing active-site density are expected to enable highly efficient, low-energy NORR under ambient conditions, thereby offering a sustainable pathway for green ammonia synthesis and NO_x waste valorisation. Building on this concept, Yang *et al.* developed a pressurised electrolyser incorporating a monolithic electrode of hierarchically porous copper nanowire arrays (Cu NWA), which delivered marked enhancements in both NH_3 production rate and selectivity.[112] The pressurised electrolyser sustained stable ammonia production for over 100 h at an industrial-scale current density of 1000 mA cm^{-2}. In addition, to achieve highly efficient and selective NO conversion under ambient conditions, Sun *et al.* engineered an electrocatalytic platform centred on a metal–NO battery, which integrates ammonia synthesis, power generation, and pollutant valorisation into a single system (Fig. 11g).[151] The Zn–NO metal battery, featuring a Ni_2P/carbon-paper (Ni_2P/CP) cathode, achieves an ammonia production rate of 62.05 μg h^{-1} mg_{cat}^{-1} while simultaneously delivering a power density of 1.53 mW cm^{-2} and an open-circuit voltage of 2.06 V (Fig. 11h). These results compellingly demonstrate the feasibility of metal–NO batteries to couple highly selective electrochemical NH_3 synthesis with efficient energy conversion, thereby charting a new pathway toward high-performance, sustainable nitrogen-cycle technologies.

5.5.3 Microstructural integration at the triple-phase boundary. Effective flow-field design must be complemented by electrode microstructure that sustains robust gas–liquid–solid interfaces. Microchannel etching within the microporous layer creates preferential pathways that lower tortuosity and equalise local current densities under dynamic loads (Fig. 12a).[72] Controlled hydrophilisation treatments of the GDL and catalyst support tune wettability: hydrophilic zones aid electrolyte distribution, while hydrophobic domains preserve gas permeability and prevent electrolyte breakthrough.[227,230] Furthermore, graded ionomer distributions concentrate ionic pathways near the catalyst–electrolyte interface, minimising flood-prone regions deeper within the layer.[231,232] This co-design of macro- and micro-scale features ensures that triple-phase boundaries remain active and stable, enabling sustained current densities $\geq$ hundreds of mA cm^{-2} at $>90\%$ FE over extended operation without flooding or salt crystallisation.

Gas-diffusion electrodes developed for CO_2 or O_2 electrocatalysis are often operated in either a flow-through (Fig. 12b) or a flow-by (Fig. 12c) regime, the choice being dictated largely by mass-transfer gains *versus* flooding risk. For nitric-oxide reduction, however, the geometry is not merely an engineering preference; it is essential to maintaining the reaction pathway itself. In a flow-by configuration the NO feed is introduced at the rear of the cathode and diffuses only a few tens of micrometres to the catalyst layer, while the product NH_3 leaves in the

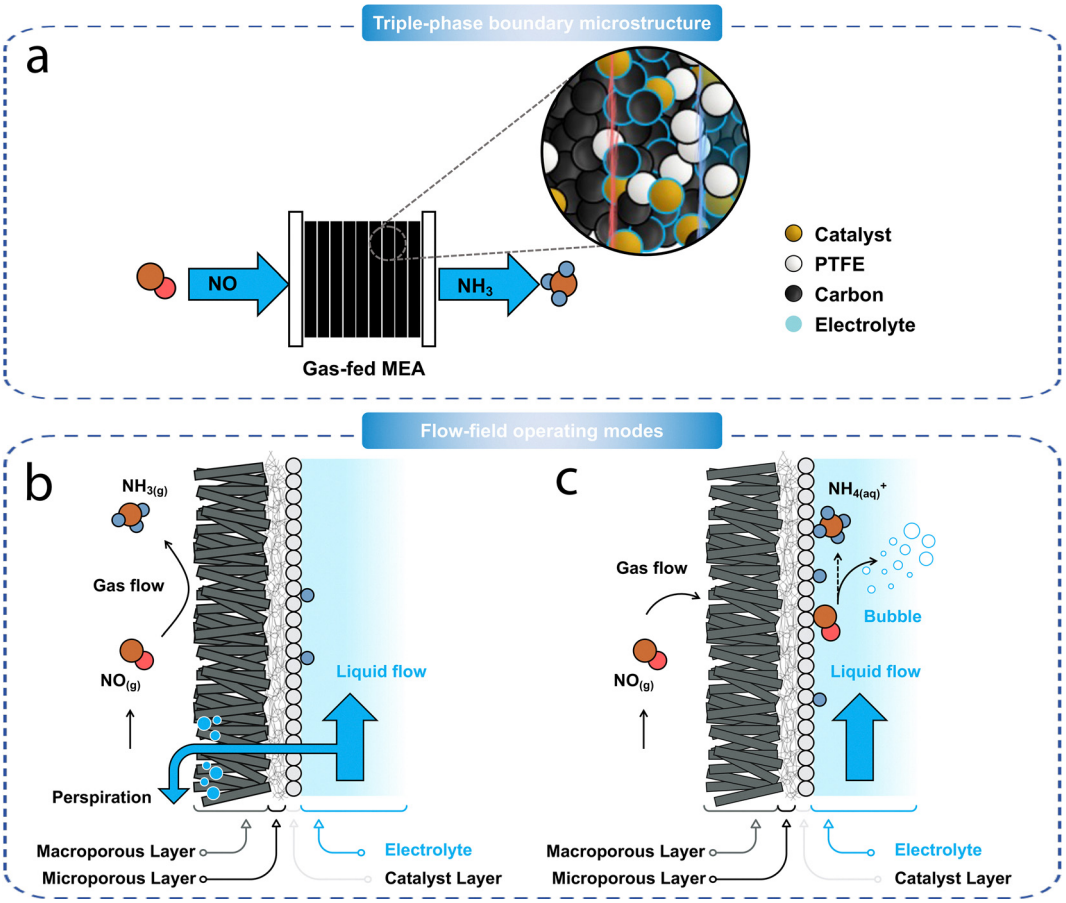

Fig. 12 (a) Microstructural rendering of the catalyst-ionomer–pore network at the triple-phase boundary. (b) Flow-by mode. NO-rich gas sweeps laterally across the GDE surface adjacent to the electrolyte, keeping gas saturation below ~40%, suppressing flooding and nitrite/nitrate salt crystallisation, and allowing NH_3 to leave exclusively in the gas stream, so a simple condenser operating 5–10 K below cell temperature passively captures >95% of the product while meeting occupational exposure limits. (c) Flow-through mode. Gas is driven through the porous electrode into the electrolyte channel, which shortens diffusion distances but raises the risk of electrolyte intrusion, precipitate clogging, and pressure-loss penalties familiar from CO_2 electrolyser systems.

same gas stream. This lateral, rather than through-plane, transport preserves an unmixed gas phase on the catalyst side and keeps the liquid electrolyte on the opposite face of the porous layer. Experimental analyses of CO_2 electrolysers show that when $\Delta p = p_{gas} - p_{liq}$ is held slightly positive (0–5 kPa) no gas bubbles enter the catholyte and no electrolyte penetrates the GDL pores, a regime that sharply reduces ohmic loss and hydrodynamic stress compared with flow-through operation. These hydrodynamic principles translate directly to NO reduction: stable capillary exclusion of catholyte is the only means of ensuring that both reactant and product remain in the gas phase at technologically relevant current densities.

The criticality of flow-by geometry for NORR extends beyond merely engineering preference into fundamental reaction control. Ensuring lateral diffusion of NO from the rear of the cathode guarantees that both reactants and products remain exclusively gaseous. This configuration prevents undesirable mixing with electrolytes, preserving reaction selectivity, efficiency, and pathway stability. Maintaining such strict separation avoids the rapid autoxidation of dissolved NO into nitrite and nitrate species, significantly improving ammonia yields and operational stability compared to flow-through configurations.

Chemically, the flow-by configuration significantly enhances product purity and reaction pathway integrity. When NH_3 remains entirely gaseous, it bypasses the ionization into ammonium ions (NH_4^+) that typically occurs upon contact with liquid electrolytes at neutral or near-neutral pH, thereby circumventing costly downstream separation processes. This strategic spatial control directly aligns with the fundamental thermodynamic advantage inherent in NORR, reinforcing its economic and technical superiority over conventional aqueous-phase nitrate reduction pathways.

This strict spatial control of reactants and products is especially critical given the chemical instability of dissolved NO. In aerated aqueous media, it undergoes third-order autoxidation (rate law $-d[NO]/dt = k[NO]^2[O_2]$; $k \approx 3 \times 10^6\ M^{-2}\ s^{-1}$ at 22 °C) to yield nitrite and, sequentially, nitrate, thereby diverting the nitrogen pool toward the five-electron NO_3RR pathway and eroding faradaic efficiency for NH_3.[233] Such chemical drift is negligible when NO never contacts the bulk electrolyte,

a condition uniquely guaranteed by the flow-by architecture. At 25 °C the same rate law gives a pseudo-first-order half-life of <30 ms for 10 μM NO in air-saturated water (1.3×10^{-4} M O_2), an order of magnitude shorter than the 0.2–0.5 s residence time of a 50 μm laminar diffusion film in typical GDEs.[233]

The same geometric argument applies to the product side. At the near-neutral pH of typical catholytes ($6 \leq$ pH ≤ 8), gaseous NH_3 is quantitatively protonated to $\geq$99.4% NH_4^+ at pH 8 (pK_a $NH_4^+/NH_3 = 9.25$),[234,235] forming soluble ammonium ions that remain in the liquid phase. Once protonated, ammonia cannot be recovered by simple condensation; instead, energy-intensive ion-exchange or stripping steps are required, incurring a separation penalty of 0.3–0.5 MWh $t_{NH_3}^{-1}$ in recent techno-economic analyses. Ensuring that NH_3 never crosses the gas–liquid boundary, therefore collapses an entire downstream unit operation and preserves the thermodynamic advantage that motivates NO electroreduction in the first place. Thus, adopting a flow-by GDE architecture not only maintains reaction integrity but also directly translates into considerable economic savings by eliminating energy-intensive separation processes.

Flow-by geometry further mitigates two principal chronic failure modes well-documented in CO_2 electrolyser systems: (i) flooding-induced electrolyte intrusion and (ii) precipitation-driven salt crystallization. In NORR, salt crystallization risks are intensified due to rapid nitrite/nitrate formation from dissolved NO autoxidation, occurring orders of magnitude faster than carbonate precipitation observed in CO_2 reduction. *Operando* imaging confirms stable gas saturation in flow-by operated GDLs, significantly reducing these critical failure modes over long-duration operation. Recent *operando* X-ray microtomography confirms that carbon-based GDLs operated in flow-by mode maintain gas saturation below 40% even at 0.2 A cm^{-2}, preserving triple-phase boundary integrity over >100 h continuous electrolysis.[236]

5.6 Stack thermal management

As architectures approach their mass- and heat-transfer limits, attention must turn to active management of stack temperature and assembly precision. Effective thermal management in electrocatalytic NO reduction stacks is essential because it governs not only system stability and operational safety, but also the long-term reliability and performance of the ammonia production process. During operation, the thermal load in the stack arises from three primary sources: the sensible heat of the incoming gas streams, the exothermic enthalpy change associated with NO reduction reactions, and heat exchange between the stack and its surroundings.[237] While temperature control in laboratory-scale single cells can be managed relatively easily due to small cell volumes and limited heat production, industrial-scale stacks present a much more demanding scenario. In these larger systems, the substantial heat generated from electrochemical reactions cannot be adequately dissipated by natural convection or radiative losses alone, especially given the small temperature gradient typically existing between the stack and its environment.[238]

Without robust thermal management, internal stack temperatures will steadily rise, leading to performance degradation and possible system failure. Excessive thermal gradients within the stack can induce spatially heterogeneous reaction rates, localised membrane dehydration, and mechanical stress due to differential expansion of materials. Conversely, inadequate stack temperatures retard electrochemical kinetics, limiting current densities and overall ammonia yield, and can even provoke catastrophic flooding events if condensation of water or reaction byproducts occurs in unintended locations. To prevent such failures, the thermal-management system must be designed to ensure uniform temperature distribution throughout the stack and to provide rapid heat removal across the full range of anticipated operating conditions.

Industrial practice has adopted a range of thermal-management strategies to address these challenges. These include heat-sink-based passive cooling designs and active liquid-cooling systems, which can be supplemented with auxiliary gas-cooling loops.[239,240] For instance, heat-sink fins are often added to external stack frames or endplates to increase the effective heat-exchange area, facilitating more efficient heat dissipation through convective and conductive pathways. In addition, phase-change materials have been explored as integrated components within cooling circuits. These materials can absorb large amounts of latent heat during phase transitions, acting as buffers to stabilise transient temperature spikes during dynamic load conditions.[241] Industrial practice has adopted a range of thermal-management strategies to address these challenges. These include heat-sink-based passive cooling designs and active liquid-cooling systems, which can be supplemented with auxiliary gas-cooling loops.[239,240] For instance, heat-sink fins are often added to external stack frames or endplates to increase the effective heat-exchange area, facilitating more efficient heat dissipation through convective and conductive pathways. In addition, phase-change materials have been explored as integrated components within cooling circuits. These materials can absorb large amounts of latent heat during phase transitions, acting as buffers to stabilise transient temperature spikes during dynamic load conditions.[241]

Liquid-cooling approaches also benefit from innovations in alternative coolants, which can offer superior thermal conductivity and lower viscosity compared to traditional water-glycol mixtures. Studies have demonstrated that alternative liquid coolants, such as fluorinated or dielectric fluids, can maintain more uniform stack temperatures and reduce pumping power requirements while preventing corrosion of sensitive catalyst and membrane materials.[242]

Moreover, emerging design concepts such as condensing-tower-inspired curved flow-field geometries provide avenues to couple gas-phase heat and mass transport more efficiently within the stack architecture.[243] By leveraging such biomimetic geometries, these approaches simultaneously enhance heat dissipation and facilitate improved reactant distribution across the catalyst layer.

5.7 Control architectures for operational stability

5.7.1 Assembly process and optimisation. In electrocatalytic NO-to-NH_3 systems, multiple electrolytic cells are typically

connected in series to form a complete stack capable of delivering high reaction rates and robust output. This serial architecture imposes stringent demands on manufacturing precision and uniform stacking. Inevitable production deviations, such as end-plate warping, structural deformation, and misalignments, particularly pronounced in stacks employing metallic bipolar plates, can severely impact stack performance.[244] Non-uniform compression during stacking, often seen as localised end-plate bending, can degrade reaction environments and cause performance heterogeneity.[245] Mechanical stresses during assembly also directly affect membrane durability and lifetime.[246]

To address these challenges, finite-element modelling and analytical simulations have been employed to predict the spatial distribution and evolution of stress, gasket compression, and current-density profiles during stack assembly.[247,248] These numerical simulations provide visual insights into how these assembly-induced factors influence overall stack performance. It is equally essential to evaluate how dimensional tolerances propagate in-plane and couple through stacked layers, impacting final assembly geometry and operational uniformity. Such systematic analysis underpins rational design improvements in assembly protocols for scalable, durable, and efficient NO-to-NH_3 stacks.

While precise assembly and microstructural control form the foundation for achieving uniform current distribution and mechanical stability, ensuring long-term durability and performance consistency necessitates an integrated monitoring and control strategy. Such an approach leverages real-time data streams and advanced digital twins to actively manage system health and performance, as explored in the following section.

5.7.2 Predictive data-driven regulation. Beyond mechanical precision and careful electrolyte and interface design, achieving long-term stability in NORR systems requires real-time, adaptive regulation of operating conditions and reaction environments. This is especially important in plasma–electrolyser setups, where changing NO feed levels and varying power needs put different kinds of stress on the reactor over time. Data-driven control frameworks, including digital twins and AI-assisted predictive models, emerge as powerful tools to navigate these dynamic regimes. They complement material-level robustness and flow-field engineering by enabling continuous sensing, rapid diagnosis, and proactive control of system behaviour under real-world operating conditions.[248] We will discuss how to integrate these advanced data strategies to prevent system degradation and ensure stable, high-yield ammonia synthesis during extended operation.

These data-driven strategies are similar to methods already used in PEM fuel cells, where digital twins and predictive maintenance systems are successfully used to handle sudden changes in load, reduce mechanical damage, and extend the life of the system. Additionally, advanced AI and machine learning load-balancing methods used in power electronics, like those for controlling frequency in microgrids, provide a reliable model for handling the changing power demands in plasma–electrolyser hybrids.[249] By comparing fuel cell technologies and CO_2 reduction electrolysers, we highlight that the durability of the stack depends on both the materials used and how the system operates, including factors like evenness in mechanical structure, control of humidity, and the management of changing operational loads. These insights from different fields show that it's possible to include real-time intelligence in NORR systems, creating a clear plan for increasing operational lifetimes and ensuring reliable ammonia production on a large scale. At the material level, mechanical deformation of MEAs under repeated thermal and pressure cycling can induce localised delamination, crack propagation, and accelerated catalyst deactivation. This is reminiscent of the degradation mechanisms in PEM fuel cell stacks, where repetitive load cycles and humidity swings induce irreversible polymer chain scission and catalyst layer restructuring, ultimately reducing cell voltage by $\sim$40 mV over 1000 hours of operation.[250] Similarly, the repetitive expansion-contraction cycles in plasma–NORR stacks, driven by fluctuating plasma output and dynamic gas feed rates, can compromise the structural integrity of sealing gaskets and bipolar plates. High-resolution digital image correlation mapping, which has been applied to various mechanical systems and can be adapted and extended to plasma–NORR stacks to visualise local strain distributions during load transients and identify weak points for material reinforcement.

Humidity control remains critical to preserving ionic conductivity and triple-phase boundary integrity. Excess hydration promotes NO disproportionation to nitrite and nitrate, while membrane dehydration degrades proton transport and increases area-specific resistance. These lessons echo those of PEM fuel cell stacks, where membrane water content directly modulates both ionic conductivity and mechanical durability. Emerging solutions include advanced ionomer chemistries with tailored water-uptake behaviour (such as partially fluorinated poly(arylene ether) membranes) and dynamic humidification modules leveraging enthalpy-exchange membranes, as deployed in automotive PEM stacks.[251] The direct adoption of such modules in NORR stacks can stabilise local water activity within the optimal 50–80 mV proton-availability window that underpins selectivity to ammonia.[92]

During device-level integration of electrocatalytic NORR systems, operational stability and durability constitute the key metrics for assessing their potential for industrial application.[92] A stack comprises several critical components, including electrodes, membrane materials, bipolar plates, current collectors, end plates, and sealing elements, whose structural stability and chemical reliability exert a decisive influence on the system's overall performance.[252] Performance degradation in the stack principally stems from material ageing, stress concentration, and contaminant accumulation during operation and is manifested by diminished proton conductivity of the membrane, loss of active sites, electrode deactivation, and localised corrosion of the bipolar plates.[253] Common failure mechanisms of membrane materials include leakage, sulfonate-group loss, and ionic contamination; leakage pathways can be further classified into mechanically induced structural rupture and chemically driven degradation caused by radical attack.

Electrode performance deterioration primarily arises from the depletion of catalytically active functional groups and microscopic structural damage such as pore blockage. Degradation of bipolar plates is manifested by diminished electrical conductivity, localised cracking, and fatigue failure in regions of stress concentration. Collectively, these failure pathways originate from mechanical non-uniformities introduced during stack assembly, operational temperature gradients and pressure fluctuations, and electrolyte-distribution inhomogeneities that give rise to current-density hotspots, thereby exacerbating pitting corrosion.[246]

To counteract the diverse degradation pathways, it is essential, first, to engineer functional materials endowed with heightened chemical and mechanical robustness and, second, to slow ageing through system-level measures such as optimising operating parameters, homogenising fluid distribution, and suppressing transient overloads. Moreover, establishing a big-data-driven platform for stack-state modelling and operational control can furnish dynamic sensing and predictive regulation of key operating parameters, thereby safeguarding long-term system stability.[254] To address potential component failures or sensor anomalies, a highly robust fault-diagnosis and fault-tolerant control architecture must be incorporated to safeguard system stability and safety under non-ideal operating conditions. Drawing on the modelling experience accumulated for proton-exchange-membrane fuel cell systems, four principal modelling paradigms can be adopted: mechanistic models;[255] semi-empirical models;[254] fully empirical models;[256] and data-driven models.[256] Semi-empirical models incorporate empirical correlations while preserving the core physical mechanisms, thereby reducing computational complexity. In contrast, fully empirical models dispense with internal reaction mechanisms entirely, relying solely on experimental data fitting and thus being well suited for rapid performance evaluation. Data-driven models, constructed through large-scale data training, exhibit strong predictive capability but depend heavily on extensive offline datasets and significant computational resources. Moreover, as an emerging modelling paradigm, digital twins offer a more forward-looking framework for the simulation of NORR systems.[257] By fusing physics-based models, sensor measurements, and operational history, the system's actual running state can be dynamically represented in a virtual environment, thereby enabling full-lifecycle modelling and forecasting of the stack.[258]

Transient load handling is an equally crucial axis. Plasma-driven NO generation is inherently dynamic, with minute-scale fluctuations in NO concentration driven by renewable power intermittency. If unmitigated, these variations can lead to localised proton starvation, uneven current density distributions, and potential catalyst passivation.[259] Furthermore, data-driven approaches provide a transformative opportunity already employed in other emerging fields.[260,261] Machine learning and AI models have successfully predicted membrane dehydration and catalyst layer hot-spot formation in real-time, as seen in studies leveraging digital twins, physics-informed models, and advanced data analytics.[262,263]

Operational stability at scale also depends on managing gas-phase NO delivery under real-world plasma fluctuations. Studies in CO_2RR stacks highlight that even 5–10% variations in feed gas purity can halve selectivity and accelerate catalyst deactivation.[264] In NORR systems, transient re-oxidation of NO to NO_2 or N_2O during plasma–electrolyser coupling will erode ammonia yield unless the NO partial pressure is tightly stabilised. Mitigation tools already proven for CO_2-RR, fast-response flow controllers, and membrane-based gas-recirculation modules,[263] can be ported directly to the NORR stack. Fig. 13

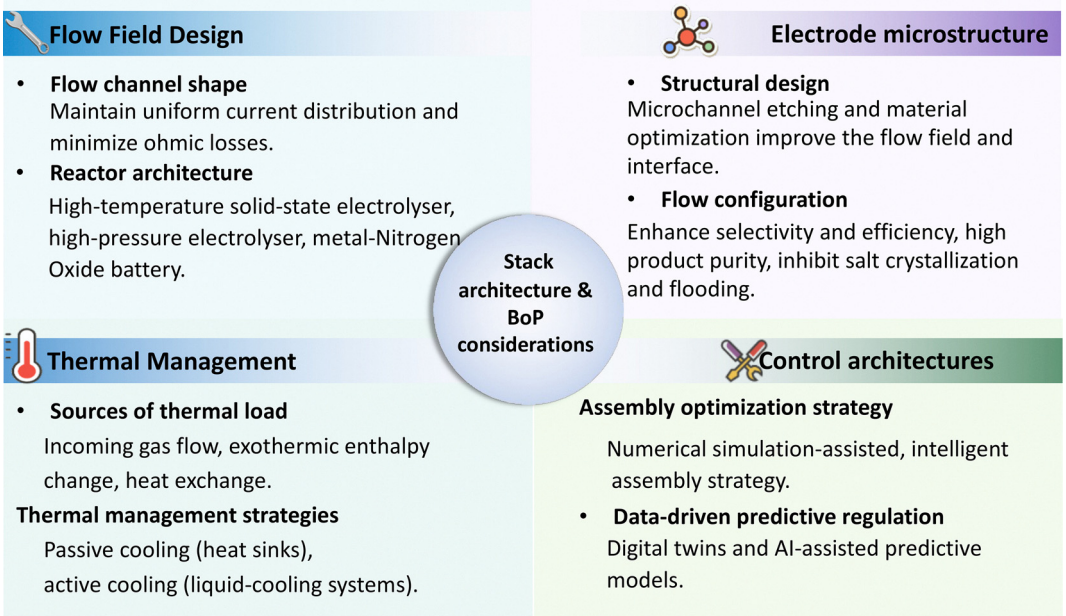

Fig. 13 Maps the key stack- and balance-of-plant trade-offs, flow-field layout, thermal management, and assembly tolerances for a stack architecture.

decontaminates where these gas-handling solutions intersect with the other balance-of-plant levers, flow-field layout, thermal management, and assembly tolerances, providing a roadmap of stack-level trade-offs that must be mastered before advancing up the technology readiness ladder (TRL).

5.8 TRL-based roadmap for system integration

The scale-up of plasma–electrolyser hybrid systems for nitric oxide reduction to ammonia should follow a structured TRL framework inspired by the progression observed in PEM water electrolysis and gas-fed CO_2 reduction technologies while addressing the molecular and operational constraints unique to NO-based pathways. Fig. 14 presents the proposed TRL development pathway and corresponding performance targets for plasma-assisted electrocatalytic NO reduction across different stages of technology maturation. At TRL 3–4, subsystem components are tested independently: the plasma module operates in batch mode, producing high-purity NO with minimal NO_2 (<50 ppm), while the electrolyser benchmarks catalyst selectivity and stability using independently metered gas feeds. At TRL 5, the architecture transitions to continuous-flow operation, with a low-power (20–40 W) plasma module directly coupled to the electrolyser under steady-state conditions. The system must demonstrate sustained performance over 100 hours at ≥ 100 mA cm^{-2} while maintaining high selectivity ($>90\%$) and stability across thermal, humidity, and gas-phase operating regimes. Inline gas diagnostics track NO concentration (ppm level), flow rate (sccm), and impurity suppression, enabling correlation of faradaic efficiency with reactor energetics. This phase mirrors the diagnostic-heavy stack conditioning typical in PEM platforms. At TRL 6–7, the system evolves into a 1–5 kW modular pilot stack with embedded feedback control. Plasma–electrolyser integration is tuned *via* closed-loop regulation of NO feed rate, dew point, and discharge energy, ensuring synchronisation between NO production and electroreduction demand. Stack-level production rates (>20 g h^{-1}) and selectivity ($>90\%$) are validated under intermittent load, while real-time data capture enables predictive maintenance and performance logging. Similar to CO_2RR stack-up transitions, pressure drop, flow uniformity, and ppm-level NO_2 breakthrough are actively managed using sensor arrays and microfluidic manifolds. At TRL 8–9, the system is deployed as a containerised field unit capable of delivering 50–100 kg of NH_3 day^{-1} under variable renewable power. Plasma generation is now fully automated, with duty cycle modulation, impurity rejection, and energy consumption dynamically adjusted *via* AI-assisted control. Cathodic productivity surpasses 0.02 g h^{-1} cm^{-2}, and selectivity exceeds 95% under continuous operation. Long-term metrics, such as start-up latency, uptime, and stack durability, are benchmarked not against theoretical maxima but against field-proven standards in PEM electrolysers, where thermal management, current distribution, and redundancy protocols define commercial viability.[265] The technical targets specified at each TRL stage reflect performance trends already demonstrated in comparable electrified gas-conversion systems and are extrapolated conservatively to ensure alignment with realistic near-term engineering constraints.

6. Economic viability and market translation

6.1 Integrated techno-economic assessment

We present a detailed techno-economic assessment of a hybrid ammonia synthesis system that couples plasma-driven oxidation of air to nitric oxide with electrochemical reduction of nitric oxide to ammonia. The analysis builds upon a recent scenario defined by a decentralised production unit delivering 91 t day^{-1} NH_3, corresponding to the minimum scale for commercial HB synthesis examined by Izelaar *et al.*[32] Their analysis, which applied consistent assumptions across five major green ammonia routes, provides a high-resolution benchmark for evaluating electrolyser-fed Haber–Bosch (eHB), aqueous and solid-state nitrogen reduction, lithium-mediated processes, and conventional steam methane reforming. Their

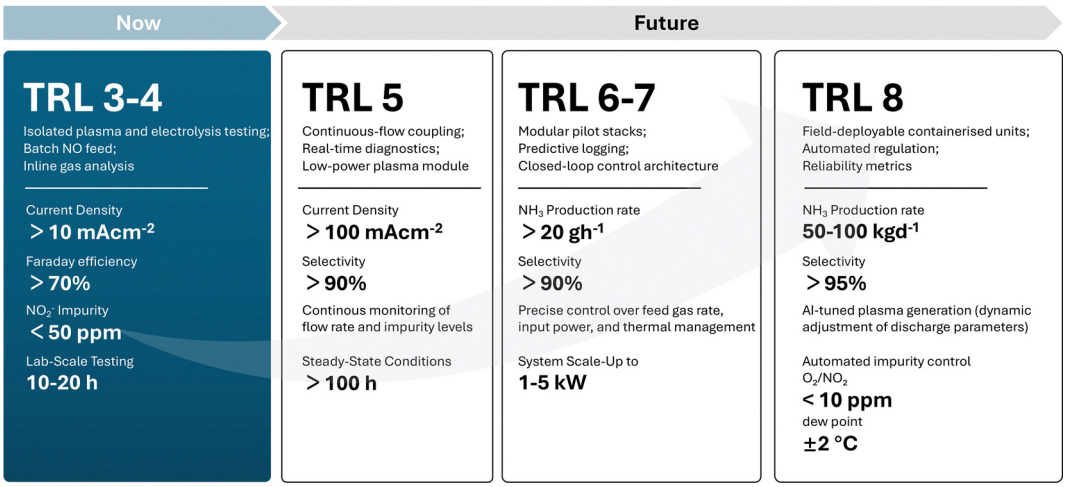

Fig. 14 Roadmap for TRL advancement of plasma–electrolyser hybrid systems for NORR.

findings suggest that eHB will reach a levelised cost of ammonia (LCOA) of approximately 672 USD t^{-1} by 2030 under favourable electricity pricing. However, under more realistic assumptions, including infrastructure and stack replacement costs, the LCOA remains closer to 900 USD t^{-1} in 2030 and declines below 800 USD t^{-1} only after 2035. Their projected cost only declines below 800 USD t^{-1} in the mid-2030s, reflecting gradual improvements in electrolyser capital expenditure and energy sourcing. Other emerging electrochemical pathways, such as high-temperature nitrogen reduction and lithium-mediated processes, are projected to exceed 1000 USD t^{-1} until at least 2035–2040. They concluded that lithium-mediated systems, despite being mechanistically intriguing, face fundamental limitations in lithium recycling, current efficiency, and sensitivity to air and moisture, and therefore are not expected to become cost-competitive within the foreseeable future. Consequently, we omit Li-mediated NRR from our subsequent cost curves and sensitivity analyses, using it only as an upper-bound reference because its projected LCOA ($>$USD 3000 t^{-1}, $\approx$146 GJ t^{-1} NH_3) lies far outside the realistic cost-parity window. High-temperature nitrogen reduction processes face persistent selectivity and electrolyte degradation issues and are often reliant on non-scalable solid-state configurations. Moreover, even as eHB continues to improve in cost and carbon intensity, it remains centralised and capital-intensive, making it an incremental improvement on the traditional process rather than a transformative shift toward decentralised, fully electrified, and renewable-driven ammonia synthesis.

Considering the comprehensive methodology and assumptions by Izelaar *et al.*, we modelled their framework for hybrid plasma–electrolysis, NORR, and used it for benchmarking against other alternatives they have discussed. Accordingly, we constructed a techno-economic model for our NORR pathway using identical or closely matched assumptions to enable meaningful comparison. Within this comparative framework, the NORR pathway is assessed under both present-day and forward-looking conditions. The base case adopts a plasma energy demand of 2.0 MJ mol^{-1} NO, a figure that reflects the lower bound of energy intensity reported for atmospheric-pressure systems at kilowatt scale. A historical analysis of reported plasma systems from 2013 to 2023 reveals a strong temporal trend: median energy intensity has declined from approximately 5.5 MJ mol^{-1} in 2013 to below 2.5 MJ mol^{-1} in 2023. This corresponds to an average improvement rate of around 8% per year, attributed to innovations in discharge stability, vibrational excitation control, flow-field design, and quench engineering[172]

Projections based on this empirically observed trajectory suggest that plasma energy consumption can realistically reach 1.0 MJ mol^{-1} by 2030. Near-term enablers include high-frequency solid-state power electronics, improved gas-phase residence time control, and partial energy recovery from hot effluent streams. Beyond 2035, a further decline toward 0.5 MJ mol^{-1} is considered feasible. This step-change assumes that sub-atmospheric energy efficiencies demonstrated decades ago (as low as 0.3 MJ mol^{-1}) can be partially replicated at ambient conditions by deploying multiphase catalytic quenching beds and continuously tuned hybrid microwave-radio-frequency excitation.

Electrochemical conversion performance is projected with equal granularity. Since 2018, current densities for nitric oxide reduction on gas-fed membrane electrode assemblies have increased from below 50 to beyond 100 mA cm^{-2}, while faradaic efficiency has improved from approximately 30% to more than 60%. Under optimised operating conditions with controlled gas feed and engineered gas-diffusion layers, faradaic efficiencies approaching 90% have been achieved at low overpotentials, although sustained operation at these levels remains confined to short-duration, single-cell studies. These gains stem from improvements in catalyst morphology, electrode structure, gas management, and electrolyte design. Extrapolating conservatively based on the rate of past progress, current densities of 350 mA cm^{-2} at 90% faradaic efficiency are expected by 2030, reaching 500 mA cm^{-2} and 95% efficiency by 2035.

Our techno-economic assessment is built upon five core elements: plant scale, energy consumption, capital investment, operating expenses (including operation and maintenance, and labor), and financial performance over the plant's lifetime. We apply an interest rate of 4.28% and calculate the capital recovery factor over a 20-year horizon. The LCOA is determined by adjusting the NH_3 selling price until the net present value of all cash flows equals zero, ensuring that capital and operating costs are fully recovered. We model a decentralised ammonia facility sized at 91 t day^{-1} NH_3, reflecting the smallest commercial HB unit operating 333 day $year^{-1}$ over a 20-year horizon. For the plasma front end, we adopt a specific energy requirement of 2.0 MJ mol^{-1} NO, consistent with current non-thermal plasma nitric oxide synthesis data. We assume a plasma generator capital cost of 666 670 USD MW^{-1} of installed power. In line with established trends in electrolyser manufacturing of 4% reduction based on IEA projection, we assume a similar annual reduction in plasma capital cost, which aligns with our broader assumptions for cost evolution. Recent work on plasma-based nitrogen fixation has demonstrated that compact 20 W cascade-discharge units can achieve meaningful yields at hardware costs as low as 40 USD, reinforcing the scalability and cost-reduction potential of such systems.[41]

The gas-diffusion electrolyser operates at 0.3 A cm^{-2} and 90% faradaic efficiency, with stack capital costs of 15 876 USD m^{-2}. We apply a 20% balance-of-plant factor, 2.5% O&M costs, and model labour costs based on a 20-person workforce. Electricity prices are set at 0.03 USD kWh^{-1} in the near term and decline to 0.014 USD kWh^{-1} by 2050, aligned with ARENA projections.

Fig. 15a presents the projected LCOA trajectories for our NORR pathway under three scenarios: (1) no further innovation beyond established nitrate reduction metrics (*status quo* cenario), (2) gradual improvements in plasma energy consumption, faradaic efficiency, and current density, and (3) full potential across all modules. In all cases, cost reductions in plasma equipment, electrolyser stacks, and electricity prices are

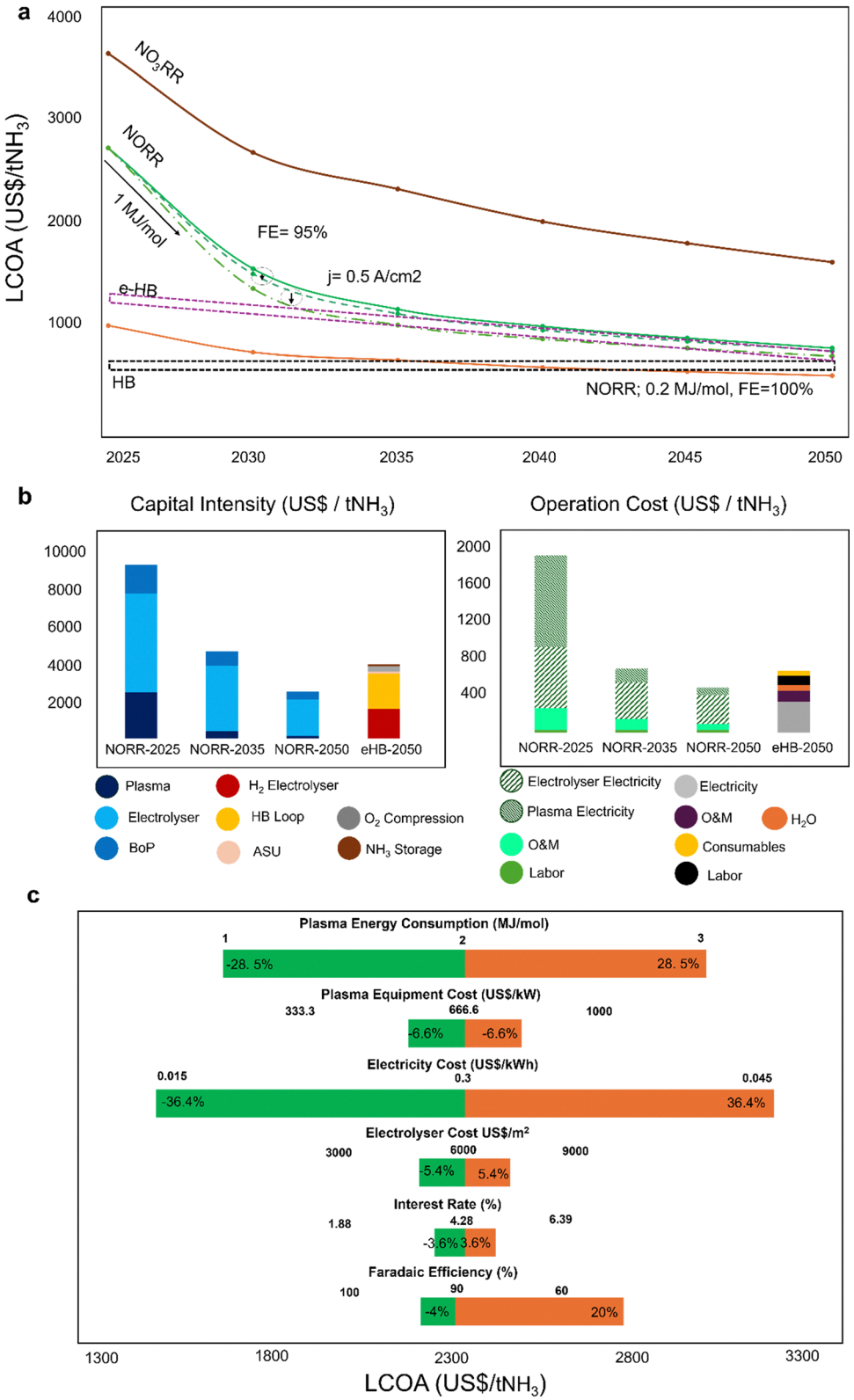

Fig. 15 Techno-economic analysis of our proposed NORR strategy. (a) LCOA compared to alternative pathways. At 0.5 MJ mol^{-1} plasma energy and 500 mA cm^{-2} stack operation, targets within demonstrated learning curves, the NORR pathway reaches 720–760 USD t^{-1} by 2035, converging with the most optimistic eHB forecasts while retaining its modular-deployment advantage. (b) Capital intensity and operational cost breakdowns as a function of time, and (c) sensitivity analysis of cost highlighting key cost drivers and parameter sensitivities.

consistently applied over the modelled time frame. Under the *status quo* scenario, the LCOA is projected at 2292 USD t^{-1} in 2035, falling to 1576 USD t^{-1} by 2050. However, under a transitional innovation scenario that incorporates realistic performance improvements, including an annual 10% reduction in plasma energy consumption until 2035 followed by 2% thereafter, along with 500 mA cm^{-2} current density and 95% faradaic efficiency, the system achieves price parity with centralised eHB around 2035 at approximately 730 USD t^{-1}. A full potential scenario, in which plasma energy is reduced to 0.2 MJ mol^{-1} and electrolyser efficiency reaches 100%, combined with sustained cost declines in electricity and capital equipment, drives the cost further down to 463 USD t^{-1} by 2050, undercutting both eHB and fossil-based HB.

A detailed cost breakdown shows that electrolyser stacks represent the largest capital component of the NORR pathway. By 2035, they account for over 70% (3500 USD t^{-1}) of the total capital cost. In comparison, eHB is dominated by the capital cost of the high-pressure synthesis loop. Operationally, electricity remains the largest single expenditure, followed by O&M costs, both of which decline over time due to improved system performance and scaling. Sensitivity analysis confirms that electricity price is the most influential variable, followed by plasma energy consumption (Fig. 15b). A 50% variation in electricity cost changes ammonia price by over $\pm$800 USD t^{-1}, whereas a 50% swing in plasma energy changes cost by around $\pm$640 USD t^{-1}. In contrast, variations in electrolyser CAPEX and faradaic efficiency result in smaller effects. These targets are grounded in documented trends: electricity cost assumptions align with International Renewable Energy Agency (IRENA) projections, which anticipate a decline from 0.03 USD kWh^{-1} today to 0.014 USD kWh^{-1} by 2050, driven by infrastructure scaling and policy-led renewable deployment. For the electrolyser, we adopt a baseline stack cost of 15 876 USD m^{-2} and apply an annual 4% cost reduction in line with International Energy Agency data. These declines mirror historical learning rates observed in proton-exchange membrane electrolyser technologies. As plasma energy declines, the contribution of electricity to total operating expenses drops from 52% at 2.0 MJ mol^{-1} to 28% at 1.0 MJ mol^{-1}. At the same time, capital intensity is markedly reduced as current density scales: the cost of the electrolyser stack per tonne of ammonia nearly halves between 200 and 500 mA cm^{-2}. Meanwhile, enhanced faradaic efficiency alleviates downstream burden by reducing residual nitric oxide in the product stream, cutting purification and recycling costs by up to 40%.

Our analysis identifies 2035 as the convergence point at which plasma-based nitric oxide reduction can compete directly with the most cost-effective green ammonia systems. Given that electricity cost is the most dominant contributor to the LCOA, the success of initiatives like Australia's Solar 30-30-30 vision becomes particularly crucial. This national target, aiming for 30% solar module efficiency and an installed cost of 0.30 USD W^{-1} by 2030, would drive electricity prices toward 10–15 USD MWh^{-1} or lower, dramatically reducing operational expenditures for electrified chemical synthesis. Such developments could decisively enhance the economic competitiveness of NORR. Beyond 2035, the intrinsic modularity, pressure compatibility, and electrification potential of the system confer unique advantages in distributed deployment contexts, such as remote fertiliser production, hydrogen transport, grid-balancing installations, and even clean energy export (Fig. 15c).

6.2 Commercialisation roadmap

6.2.1 Outlook. The global ammonia market, currently valued at over US$220 billion, is projected to grow at a compounding annual growth rate of 5.9% between 2025 and 2030. Approximately 80% of ammonia is used for fertiliser manufacturing, which accounts for nearly 40% of the market value. Beyond this, applications in pharmaceuticals, textiles, the mining industry, and refrigerants, along with emerging markets such as hydrogen transport and carbon-free fuels, are driving a more diverse and dynamic demand landscape.

NORR represents a viable and competitive pathway for electrified ammonia production among all electrochemical technologies. Our TE analysis, supported by a comprehensive literature review, identifies NORR as the most cost- and energy-effective solution for decentralised ammonia synthesis. With a credible pathway to cost parity with eHB within a decade and potential competitiveness with fossil-based HB by 2050, this emerging platform offers a research-driven trajectory toward commercial viability. The relevant technical diagrams are shown in Fig. 16.

These findings rest on a strong technical foundation. Alongside improvements in electrolyser performance, NO generation efficiency, and declining renewable electricity prices, key enablers such as improved FE, stack design, and current density are central to scaling the process. Our TRL roadmap outlines a structured path from modular validation to integrated systems. By comparing NORR with more mature technologies, we identify bottlenecks, define research priorities, and map out feasible technical milestones.

Our TE analysis confirms that these milestones support commercial viability. We now extend this framework to a business-focused roadmap, illustrating how technical progress in NORR can translate into commercial implementation. Drawing from successful electrification case studies, government programs, and policy instruments, we provide a forward-looking strategy for the translation of NORR research into real-world deployment.

Electrified and decarbonised ammonia production is evolving along two primary commercialisation trajectories. The first is a near-term retrofit strategy focused on decarbonising existing HB facilities by replacing steam methane reforming with water electrolysis technologies such as PEMEL or AEL. These systems generate hydrogen from renewable electricity rather than natural gas, significantly lowering emissions while leveraging existing assets. For instance, Yara International is retrofitting its Pilbara plant in Australia with renewable-powered electrolysers, while Fertiglobe, in collaboration with Scatec and the Sovereign Fund of Egypt, is developing a 100 MW PEM-based green ammonia facility in Ain Sokhna.

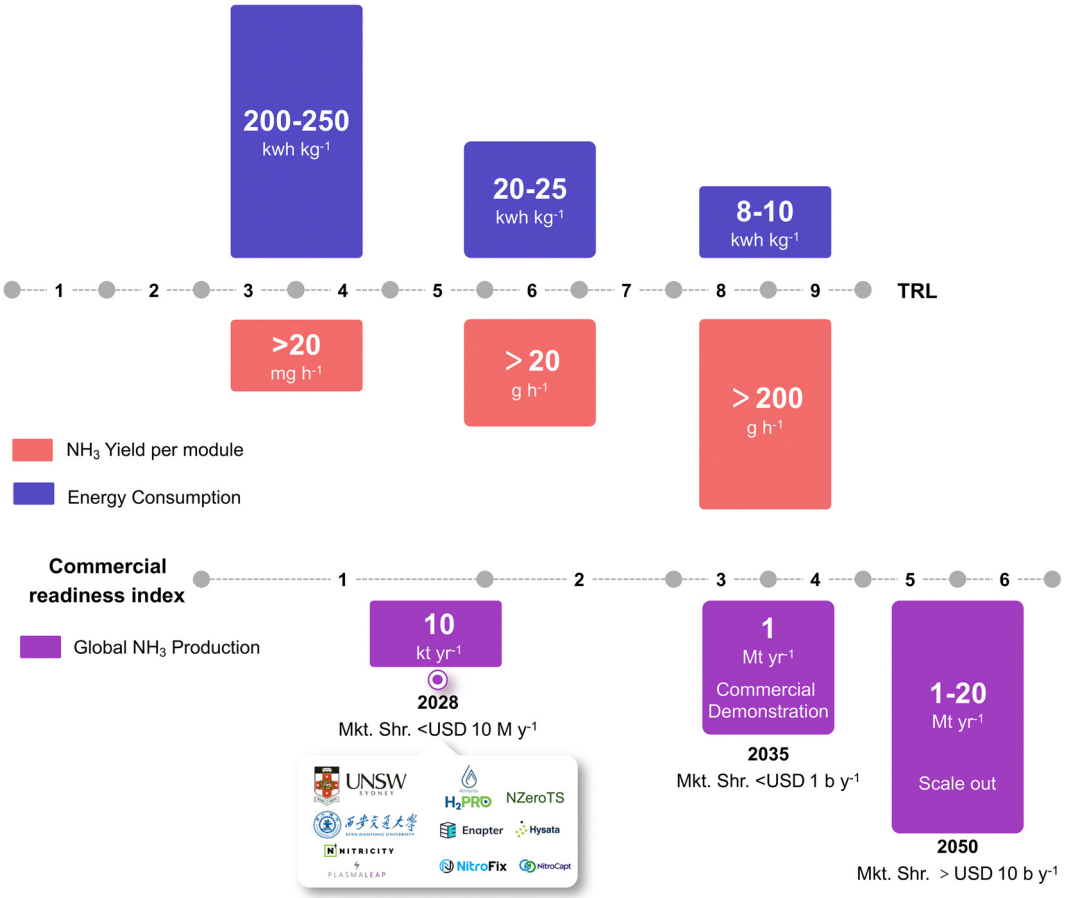

Fig. 16 Commercialisation roadmap for NORR, illustrating TRL milestones, module-level performance benchmarks, alignment with commercial readiness levels, and projected contribution to the global ammonia market by 2050.

Institutional funding mechanisms strongly support this approach. The EU's Innovation Fund has committed over €1 billion to first-of-a-kind clean energy demonstrations, several of which target green ammonia. In the U.S., ARPA-E's REFUEL and SCALEUP initiatives have backed modular, grid-flexible hydrogen and ammonia platforms. In Australia, ARENA has supported projects like the QNP-Jemena consortium, which is advancing renewable hydrogen-to-ammonia integration in Queensland. These programs represent a robust and diverse foundation of technical and financial enablers that help mitigate early-stage risks and reduce LCOA through public procurement, demonstration incentives, and blended finance strategies.

Beyond retrofitting, the mid-to-long-term strategy envisages ammonia production fully decoupled from fossil inputs. This model relies on synthesising ammonia from air, water, and renewable electricity in stand-alone green facilities. More than 20 large-scale projects, spanning eHB retrofits and new electrolysis-based routes, are currently underway or funded across five continents. These projects include demonstration systems in the tens of megawatts, as well as full-scale facilities targeting production volumes in excess of 1 Mt year^{-1}, backed by capital investments ranging from hundreds of millions to several billion US dollars.

One example is the NEOM Green Hydrogen Project in Saudi Arabia, a US$8.4 billion venture by Air Products, ACWA Power, and NEOM, which will use 4 GW of renewable energy to produce 600 tonnes of hydrogen per day, ultimately yielding around 1.2 Mt of green ammonia annually (Air Products, 2023). In Australia, the H2U Eyre Peninsula Gateway Project plans to expand from a 100 MW pilot to a 1.5 GW electrolyser array, enabling production of up to 800 000 tonnes of green ammonia per year (SA Dept. for Energy and Mining, 2023). Similarly, the Australian Renewable Energy Hub (AREH), led by BP, aims to develop 26 GW of wind and solar generation to support 9 Mt of green ammonia and 1.6 Mt of hydrogen per year at full capacity, potentially offsetting 17 Mt of CO_2 annually (BP Australia, 2023).

These ventures employ a diverse range of technologies, including PEMEL, SOEC, and hybrid electrolysis–Haber–Bosch configurations. From an entrepreneurial perspective, they exemplify successful capital mobilisation through public–private partnerships involving sovereign wealth funds, venture capital, and multilateral lenders. The investment structures and deployment models of these projects offer instructive parallels for early-stage NORR systems, especially regarding risk allocation, financing instruments, and policy integration frameworks.

Beyond purely techno-economic considerations, NORR's distributed deployment model presents unique opportunities and challenges with profound socioeconomic and environmental dimensions. Modular plasma–electrolyser systems can be deployed near agricultural hubs, circumventing the high capital costs and rigid supply chains of conventional HB plants. This decentralisation of ammonia production aligns with efforts to stabilise fertiliser prices and ensure equitable access, particularly in regions vulnerable to global fertiliser market fluctuations and geopolitical tensions that have historically shaped ammonia flows. For rural and emerging economies, locally produced ammonia reduces reliance on imported fossil-based fertiliser, bolstering food security and empowering communities to integrate renewable energy for local fertiliser autonomy.

Moreover, by decoupling ammonia synthesis from fossil inputs, distributed NORR systems could foster new value chains around renewable-based nitrogen management. This approach directly supports broader decarbonisation goals, aligning with international initiatives such as the EU Green Deal, Australia's Future Made in Australia policy, and the African Union's Agenda 2063, all of which prioritise resilient, low-carbon agricultural systems as foundational pillars of regional development.

While the environmental and climate benefits of distributed green ammonia production are compelling, careful attention must also be paid to the unintended consequences of NO–NH_3 pathways. The controlled generation and handling of NO, a regulated atmospheric pollutant, requires robust safety protocols and regulatory frameworks to prevent localised air quality degradation. Simultaneously, replacing nitrate-intensive agricultural inputs with localised NO–NH_3 platforms can significantly reduce nitrate runoff and eutrophication in vulnerable water systems, addressing a persistent environmental challenge linked to intensive fertiliser use. Balancing these co-benefits and trade-offs will necessitate proactive engagement with environmental regulators and robust life-cycle assessments that incorporate not just carbon intensity, but also broader ecological impacts and social acceptance considerations.

6.2.2 Short-term (2025–2028): decentralised deployment. The short-term commercialisation roadmap for NORR focuses on decentralised, modular systems designed to operate at capacities below 10 000 t NH_3 $year^{-1}$, collectively. This estimate reflects the current maturity of plasma–electrolyser hybrids at TRL 4–5, where batch-mode NO production and continuous-flow electroreduction have been independently validated under short-duration testing. Pilot systems in this category, such as the 3.6 million USD NSF-funded project at Princeton, target integration under intermittent renewable energy supply and are projected to operate over 100–500 h cycles at modest current densities. These systems are not yet optimised for volumetric throughput but serve to validate operability, energy input profiles, and system stability under cycling loads.

Complementing this, the NSW Environmental Trust, through its CleanTech R&D program, has awarded AU$1.5 million to our laboratory at UNSW and our commercial partner to develop and scale a hybrid plasma–electrolysis system for green ammonia production powered by renewable electricity (NSW Environment, 2024). Companies such as PlasmaLeap and Nitricity are actively developing plasma-based nitrogen fixation platforms, which are crucial for reducing reactor costs and energy intensity, two of the most critical techno-economic parameters outlined in this roadmap. Moreover, companies like Hysata, though focused on high-efficiency hydrogen electrolysers, may support cost reductions in electrolyser stacks for NORR if broader market adoption and investment accelerate.

Deployments below 10 000 t represent a realistic and necessary milestone toward larger commercial systems. They generate critical performance data on FE, gas purity, degradation rates, and interfacial compatibility. These parameters inform refinements to membrane architecture, plasma–catalyst synchronisation, and load-following control. With successful validation and support from agencies such as ARPA-E and ARENA, a limited number of early commercial demonstration units might scale toward the 50–100 t $year^{-1}$ threshold by 2028. However, such outcomes will likely depend on bespoke funding models, public–private partnerships, or pre-commercial offtake agreements.

In this short-term phase (TRL4–5, up to 2028), NORR module-level performance targets are set at $<$200–250 kWh kg^{-1} NH_3 energy intensity and $>$0.02–0.05 g h^{-1} ammonia production per device. These targets correspond to the partial current densities of $\sim$0.001–0.005 g h^{-1} cm^{-2} typical of early demonstration reactors prior to advanced GDE integration. They serve as quantitative benchmarks to validate laboratory-scale viability and inform the progression to more integrated pilot stacks and mid-term deployments.

Importantly, these first deployments function not only as technical proofs-of-concept but also as vehicles for stakeholder alignment, regulatory engagement, and supply chain mobilisation. A useful analogue is the recent commercialisation of electrochemical CO_2-to-CO technologies. Companies such as Twelve scaled from TRL 3 to TRL 6 within five years by deploying modular systems with targeted performance validation, aligned with strategic offtake partnerships.[266] Similar to NORR, these platforms began with $<$10 t $year^{-1}$ deployments, focusing on data generation, stack integration, and dynamic load operation under renewables. The NORR platform can mirror this path by prioritising high-visibility use cases, pre-commercial pilots, and modular BoP engineering.

Importantly, early design of control architectures and diagnostic frameworks will be essential, as CO_2RR scale-up challenges, such as membrane durability, impurity management, and stack balance, are well documented.[267,268] They help validate stack architecture, lifetime cost models, and performance logging systems, laying the foundation for NORR's evolution toward regionalised mid-scale systems in the 2030s.

Small-scale projects can also access enabling policy frameworks, such as ARPA-E's SCALEUP and ARENA's Advancing Renewables Program, both designed to bridge early-stage breakthroughs with field demonstrations and facilitate the transition from TRL 3–5 to pilot-scale deployment.

6.2.3 Mid-term (2028–2035): regional expansion. In the mid-term commercialisation roadmap, the NORR platform progresses from decentralised demonstration systems to regional production facilities operating at capacities that still collectively contribute to below 1 Mt NH_3 $year^{-1}$. This range reflects the practical upper bound for TRL 6–7 systems, consistent with performance and deployment metrics observed in analogous PEMEL[268] and CO_2RR[269] technologies. For instance, PEM electrolysers operating at 1–10 MW scale, typical of TRL 6–7 demonstrations, achieve 200–2000 t H_2 $year^{-1}$. Translated to ammonia synthesis, this equates to 1–10 kt NH_3 $year^{-1}$ only at higher TRLs (8–9), where validated stack lifetimes and industrial-level control redundancy are realised. In these mid-term systems, NORR module-level performance targets of $<$20–25 kWh kg^{-1} NH_3 energy intensity and $>$20 g h^{-1} ammonia production per module, corresponding to partial current densities of $\sim$0.02 g h^{-1} cm^{-2} at $>$70% faradaic efficiency, anchor these production scales and serve as a critical benchmark for engineering scale-up and market readiness.

Our TE analysis shows that by 2035, NORR systems operating at regional scale could reach cost parity with eHB, contingent upon renewable electricity prices falling below US$0.02 per kWh, FE exceeding 90%, and reactor stability beyond 1000 h. These facilities will consolidate improvements from the short-term phase, such as synchronised NO, electrolyser integration and adaptive power management.

At this stage, optimisation of BoP, NO storage and feed systems, and system modularity will enable stable, semi-continuous ammonia production in off-grid or distributed energy environments. Battery buffering or hybrid solar-wind integration will further enhance operational resilience.

Comparable trajectories can be observed in PEMEL commercialisation. Companies like ITM Power and Sunfire achieved mid-scale rollouts (1–10 MW) within five to seven years through a structured approach of off-take agreements and public capital support. Their stacks transitioned from sub-kW lab modules to MW-class platforms by aligning stack hardware development with industrial integration protocols.

NORR can adopt similar strategies. Vertical integration with end-users (*e.g.*, fertiliser blenders, decentralised fuel processors) and standardisation of ammonia quality and origin could position NORR as a differentiated, regionally adaptive platform. Supportive policy instruments, such as Clean Energy Investment Plans, carbon contracts-for-difference, or direct procurement *via* sovereign tenders, could play a pivotal role in enabling this phase.

To further support investment at this stage, surplus renewable electricity presents a compelling opportunity. According to IRENA, global renewable generation capacity is expected to exceed 11 000 GW by 2030, with substantial overcapacity projected in regions such as Australia, MENA, and parts of Africa during non-peak hours.[270] NORR systems offer a dispatchable, value-added load that can monetise this surplus, particularly in settings where grid curtailment or time-of-day pricing creates stranded energy resources.

Ammonia's dual role as a fertiliser input and hydrogen carrier strengthens its commercial case. Distributed NORR systems could serve both local agriculture and emerging maritime fuel markets, offering geographic and market flexibility. With growing momentum behind green product certification, carbon border tariffs, and guarantee-of-origin schemes, decentralised ammonia production can capture regulatory premiums and align with Scope 3 emission strategies. This is particularly relevant as the EU Carbon Border Adjustment Mechanism (CBAM) and Australia's Guarantee of Origin scheme begin to formalise embedded carbon reporting for imported ammonia and derivatives, rewarding decentralised, renewable-based systems with reduced upstream transport emissions and traceable green credentials.[271,272]

Companies already active in PEMEL, SOEL, hydrogen transport, or CO_2RR (*e.g.*, ITM Power, Sunfire, Enapter, Twelve, NetZero Tech Solutions, and Hysata) hold core competencies directly transferrable to NORR. Their platforms in plasma diagnostics, electrolyser design, and balance-of-plant integration position them to pivot or diversify into NORR pathways. Government incentives targeting low-carbon fuels, such as the U.S. Inflation Reduction Act (IRA 45 V), the EU Innovation Fund, and ARENA's clean hydrogen portfolio, may similarly extend support to NORR *via* expanded definitions of renewable fuels of non-biological origin (RFNBOs).

6.2.4 Long-term (post-2035): distributed scale-out. For 2050, we target each ammonia module-level performance of $<$8–10 kWh kg^{-1} NH_3 energy intensity and $>$50–100 kg day^{-1} ammonia production per modular unit, consistent with projected TRL 8–9 systems leveraging optimised GDE interfaces and advanced stack designs. These targets are based on achieving partial ammonia-producing current densities of $\sim$500 mA cm^{-2} at $>$90% faradaic efficiency, corresponding to partial ammonia production rates of $\sim$0.05 g h^{-1} cm^{-2}. This performance enables a modular system with a $\sim$2 m^2 active cathode area to produce 1 kg h^{-1} of ammonia, marking a substantial leap in productivity over current laboratory benchmarks. Explicitly stating these relationships, linking partial current density, faradaic efficiency, production rates, and active area, clarifies the path to bridging laboratory insights with real-world commercial deployment. Moreover, the total number of deployed NORR modules can be dynamically scaled to match local electricity availability, supporting flexible integration with intermittent renewable resources and time-of-day power pricing. However, unlike conventional scale-up pathways that culminate in centralised megatonne plants, the commercial strategy for NORR diverges. Instead of converging toward single-site, capital-intensive facilities, NORR will harness the unique advantages of modularity and distributed deployment.

This distributed model mirrors the broader transformation of the energy sector in the twenty-first century. The electrification is no longer confined to high-value niches but is being modularised, containerised, and replicated through factory-built systems. Our TE analysis confirms that NORR can reach cost parity with eHB by 2035. Yet, its strategic advantage lies not just in competing on price, but in enabling production models that decentralise risk, simplify logistics, and adapt to local renewable supply and demand.

The growing global surplus of variable renewable energy creates stranded generation in many regions, particularly during off-peak periods. Modular NORR systems act as intelligent loads that can monetise this surplus, converting it into ammonia for local fertiliser markets, microgrids, or hydrogen-carrier applications. IRENA's 2023 innovation brief on modular energy systems emphasises this as a foundational transition in renewable-based industrial design.[273]

From a business perspective, the NORR platform unlocks new commercial models. Instead of requiring multi-billion-dollar CAPEX and ten-year build-outs, companies can pursue a ''scale-out'' strategy, rolling out dozens or hundreds of pre-engineered units across distributed sites. This approach reduces permitting complexity, aligns CAPEX with cash flow, and allows for dynamic adjustment to market conditions. Emerging markets in sub-Saharan Africa, Southeast Asia, and rural Australia, where centralised HB supply chains are infeasible, could leapfrog directly to localised ammonia production using containerised NORR systems.

The successful deployment of distributed CO_2RR and hydrogen electrolysis platforms provides a strong precedent. Companies such as Enapter[274] and H_2Pro achieved rapid market entry by focusing on modular hardware, factory-line production, and pre-certified BoP integration. NORR can follow a similar path, with production hubs focused on 10–500 t NH_3 $year^{-1}$ units manufactured in parallel and installed near agricultural demand centres or renewable energy corridors. These decentralised units may exhibit higher capital intensity, estimated at 2000 USD per tonne of annual capacity *versus* 1100 USD for centralised HB, primarily due to the absence of economies of scale and the duplication of BoP and control infrastructure across units. However, this cost structure brings critical benefits. Smaller modular units are more affordable to individual entities or startup ventures, enabling market entry in regions or sectors where centralised facilities would be financially or logistically prohibitive.

Furthermore, they are well-suited to attract venture capital and mission-driven financing by aligning with scalable, low-footprint business models. In effect, the trade-off in capital intensity supports broader affordability and feasibility in distributed deployment, particularly where flexible, just-in-time capacity is needed to capture intermittent renewables and serve localised ammonia demand. Importantly, the techno-economic analysis predicting cost parity with eHB by 2035 accounts for both CAPEX and OPEX, meaning that a similar levelised production cost can be achieved despite higher capital intensity. For every 1 million USD invested in a decentralised NORR unit, approximately 200 000 USD in annual operating margin is achievable. In contrast, a centralised eHB system, requiring around 3 billion USD in CAPEX, generates a comparatively lower return per dollar invested. For example, a decentralised NORR unit producing 500 t NH_3 $year^{-1}$ is expected to cost ~1 million USD in CAPEX, with OPEX around 150 000 USD per year. This results in an estimated annual operating margin of 200 000 USD based on total output and cost structure. In contrast, a centralised eHB plant producing 1 Mt NH_3 $year^{-1}$ would likely require 2–3 billion USD in CAPEX due to the need for both large-scale electrolyser capacity and synthesis infrastructure and incur annual OPEX exceeding 400 million USD. While centralised systems benefit from economies of scale, they also face significant costs related to ammonia transport, export infrastructure, and storage logistics. NORR systems avoid these overheads by situating production near end users or renewable corridors, cutting delivery emissions, and enabling monetisation of carbon credits. Their modularity supports rapid deployment, phased investment, and eligibility for decentralised energy incentives and Scope 3 emissions reporting schemes. These attributes make NORR not only technically competitive but also financially attractive, particularly for startups, regional developers, and investors seeking scalable, low-footprint solutions aligned with energy and climate transitions.

This modular future also aligns with policy directions. The decentralisation of industrial capacity is a priority in many national energy strategies. Australia's Future Made in Australia Act, the EU's Net-Zero Industry Act, and localised fertiliser initiatives in India and Africa all provide avenues for NORR adoption under government-backed procurement and green industrial policy. Carbon border tariffs, Scope 3 emissions reporting, and the Guarantee of Origin (GO) scheme will further strengthen the case for local, low-emissions ammonia.

In this context, even if NORR reaches cost parity with eHB, it offers strategic value through resilience, localisation, and compatibility with intermittent power. Its future does not hinge on displacing HB in centralised settings but on providing an alternative where centralisation is a weakness, not a strength. The long-term vision for NORR is not just one of technical feasibility, but of reconfiguring the geography and economics of ammonia supply for a distributed energy world. Taken together, these insights show that NORR is not a derivative of legacy ammonia systems, but a fundamentally different platform, purpose-built for decentralised energy conditions, modular industrial policy, and region-specific deployment models. We therefore invite the electrochemical, plasma-physics, and agricultural-economics communities to adopt the quantitative milestones catalogued herein and to converge experimental, modelling, and policy efforts on this five-electron route to green ammonia.

Conflicts of interest

A. R. is a minor shareholder of PlasmaLeap. A. R. J. serves as an advisor to PlasmaLeap, primarily on plasma reactor development, and is the director of NetZero Tech Solutions, a company focused on developing green technologies.

Data availability

The data supporting this article have been included as part of the SI. Supplementary information for Density Function Theory (DFT) Method and Techno-economic assessment. See DOI: **https://doi.org/10.1039/d5ee03443d**

Acknowledgements

This work was supported by the National Key Research and Development Program of China (2023YFE0120900), the National Natural Science Foundation of China (Grant No. 52377160), the National Natural Science Foundation of China National Young Talents Project (GYKP010). Australian Research Council (ARC) Future Fellowship Award FT230100396 (A. R. J.) and ARC Discovery Early Career Research Award DE230101617 (D.E).

References

1 N. Lazouski, M. Chung, K. Williams, M. L. Gala and K. Manthiram, *Nat. Catal.*, 2020, **3**, 463–469.
2 S. Z. Andersen, M. J. Statt, V. J. Bukas, S. G. Shapel, J. B. Pedersen, K. Krempl, M. Saccoccio, D. Chakraborty, J. Kibsgaard and P. C. Vesborg, *Energy Environ. Sci.*, 2020, **13**, 4291–4300.
3 A. Klerke, C. H. Christensen, J. K. Nørskov and T. Vegge, *J. Mater. Chem.*, 2008, **18**, 2304–2310.
4 L. Zhou, L. Zhong, Z. Liu and H. Wei, *Fuel*, 2023, **352**, 129009.
5 K. Li, S. G. Shapel, D. Hochfilzer, J. B. Pedersen, K. Krempl, S. Z. Andersen, R. Sažinas, M. Saccoccio, S. Li and D. Chakraborty, *ACS Energy Lett.*, 2021, **7**, 36–41.
6 M. Capdevila-Cortada, *Nat. Catal.*, 2019, **2**, 1055.
7 I. McPherson and J. Zhang, *Joule*, 2020, **4**, 12–14.
8 J. W. Erisman, M. A. Sutton, J. Galloway, Z. Klimont and W. Winiwarter, *Nat. Geosci.*, 2008, **1**, 636–639.
9 C. J. M. van der Ham, M. T. M. Koper and D. G. H. Hetterscheid, *Chem. Soc. Rev.*, 2014, **43**, 5183–5191.
10 H. Jiang, T. Li, Y. Gao, J. Fan, D. Gan, S. Yuan, L. Hong, Y. Feng, J. Sun, Q. Song, T. Zhang, A. R. Jalili, P. J. Cullen and R. Zhou, *J. Energy Chem.*, 2025, **105**, 630–668.
11 Z. J. Schiffer and K. Manthiram, *Joule*, 2017, **1**, 10–14.
12 D. S. Mallapragada, Y. Dvorkin, M. A. Modestino, D. V. Esposito, W. A. Smith, B.-M. Hodge, M. P. Harold, V. M. Donnelly, A. Nuz, C. Bloomquist, K. Baker, L. C. Grabow, Y. Yan, N. N. Rajput, R. L. Hartman, E. J. Biddinger, E. S. Aydil and A. D. Taylor, *Joule*, 2023, **7**, 23–41.
13 P. Koschwitz, D. Bellotti, C. Liang and B. Epple, *Int. J. Hydrogen Energy*, 2022, **47**, 25322–25334.
14 Electrolysers – energy system, **https://www.iea.org/energy-system/low-emission-fuels/electrolysers**, (accessed June 6, 2025).
15 H. Sayed-Ahmed, Á. I. Toldy and A. Santasalo-Aarnio, *Renewable Sustainable Energy Rev.*, 2024, **189**, 113883.
16 A. Hassan, O. Abdel-Rahim, M. Bajaj and I. Zaitsev, *Sci. Rep.*, 2024, **14**, 24767.
17 Y. Kim, L. K. Park, S. Yiacoumi and C. Tsouris, *Annu. Rev. Chem. Biomol. Eng.*, 2017, **8**, 359–380.
18 D. R. MacFarlane, J. Choi, B. H. Suryanto, R. Jalili, M. Chatti, L. M. Azofra and A. N. Simonov, *Adv. Mater.*, 2020, **32**, 1904804.
19 L. Cheng, L. Qi, X. Tang, X. Li, L. Chen, W. Min, Z. Mei, R. Gao, M. Sun, J. Xiao, Q. Guan, M. Yu and Z. Sun, *Int. J. Hydrogen Energy*, 2024, **83**, 499–511.
20 P. Mayer, A. Ramirez, G. Pezzella, B. Winter, S. M. Sarathy, J. Gascon and A. Bardow, *iScience*, 2023, **26**, 107389.
21 W. H. Avery, *Int. J. Hydrogen Energy*, 1988, **13**, 761–773.
22 E. Spatolisano, L. A. Pellegrini, A. R. de Angelis, S. Cattaneo and E. Roccaro, *Ind. Eng. Chem. Res.*, 2023, **62**, 10813–10827.
23 J. Hansson, S. Brynolf, E. Fridell and M. Lehtveer, *Sustainability*, 2020, **12**, 3265.
24 B. Bonnet-Cantalloube, M. Espitalier-Noël, P. F. de Carvalho and G. Pawelec, Clean Ammonia in the Future Energy System, *Hydrogen Europe*, **2023**, **https://hydrogeneurope.eu/wp-content/uploads/2023/03/2023.03_H2Europe_Clean_Ammonia_Report_DIGITAL_FINAL.pdf**.
25 D. Yao, C. Tang, P. Wang, H. Cheng, H. Jin, L.-X. Ding and S.-Z. Qiao, *Chem. Eng. Sci.*, 2022, **257**, 117735.
26 Y. Cheng, X. Xu, M. Wang, C. Deng, Y. Sun, C. Yan and T. Qian, *Adv. Funct. Mater.*, 2023, **33**, 2302332.
27 K. C. Ranjeesh, S. Kaur, A. K. Mohammed, S. Gaber, D. Gupta, K. Badawy, M. Aslam, N. Singh, T. Skorjanc, M. Finšgar, J. Raya, T. C. Nagaiah and D. Shetty, *Adv. Energy Mater.*, 2024, **14**, 2303068.
28 H.-P. Jia and E. A. Quadrelli, *Chem. Soc. Rev.*, 2014, **43**, 547–564.
29 J. Kundu, T. Bhoyar, S. Park, H. Jin, K. Lee and S.-I. Choi, *Adv. Powder Mater.*, 2025, **4**, 100279.
30 H.-L. Du, M. Chatti, R. Y. Hodgetts, P. V. Cherepanov, C. K. Nguyen, K. Matuszek, D. R. MacFarlane and A. N. Simonov, *Nature*, 2022, **609**, 722–727.
31 A. Bagger, R. Tort, M.-M. Titirici, A. Walsh and I. E. Stephens, *ACS Energy Lett.*, 2024, **9**, 4947–4952.
32 B. Izelaar, M. Ramdin, A. Vlierboom, M. Pérez-Fortes, D. Van Der Slikke, A. S. Kumar, W. de Jong, F. M. Mulder and R. Kortlever, *Energy Environ. Sci.*, 2024, **17**, 7983–7998.
33 Y. Wang, C. Wang, M. Li, Y. Yu and B. Zhang, *Chem. Soc. Rev.*, 2021, **50**, 6720–6733.
34 T. Yuan, M. Li, S. Subramanian, J. Kok, M. Li, A. Urakawa, O. Voznyy and T. Burdyny, *Cell Rep. Phys. Sci.*, 2024, **6**, 101977.
35 L. Zhang, Y. Cai, Y. Li, C. Sun, Y. Xiao, Y. Yang, D. Chen, D. Xiao, C.-F. Lee, Y. Wang, S. Feng, H.-T. Wang, Y.-C. Shao, T.-S. Chan, H. Ishii, N. Hiraoka, X. Wang, J. Luo and L. Han, *Energy Environ. Sci.*, 2025, **18**, 2804–2816.
36 L. Barrera and R. B. Chandran, *Meet. Abstr.*, 2021, **MA2021-01**, 1246.
37 G. Yang, P. Zhou, J. Liang, H. Li and F. Wang, *Inorg. Chem. Front.*, 2023, **10**, 4610–4631.
38 A. A. Lee, C. S. Perez-Martinez, A. M. Smith and S. Perkin, *Phys. Rev. Lett.*, 2017, **119**, 026002.
39 K. Zhang, X. Zou, Y. Liu, X. Zhang and L. An, *iScience*, 2024, 111229.
40 J. Guo, M. J. Liu, C. Laguna, D. M. Miller, K. S. Williams, B. D. Clark, C. Muñoz, S. J. Blair, A. C. Nielander and T. F. Jaramillo, *Energy Environ. Sci.*, 2024, **17**, 8787–8800.
41 J. Li, C. Lan, L. Nie, D. Liu and X. Lu, *Chem. Eng. J.*, 2023, **478**, 147483.
42 J. Sun, R. Zhou, J. Hong, Y. Gao, Z. Qu, Z. Liu, D. Liu, T. Zhang, R. Zhou, K. (Ken) Ostrikov, P. Cullen, E. C. Lovell, R. Amal and A. R. Jalili, *Appl. Catal., B*, 2024, **342**, 123426.

43 V. D. Rusanov, A. Fridman and G. V. Sholin, *Sov. Phys.*, 1981, **24**, 447.
44 K. H. Rouwenhorst, F. Jardali, A. Bogaerts and L. Lefferts, *Energy Environ. Sci.*, 2023, **16**, 6170–6173.
45 Y. Li, Y. Huang, H. Zhang, X. Wang, L. Gao, Y. Zhang, Y. Liao, J. Meng, Y. Cui and W.-L. Dai, *Appl. Catal., B*, 2025, **361**, 124657.
46 J. Long, S. Chen, Y. Zhang, C. Guo, X. Fu, D. Deng and J. Xiao, *Angew. Chem., Int. Ed.*, 2020, **59**, 9711–9718.
47 J. Liang, W.-F. Hu, B. Song, T. Mou, L. Zhang, Y. Luo, Q. Liu, A. A. Alshehri, M. S. Hamdy and L.-M. Yang, *Inorg. Chem. Front.*, 2022, **9**, 1366–1372.
48 B. H. Ko, B. Hasa, H. Shin, Y. Zhao and F. Jiao, *J. Am. Chem. Soc.*, 2022, **144**, 1258–1266.
49 J. Mante and C. J. Myers, *Nat. Commun.*, 2023, **14**, 2953.
50 H. R. Inta, D. Dhanabal, S. S. Markandaraj and S. Shanmugam, *EES Catal.*, 2023, **1**, 645–664.
51 X. Fan, S. Kang, J. Li and T. Zhu, *Water, Air, Soil Pollut.*, 2018, **229**, 351.
52 H. U. Rasheed, J. Shim, J. H. Kim, K. Lee, S. H. Kim, H. Jung and H. C. Yoon, *Electrochim. Acta*, 2025, **530**, 146412.
53 T. Burdyny and W. A. Smith, *Energy Environ. Sci.*, 2019, **12**, 1442–1453.
54 X. Mao, X. Bai, G. Wu, Q. Qin, A. P. O'Mullane, Y. Jiao and A. Du, *J. Am. Chem. Soc.*, 2024, **146**, 18743–18752.
55 J. Cai, J. Huang, A. Cao, Y. Wei, H. Wang, X. Li, Z. Jiang, G. I. N. Waterhouse, S. Lu and S.-Q. Zang, *Appl. Catal., B*, 2023, **328**, 122473.
56 Z. Wu, Y. Song, Y. Liu, W. Luo, W. Li and J. Yang, *Chem. Catal.*, 2023, **3**, 100786.
57 H. Wang, J. Huang, J. Cai, Y. Wei, A. Cao, B. Liu and S. Lu, *Small Methods*, 2023, **7**, 2300169.
58 Y. Kwon, S. K. Kim, Y. B. Kim, S. J. Son, G. D. Nam, H. J. Park, W.-C. Cho, H. C. Yoon and J. H. Joo, *ACS Energy Lett.*, 2021, **6**, 4165–4172.
59 G. Linling, Z. Liao, H. Zhang, J. Jiang and Z. Chen, *Front. Chem.*, 2024, **12**, 1452689.
60 A. C. A. de Vooys, G. L. Beltramo, B. van Riet, J. A. R. van Veen and M. T. M. Koper, *Electrochim. Acta*, 2004, **49**, 1307–1314.
61 S.-C. Kuo, Z. Zhang, S. K. Ross, R. B. Klemm, R. D. Johnson, P. S. Monks, R. P. Thorn and L. J. Stief, *J. Phys. Chem. A*, 1997, **101**, 4035–4041.
62 D. Wang, Z.-W. Chen, K. Gu, C. Chen, Y. Liu, X. Wei, C. V. Singh and S. Wang, *J. Am. Chem. Soc.*, 2023, **145**, 6899–6904.
63 K. Zhang, Y. Liu, Z. Pan, Q. Xia, X. Huo, O. C. Esan, X. Zhang and L. An, *EES Catal.*, 2024, **2**, 727–752.
64 H. Liu, L. Bai, A. Bergmann, B. R. Cuenya and J. Luo, *Chem*, 2024, **10**, 2963–2986.
65 W. Song, W. Peng, P. Ma, X. Liu, Y. Guo, C. He and L. Fu, *Appl. Surf. Sci.*, 2022, **597**, 153678.
66 J. Wang, T. Feng, J. Chen, V. Ramalingam, Z. Li, D. M. Kabtamu, J.-H. He and X. Fang, *Nano Energy*, 2021, **86**, 106088.
67 I. Ledezma-Yanez, W. D. Z. Wallace, P. Sebastián-Pascual, V. Climent, J. M. Feliu and M. T. M. Koper, *Nat. Energy*, 2017, **2**, 1–7.
68 S. Chen, S. Perathoner, C. Ampelli, C. Mebrahtu, D. Su and G. Centi, *ACS Sustainable Chem. Eng.*, 2017, **5**, 7393–7400.
69 G.-F. Chen, Y. Yuan, H. Jiang, S.-Y. Ren, L.-X. Ding, L. Ma, T. Wu, J. Lu and H. Wang, *Nat. Energy*, 2020, **5**, 605–613.
70 S. Cheon, W. J. Kim, D. Y. Kim, Y. Kwon and J.-I. Han, *ACS Energy Lett.*, 2022, **7**, 958–965.
71 M. C. Monteiro, M. F. Philips, K. J. P. Schouten and M. T. Koper, *Nat. Commun.*, 2021, **12**, 4943.
72 S. Brosch, E. Häger, O. Frank, P. Scholz, W. Plischka and M. Wessling, *Chem*, 2025, **1**, 102582.
73 C.-T. Dinh, T. Burdyny, M. G. Kibria, A. Seifitokaldani, C. M. Gabardo, F. P. García de Arquer, A. Kiani, J. P. Edwards, P. De Luna, O. S. Bushuyev, C. Zou, R. Quintero-Bermudez, Y. Pang, D. Sinton and E. H. Sargent, *Science*, 2018, **360**, 783–787.
74 J. Theerthagiri, K. Karuppasamy, A. H. Mahadi, C. J. Moon, N. Rahamathulla, S. Kheawhom, S. Alameri, A. Alfantazi, A. P. Murthy and M. Y. Choi, *Environ. Chem. Lett.*, 2024, **22**, 189–208.
75 D. Richards, S. D. Young, B. R. Goldsmith and N. Singh, *Catal. Sci. Technol.*, 2021, **11**, 7331–7346.
76 B. H. Ko, B. Hasa, H. Shin, Y. Zhao and F. Jiao, *J. Am. Chem. Soc.*, 2022, **144**, 1258–1266.
77 D. M. Beagan, A. C. Cabelof, M. Pink, V. Carta, X. Gao and K. G. Caulton, *Chem. Sci.*, 2021, **12**, 10664–10672.
78 W. Duan, Y. Li, Y. Ou, H. Tuo, L. Tian, Y. Zhu, H. Fu, W. Zheng and C. Feng, *Environ. Sci. Technol.*, 2025, **59**, 3263–3275.
79 L. Mattarozzi, S. Cattarin, N. Comisso, P. Guerriero, M. Musiani, L. Vázquez-Gómez and E. Verlato, *Electrochim. Acta*, 2013, **89**, 488–496.
80 R. Jia, X. Zhang, L. Gan, M. Tahir, Z.-F. Huang, L. Pan, R. Gao, C. Shi, X. Zhang and G. Yang, *J. Mater. Chem. A*, 2025, **13**, 5732–5743.
81 K. P. Kuhl, E. R. Cave, D. N. Abram and T. F. Jaramillo, *Energy Environ. Sci.*, 2012, **5**, 7050–7059.
82 S. S. Markandaraj, D. Dhanabal and S. Shanmugam, *J. Mater. Chem. A*, 2023, **11**, 23479–23488.
83 R. Zeng, Y. Yang, X. Feng, H. Li, L. M. Gibbs, F. J. DiSalvo and H. D. Abruña, *Sci. Adv.*, 2022, **8**, eabj1584.
84 S. Yu, J. Xu, Q. Wang, Y. Zou, C. Xiang, F. Xu, L. Sun, M. Jiang, Z. Hu and X. Hu, *J. Alloys Compd.*, 2024, **977**, 173433.
85 W. Ding and W. Li, *Chin. J. Catal.*, 2014, **35**, 1937–1943.
86 F. C. Ballotin, T. Hartman, J. Koek, R. G. Geitenbeek and B. M. Weckhuysen, *ChemPhysChem*, 2021, **22**, 1595–1602.
87 M. Zhong, K. Tran, Y. Min, C. Wang, Z. Wang, C.-T. Dinh, P. De Luna, Z. Yu, A. S. Rasouli, P. Brodersen, S. Sun, O. Voznyy, C.-S. Tan, M. Askerka, F. Che, M. Liu, A. Seifitokaldani, Y. Pang, S.-C. Lo, A. Ip, Z. Ulissi and E. H. Sargent, *Nature*, 2020, **581**, 178.
88 P. Babar and G. G. Botte, *ACS Sustainable Chem. Eng.*, 2024, **12**, 13030–13047.
89 H. Wang and H. D. Abruña, *J. Am. Chem. Soc.*, 2025, **147**, 9352–9364.

90 V. Roth, M. Valter-Lithander, L. Strandberg, M. R. Bilesan, J. Järlebark, J. Jamroz and B. Wickman, *Electrochim. Acta*, 2024, **507**, 145137.
91 M. R. Al Fauzan, T. N. Pham, H. H. Halim, Y. Hamamoto, K. Inagaki, I. Hamada and Y. Morikawa, *J. Phys. Chem. C*, 2023, **127**, 19451–19467.
92 D. H. Kim, S. Ringe, H. Kim, S. Kim, B. Kim, G. Bae, H.-S. Oh, F. Jaouen, W. Kim and H. Kim, *Nat. Commun.*, 2021, **12**, 1856.
93 Z.-H. Zeng, J. L. Da Silva and W.-X. Li, *Phys. Chem. Chem. Phys.*, 2010, **12**, 2459.
94 Y. Wong, H. H. Halim, N. F. Khairudin, T. N. Pham, S. E. Putra, Y. Hamamoto, K. Inagaki, I. Hamada, A. R. Mohamed and Y. Morikawa, *J. Phys. Chem. C*, 2021, **125**, 21902.
95 Y. Bu, C. Wang, W. Zhang, X. Yang, J. Ding and G. Gao, *Angew. Chem.*, 2023, **135**, e202217337.
96 D. Vione, G. Falletti, V. Maurino, C. Minero, E. Pelizzetti, M. Malandrino, R. Ajassa, R. Olariu and C. Arsene, *Environ. Sci. Technol.*, 2006, **40**, 3775–3781.
97 L. Yue, W. Song, L. Zhang, Y. Luo, Y. Wang, T. Li, B. Ying, S. Sun, D. Zheng and Q. Liu, *Small Struct.*, 2023, **4**, 2300168.
98 J. Sun, D. Alam, R. Daiyan, H. Masood, T. Zhang, R. Zhou, P. J. Cullen, E. C. Lovell, A. (Rouhollah) Jalili and R. Amal, *Energy Environ. Sci.*, 2021, **14**, 865–872.
99 E. Pérez-Gallent, M. C. Figueiredo, I. Katsounaros and M. T. Koper, *Electrochim. Acta*, 2017, **227**, 77–84.
100 E. Murphy, Y. Liu, I. Matanovic, M. Rüscher, Y. Huang, A. Ly, S. Guo, W. Zang, X. Yan and A. Martini, *Nat. Commun.*, 2023, **14**, 4554.
101 S. Nazari, A. Najmi, P. Kumar, A. Zavabeti, F. Allioux, A. R. Natarajan, D. Esrafilzadeh and A. R. Jalili, *Small*, 2025, 2504087.
102 J. Long, C. Guo, X. Fu, H. Jing, G. Qin, H. Li and J. Xiao, *J. Phys. Chem. Lett.*, 2021, **12**, 6988–6995.
103 T. N. Nguyen and C.-T. Dinh, *Chem. Soc. Rev.*, 2020, **49**, 7488–7504.
104 T. Ito, J. Raj, T. Zhang, S. Roy and J. Wu, *EES Catal.*, 2024, **2**, 997–1005.
105 C. Park, M. Y. Seo, T. Kwon, J. Kim, K. M. Nam, Y. Kim and J. Chang, *J. Am. Chem. Soc.*, 2024, **147**, 687–700.
106 L. Li, Y. Liu, Y. Zhang and D. Chao, *Matter*, 2025, **10**, 75–85.
107 Q. Wu, X. Fan, B. Shan, L. Qi, X. Quan and Y. Liu, *Nat. Commun.*, 2025, **16**, 3479.
108 D. Kim, D. Shin, J. Heo, H. Lim, J.-A. Lim, H. M. Jeong, B.-S. Kim, I. Heo, I. Oh and B. Lee, *ACS Energy Lett.*, 2020, **5**, 3647–3656.
109 A. Singh-Morgan, K. Trösch, A. Weinfurter, M. Inniger, Y.-Z. Xu and V. Mougel, *Chem*, 2025, 102460.
110 K. H. R. Rouwenhorst, A. G. J. Van der Ham, G. Mul and S. R. A. Kersten, *Renewable Sustainable Energy Rev.*, 2019, **114**, 109339.
111 G. Ruan, F. Todman, G. Yogev, R. Arad, T. Smolinka, J. O. Jensen, M. D. Symes and A. Rothschild, *Nat. Rev. Clean Technol.*, 2025, 1–16.
112 W. Yang, H. Liu, X. Chang, Y. Zhang, Y. Cai, Y. Li, Y. Cui, B. Xu, L. Yu and X. Cui, *Nat. Commun.*, 2025, **16**, 1257.
113 P. S. Lamoureux, A. R. Singh and K. Chan, *ACS Catal.*, 2019, **9**, 6194–6201.
114 P. M. Krzywda, A. Paradelo Rodríguez, N. E. Benes, B. T. Mei and G. Mul, *ChemElectroChem*, 2022, **9**, e202101273.
115 M. Decker, Q. Lenne, J. Ghilane and C. M. Sánchez-Sánchez, *Curr. Opin. Electrochem.*, 2025, 101728.
116 A. S. Fajardo, P. Westerhoff, S. Garcia-Segura and C. M. Sánchez-Sánchez, *Sep. Purif. Technol.*, 2023, **321**, 124233.
117 Z. Wang, Z.-L. Guan and B.-L. Su, *Chem. Synth.*, 2025, **5**, 20.
118 Z. Xu, L. Wan, Y. Liao, M. Pang, Q. Xu, P. Wang and B. Wang, *Nat. Commun.*, 2023, **14**, 1619.
119 Y. Huang, C. He, C. Cheng, S. Han, M. He, Y. Wang, N. Meng, B. Zhang, Q. Lu and Y. Yu, *Nat. Commun.*, 2023, **14**, 7368.
120 H. Rabiee, L. Ge, X. Zhang, S. Hu, M. Li, S. Smart, Z. Zhu and Z. Yuan, *Appl. Catal., B*, 2021, **286**, 119945.
121 L. Chen, Q. Li, B. Li, W. Sun, J. Ma and W. Wang, *Mol. Catal.*, 2023, **549**, 113531.
122 Y. Xiong, Y. Li, S. Wan, Y. Yu, S. Zhang and Q. Zhong, *J. Hazard. Mater.*, 2022, **430**, 128451.
123 T. Wei, H. Bao, X. Wang, S. Zhang, Q. Liu, J. Luo and X. Liu, *ChemCatChem*, 2023, **15**, e202201411.
124 A. C. A. de Vooys, M. T. M. Koper, R. A. van Santen and J. A. R. van Veen, *J. Catal.*, 2001, **202**, 387–394.
125 H.-J. Chun, V. Apaja, A. Clayborne, K. Honkala and J. Greeley, *ACS Catal.*, 2017, **7**, 3869–3882.
126 Y. Li, C. Cheng, S. Han, Y. Huang, X. Du, B. Zhang and Y. Yu, *ACS Energy Lett.*, 2022, **7**, 1187–1194.
127 J. Shi, C. Wang, R. Yang, F. Chen, N. Meng, Y. Yu and B. Zhang, *Sci. China Chem.*, 2021, **64**, 1493–1497.
128 H. Zhang, Y. Li, C. Cheng, J. Zhou, P. Yin, H. Wu, Z. Liang, J. Zhang, Q. Yun and A. Wang, *Angew. Chem.*, 2023, **135**, e202213351.
129 K. Zou, X. Wang and Y. Deng, *J. Mater. Chem. A*, 2025, **13**, 2338.
130 J. Shao, H. Jing, P. Wei, X. Fu, L. Pang, Y. Song, K. Ye, M. Li, L. Jiang and J. Ma, *Nat. Energy*, 2023, **8**, 1273–1283.
131 Z. Li, Q. Zhou, J. Liang, L. Zhang, X. Fan, D. Zhao, Z. Cai, J. Li, D. Zheng, X. He, Y. Luo, Y. Wang, B. Ying, H. Yan, S. Sun, J. Zhang, A. A. Alshehri, F. Gong, Y. Zheng and X. Sun, *Small*, 2023, **19**, 2300291.
132 S. Zhang, Q. Liu, X. Tang, Z. Zhou, T. Fan, Y. You, Q. Zhang, S. Zhang, J. Luo and X. Liu, *Front. Chem. Sci. Eng.*, 2023, **17**, 726–734.
133 Z. Li, Z. Ma, J. Liang, Y. Ren, T. Li, S. Xu, Q. Liu, N. Li, B. Tang, Y. Liu, S. Gao, A. A. Alshehri, D. Ma, Y. Luo, Q. Wu and X. Sun, *Mater. Today Phys.*, 2022, **22**, 100586.
134 J. Liang, Q. Zhou, T. Mou, H. Chen, L. Yue, Y. Luo, Q. Liu, M. S. Hamdy, A. A. Alshehri and F. Gong, *Nano Res.*, 2022, **15**, 4008–4013.
135 Y. Bai and M. Mavrikakis, *J. Phys. Chem. B*, 2017, **122**, 432–443.
136 A. Mahata, K. S. Rawat, I. Choudhuri and B. Pathak, *Sci. Rep.*, 2016, **6**, 25590.

137 S. Zhao, M. Chang, J. Liu, G. Shi, Y. Yang, H. Gu, J. Zhang, C. Yang, H. Tong and C. Zhu, *Chem. Catal.*, 2023, **3**(6), 100598.
138 T. Tong, Y. Linghu, G. Wu, C. Wang and C. Wu, *Phys. Chem. Chem. Phys.*, 2022, **24**, 18943–18951.
139 K. Chen, J. Wang, J. Kang, X. Lu, X. Zhao and K. Chu, *Appl. Catal., B*, 2023, **324**, 122241.
140 X. Li, K. Chen, X. Lu, D. Ma and K. Chu, *Chem. Eng. J.*, 2023, **454**, 140333.
141 Y. Lin, J. Liang, H. Li, L. Zhang, T. Mou, T. Li, L. Yue, Y. Ji, Q. Liu and Y. Luo, *Mater. Today Phys.*, 2022, **22**, 100611.
142 K. Chen, Y. Zhang, J. Xiang, X. Zhao, X. Li and K. Chu, *ACS Energy Lett.*, 2023, **8**, 1281–1288.
143 S. Sethuram Markandaraj, T. Muthusamy and S. Shanmugam, *Adv. Sci.*, 2022, **9**, 2201410.
144 K. Chen, J. Wang, J. Kang, X. Lu, X. Zhao and K. Chu, *Appl. Catal., B*, 2023, **324**, 122241.
145 K. Chen, J. Wang, H. Zhang, D. Ma and K. Chu, *Nano Lett.*, 2023, **23**, 1735–1742.
146 J. Theerthagiri, K. Karuppasamy, A. H. Mahadi, C. J. Moon, N. Rahamathulla, S. Kheawhom, S. Alameri, A. Alfantazi, A. P. Murthy and M. Y. Choi, *Environ. Chem. Lett.*, 2024, **22**, 189–208.
147 L. Xiao, S. Mou, W. Dai, W. Yang, Q. Cheng, S. Liu and F. Dong, *Angew. Chem., Int. Ed.*, 2024, **63**, e202319135.
148 Z. Wu, Y. Liu, D. Wang, Y. Zhang, K. Gu, Z. He, L. Liu, H. Liu, J. Fan and C. Chen, *Adv. Mater.*, 2024, **36**, 2309470.
149 X. Li, G. Zhang, P. Shen, X. Zhao and K. Chu, *Inorg. Chem. Front.*, 2023, **10**, 280–287.
150 Q. Liu, Y. Lin, L. Yue, J. Liang, L. Zhang, T. Li, Y. Luo, M. Liu, J. You and A. A. Alshehri, *Nano Res.*, 2022, **15**, 5032–5037.
151 T. Mou, J. Liang, Z. Ma, L. Zhang, Y. Lin, T. Li, Q. Liu, Y. Luo, Y. Liu and S. Gao, *J. Mater. Chem. A*, 2021, **9**, 24268–24275.
152 X. Wang, L. Yang, G. Zhang and K. Chu, *New J. Chem.*, 2023, **47**, 17769–17774.
153 L. Zhang, Q. Zhou, J. Liang, L. Yue, T. Li, Y. Luo, Q. Liu, N. Li, B. Tang and F. Gong, *Inorg. Chem.*, 2022, **61**, 8096–8102.
154 K. Chen, G. Zhang, X. Li, X. Zhao and K. Chu, *Nano Res.*, 2023, **16**, 5857–5863.
155 X. Li, K. Chen, X. Lu, D. Ma and K. Chu, *Chem. Eng. J.*, 2023, **454**, 140333.
156 X. Peng, Y. Mi, H. Bao, Y. Liu, D. Qi, Y. Qiu, L. Zhuo, S. Zhao, J. Sun and X. Tang, *Nano Energy*, 2020, **78**, 105321.
157 J. Xi, H. S. Jung, Y. Xu, F. Xiao, J. W. Bae and S. Wang, *Adv. Funct. Mater.*, 2021, **31**, 2008318.
158 J. Wang, K. Li, Q. Hao, D. Liu and X. Zhang, *Chin. Chem. Lett.*, 2023, **34**, 107567.
159 Q. Wu, W. Wei, X. Lv, Y. Wang, B. Huang and Y. Dai, *J. Phys. Chem. C*, 2019, **123**, 31043–31049.
160 L. Ouyang, Q. Zhou, J. Liang, L. Zhang, L. Yue, Z. Li, J. Li, Y. Luo, Q. Liu and N. Li, *J. Colloid Interface Sci.*, 2022, **616**, 261–267.
161 N. Saeidi, M. D. Esrafili and J. J. Sardroodi, *Appl. Surf. Sci.*, 2021, **544**, 148869.
162 S. Ji and J. Zhao, *New J. Chem.*, 2018, **42**, 16346–16353.
163 Q. Wu, H. Wang, S. Shen, B. Huang, Y. Dai and Y. Ma, *J. Mater. Chem. A*, 2021, **9**, 5434–5441.
164 Y. Zang, Q. Wu, S. Wang, B. Huang, Y. Dai and Y. Ma, *Mater. Horiz.*, 2023, **10**, 2160–2168.
165 Y. Li, J. Nie, D. Gao, S. Zhao, Y. Zhang, B. Bian, Z. Guo, Y. Huang, Y. Fang and C. Tang, *Fuel*, 2023, **339**, 126943.
166 J. Nie, Y. Li, D. Gao, Y. Fang, J. Lin, C. Tang and Z. Guo, *Phys. Chem. Chem. Phys.*, 2024, **26**, 2539–2547.
167 K. Li, Z. Shi, L. Wang, W. Wang, Y. Liu, H. Cheng, Y. Yang and L. Zhang, *J. Hazard. Mater.*, 2023, **448**, 130890.
168 N. Saeidi and M. D. Esrafili, *Int. J. Hydrogen Energy*, 2023, **48**, 19509–19521.
169 N. V. R. Nulakani, V. S. K. Choutipalli and M. A. Ali, *Appl. Surf. Sci.*, 2025, **680**, 161470.
170 Z. W. Seh, J. Kibsgaard, C. F. Dickens, I. Chorkendorff, J. K. Nørskov and T. F. Jaramillo, *Science*, 2017, **355**, 4998.
171 G. Salvitti, F. Baroncelli, C. Nicotri, L. Evangelisti, S. Melandri and A. Maris, *Molecules*, 2022, **27**, 8190.
172 L. Xiao, S. Mou, X. Lin, K. Wu, S. Liu, W. Dai, W. Yang, C. Tang, C. Long and F. Dong, *Green Energy Environ.*, 2025, DOI: **10.1016/j.gee.2025.03.009**.
173 K. Yang, M. Li, S. Subramanian, M. A. Blommaert, W. A. Smith and T. Burdyny, *ACS Energy Lett.*, 2021, **6**, 4291–4298.
174 D. Panchal, Q. Lu, K. Sakaushi and X. Zhang, *Chem. Eng. J.*, 2024, 154920.
175 Z. Qu, R. Zhou, J. Sun, Y. Gao, Z. Li, T. Zhang, R. Zhou, D. Liu, X. Tu and P. Cullen, *ChemSusChem*, 2024, **17**, e202300783.
176 R. Snoeckx and A. Bogaerts, *Chem. Soc. Rev.*, 2017, **46**, 5805–5863.
177 T. Li, Y. Gao, R. Zhou, T. Zhang and K. K. Ostrikov, *Curr. Opin. Green Sustainable Chem.*, 2024, 100915.
178 N. Cherkasov, A. Ibhadon and P. Fitzpatrick, *Chem. Eng. Process.*, 2015, **90**, 24–33.
179 N. Rehbein and V. Cooray, *J. Electrost.*, 2001, **51**, 333–339.
180 P. Groen, W. Bongers, J. Janssen, T. Righart, A. van de Steeg, A. Wolf, M. van de Sanden and F. Peeters, *Chem. Eng. J.*, 2025, **503**, 158072.
181 S. Li, T. van Raak, R. Kriek, G. De Felice and F. Gallucci, *ACS Sustainable Chem. Eng.*, 2023, **11**, 12821–12832.
182 T. Li, Y. Gao, J. Fan, X. Wang, Y. Feng, Z. Qu, D. Gan, J. Sun, D. Liu and X. Tu, *Plasma Processes Polym.*, 2025, e2400257.
183 E. Vervloessem, Y. Gorbanev, A. Nikiforov, N. De Geyter and A. Bogaerts, *Green Chem.*, 2022, **24**, 916–929.
184 W. Wang, B. Patil, S. Heijkers, V. Hessel and A. Bogaerts, *ChemSusChem*, 2017, **10**, 2145–2157.
185 X. Ma, M. Chen, Z. Zheng, D. Bullen, J. Wang, C. Harrison, E. Gratz, Y. Lin, Z. Yang and Y. Zhang, *Joule*, 2021, **5**, 2955–2970.
186 S. Van Alphen, H. A. Eshtehardi, C. O'Modhrain, J. Bogaerts, H. Van Poyer, J. Creel, M.-P. Delplancke, R. Snyders and A. Bogaerts, *Chem. Eng. J.*, 2022, **443**, 136529.
187 S. Kelly and A. Bogaerts, *Joule*, 2021, **5**, 3006–3030.

188 S. Kelly and A. Bogaerts, *Joule*, 2021, **5**, 3006–3030.
189 A. Bogaerts and E. C. Neyts, *ACS Energy Lett.*, 2018, **3**, 1013–1027.
190 D. Gholami, S. Shahbazi, S. Mosleh, A. Ghoorchian, S. Hajati, K. Dashtian and G. Yasin, *Chem. Eng. J.*, 2023, **461**, 141950.
191 K. K. Sanap, S. Varma, S. Waghmode, P. Sharma, N. Manoj, R. Vatsa and S. Bharadwaj, *J. Nanosci. Nanotechnol.*, 2015, **15**, 3522–3529.
192 Q. Liu, N. Basel, L. Li, N. Xu, Q. Dong, L. Fan, Q. Wang, A. Ding and T. Wang, *J. Membr. Sci.*, 2022, **647**, 120296.
193 T. Banaszkiewicz and M. Chorowski, *Entropy*, 2018, **20**, 232.
194 H. U. Rasheed, J. Shim, J. H. Kim, K. Lee, S. H. Kim, H. Jung and H. C. Yoon, *Electrochim. Acta*, 2025, 146412.
195 T. Li, E. W. Lees, M. Goldman, D. A. Salvatore, D. M. Weekes and C. P. Berlinguette, *Joule*, 2019, **3**, 1487–1497.
196 J. Xu, Y. Kan, R. Huang, B. Zhang, B. Wang, K. Wu, Y. Lin, X. Sun, Q. Li and G. Centi, *ChemSusChem*, 2016, **9**, 1085–1089.
197 J. H. Goo, M. F. Irfan, S. D. Kim and S. C. Hong, *Chemosphere*, 2007, **67**, 718–723.
198 Q. Li, J. Zhao, H. Shang, Z. Ma, H. Cao, Y. Zhou, G. Li, D. Zhang and H. Li, *Environ. Sci. Technol.*, 2022, **56**, 5830–5839.
199 R. Chen, J. Wang, C. Zhang, Y. Sun, J. Li and F. Dong, *Environ. Sci. Technol.*, 2025, **59**(2), 1013–1033.
200 B. Li, Y. Pei and W. Shan, *Solid State Technol.*, 2020, **63**, 2438–2449.
201 H. Memon, Y. Wei and C. Zhu, *Mater. Today Commun.*, 2021, **29**, 102814.
202 J. Hu, L. Li, H. Li, Y. Zhai, F. Tang, Z. Zhang and B. Chen, *RSC Adv.*, 2022, **12**, 33716–33724.
203 D. Pan, M. Austeria P, S. Lee, H. Bae, F. He, G. H. Gu and W. Choi, *Nat. Commun.*, 2024, **15**, 7243.
204 A. Hauch, M. L. Traulsen, R. Küngas and T. L. Skafte, *J. Power Sources*, 2021, **506**, 230108.
205 A. Cronk, D. Larson and F. M. Toma, *arXiv*, 2020, preprint, arXiv:2010.11329, DOI: **10.48550/arXiv.2010.11329**.
206 Y. Gorbanev, E. Vervloessem, A. Nikiforov and A. Bogaerts, *ACS Sustainable Chem. Eng.*, 2020, **8**, 2996–3004.
207 S. Garg, C. A. G. Rodriguez, T. E. Rufford, J. R. Varcoe and B. Seger, *Energy Environ. Sci.*, 2022, **15**, 4440–4469.
208 C.-C. Weng, X.-W. Lv, J.-T. Ren, T.-Y. Ma and Z.-Y. Yuan, *Electrochem. Energy Rev.*, 2022, **5**, 19.
209 N. T. Nesbitt, T. Burdyny, H. Simonson, D. Salvatore, D. Bohra, R. Kas and W. A. Smith, *ACS Catal.*, 2020, **10**, 14093–14106.
210 D. Chen and H. Peng, *J. Dyn. Syst., Meas., Control*, 2005, **127**(3), 424–432.
211 P. Rani, V. Kasneryk and M. Opanasenko, *Appl. Mater. Today*, 2022, **26**, 101283.
212 Q. Ji, L. Bi, J. Zhang, H. Cao and X. S. Zhao, *Energy Environ. Sci.*, 2020, **13**, 1408–1428.
213 R.-B. Lin, S. Xiang, W. Zhou and B. Chen, *Chem*, 2020, **6**, 337–363.
214 S. Shahzadi, M. Akhtar, M. Arshad, M. H. Ijaz and M. R. S. A. Janjua, *RSC Adv.*, 2024, **14**, 27575–27607.
215 X. Zhang, D. Xue, S. Jiang, H. Xia, Y. Yang, W. Yan, J. Hu and J. Zhang, *InfoMat*, 2022, **4**, e12257.
216 W. P. Utomo, M. K. Leung, Z. Yin, H. Wu and Y. H. Ng, *Adv. Funct. Mater.*, 2022, **32**, 2106713.
217 Y. Li, X. Wei, L. Chen and J. Shi, *Angew. Chem., Int. Ed.*, 2021, **60**, 19550–19571.
218 X. Zou, J. Xie, C. Wang, G. Jiang, K. Tang and C. Chen, *Chin. Chem. Lett.*, 2023, **34**, 107908.
219 Y. Ren, C. Yu, X. Tan, X. Han, H. Huang, H. Huang and J. Qiu, *Small Methods*, 2019, **3**, 1900474.
220 B. H. Ko, B. Hasa, H. Shin, E. Jeng, S. Overa, W. Chen and F. Jiao, *Nat. Commun.*, 2020, **11**, 5856.
221 S. Hernandez-Aldave and E. Andreoli, *Catalysts*, 2020, **10**, 713.
222 J. Shen, Z. Tu and S. H. Chan, *Appl. Therm. Eng.*, 2020, **164**, 114464.
223 H.-J. Peng, C. Villevieille, S. Trabesinger, H. Wolf, K. Leitner and P. Novák, *J. Power Sources*, 2016, **335**, 91–97.
224 L. Grega, M. Kothari, A. Specian and S. Voinier, *J. Fuel Cell Sci. Technol.*, 2015, **12**, 061008.
225 H. Rabiee, L. Ge, J. Zhao, X. Zhang, M. Li, S. Hu, S. Smart, T. E. Rufford, Z. Zhu and H. Wang, *Appl. Catal., B*, 2022, **310**, 121362.
226 E. F. Johnson, E. Boutin, S. Liu and S. Haussener, *EES Catal.*, 2023, **1**, 704–719.
227 G. Chen, L. Ge, B. Ma, Y. Kuang, H. Rabiee, F. Dorosti, A. K. Nanjundan, Z. Zhu and H. Wang, *Appl. Catal., B*, 2025, **363**, 124803.
228 A. Singh-Morgan, K. Trösch, A. Weinfurter, M. Inniger, Y.-Z. Xu and V. Mougel, *Chem*, 2025, **11**(8), 102460.
229 S. Garg, C. A. G. Rodriguez, T. E. Rufford, J. R. Varcoe and B. Seger, *Energy Environ. Sci.*, 2022, **15**, 4440–4469.
230 R. Shi, J. Guo, X. Zhang, G. I. Waterhouse, Z. Han, Y. Zhao, L. Shang, C. Zhou, L. Jiang and T. Zhang, *Nat. Commun.*, 2020, **11**, 3028.
231 C. Ampelli, F. Tavella, D. Giusi, A. M. Ronsisvalle, S. Perathoner and G. Centi, *Catal. Today*, 2023, **421**, 114217.
232 L. Li, J. Wen, T. W. B. Lo, J. Yin and Q. Lei, *ChemistryMethods*, 2025, 2400080.
233 V. G. Kharitonov, A. R. Sundquist and V. S. Sharma, *J. Biol. Chem.*, 1994, **269**, 5881–5883.
234 CDC, Toxicological profiles, **https://www.atsdr.cdc.gov/toxicological-profiles/about/index.html**, (accessed June 11, 2025).
235 Handbook of chemistry and physics, **https://hbcp.chemnetbase.com/contents/ContentsSearch.xhtml?dswid=-6564**, (accessed June 11, 2025).
236 W. Lai, Y. Qiao, Y. Wang and H. Huang, *Adv. Mater.*, 2023, **35**, 2306288.
237 L. Fan, Z. Tu and S. H. Chan, *Int. J. Hydrogen Energy*, 2023, **48**, 7828–7865.
238 E. J. Choi, J. Y. Park and M. S. Kim, *Int. J. Hydrogen Energy*, 2018, **43**, 13406–13419.
239 J. Zhang, C. Wang and A. Zhang, *Appl. Energy*, 2022, **311**, 118646.

240 Z. Huang and Q. Jian, *Appl. Therm. Eng.*, 2022, **217**, 119238.
241 T. L. Kösters, X. Liu, D. Kožulović, S. Wang, J. Friedrichs and X. Gao, *Int. J. Hydrogen Energy*, 2022, **47**, 29399–29412.
242 Y. Yu, M. Chen, S. Zaman, S. Xing, M. Wang and H. Wang, *ETransportation*, 2022, **12**, 100165.
243 W.-M. Yan, M.-S. Zeng, T.-F. Yang, C.-Y. Chen, M. Amani and P. Amani, *Int. J. Hydrogen Energy*, 2020, **45**, 22324–22339.
244 D. Qiu, L. Peng, P. Yi, W. Lehnert and X. Lai, *Renewable Sustainable Energy Rev.*, 2021, **152**, 111660.
245 D. Qiu, P. Yi, L. Peng and X. Lai, *J. Fuel Cell Sci. Technol.*, 2015, **12**, 041002.
246 C. Wu, W. Zhang, X. Han, Y. Zhang and G. Ma, *J. Power Sources*, 2020, **476**, 228724.
247 B. Liu, M. Wei, G. Ma, W. Zhang and C. Wu, *Int. J. Hydrogen Energy*, 2016, **41**, 2911–2918.
248 L. Peng, D. Qiu, P. Yi and X. Lai, *J. Electrochem. Energy Convers. Storage*, 2016, **13**, 021007.
249 L. Pang, Y. Shao, W. Zhong, Z. Gong and H. Liu, *Energy*, 2020, **194**, 116756.
250 P. C. Okonkwo, *Catalysts*, 2025, **15**, 97.
251 Y. Yu, Q. Han, H. Lin, S. Zhang, Q. Yang and F. Liu, *J. Membr. Sci.*, 2022, **660**, 120872.
252 X. Yang, P. Wang, Q. Li, W. Nie and M. Sun, *IEEE*, 2024, pp. 125–128.
253 B. Li, K. Wan, M. Xie, T. Chu, X. Wang, X. Li, D. Yang, P. Ming and C. Zhang, *Appl. Energy*, 2022, **314**, 119020.
254 C. Wang, M. Dou, Z. Li, R. Outbib, D. Zhao, J. Zuo, Y. Wang, B. Liang and P. Wang, *Reliability Eng. System Safety*, 2023, **233**, 109123.
255 R. F. Mann, J. C. Amphlett, M. A. Hooper, H. M. Jensen, B. A. Peppley and P. R. Roberge, *J. Power Sources*, 2000, **86**, 173–180.
256 D. Hao, J. Shen, Y. Hou, Y. Zhou and H. Wang, *Int. J. Chem. Eng.*, 2016, **2016**, 4109204.
257 Y. Wang, X. Kang and Z. Chen, *Green Energy Intell. Trans.*, 2022, **1**, 100014.
258 C. Chen, R. Xiong, R. Yang and H. Li, *Green Energy Intell. Trans.*, 2022, **1**, 100001.
259 Z. Li, Y. Wang, Y. Mu, B. Wu, Y. Jiang, L. Zeng and T. Zhao, *Renewable Sustainable Energy Rev.*, 2023, **176**, 113182.
260 G. Wang, Z. Luo, H. G. Desta, M. Chen, Y. Dong and B. Lin, *Energy Rev.*, 2024, 100106.
261 A. Priya, B. Devarajan, A. Alagumalai and H. Song, *Sci. Total Environ.*, 2023, **886**, 163913.
262 T. Lombardo, M. Duquesnoy, H. El-Bouysidy, F. Årén, A. Gallo-Bueno, P. B. Jørgensen, A. Bhowmik, A. Demortière, E. Ayerbe and F. Alcaide, *Chem. Rev.*, 2021, **122**, 10899–10969.
263 A. M. Mroz, A. R. Basford, F. Hastedt, I. S. Jayasekera, I. Mosquera-Lois, R. Sedgwick, P. J. Ballester, J. D. Bocarsly, E. A. del Río Chanona and M. L. Evans, *Chem. Soc. Rev.*, 2025, **54**, 5433–5469.
264 X. Wang, S. Zhao, T. Guo, L. Yang, Q. Zhao, Y. Wu and Y. Chen, *Trans. Tianjin Univ.*, 2024, **30**, 117–129.
265 A. Buttler and H. Spliethoff, *Renewable Sustainable Energy Rev.*, 2018, **82**, 2440–2454.
266 P. De Luna, C. Hahn, D. Higgins, S. A. Jaffer, T. F. Jaramillo and E. H. Sargent, *Science*, 2019, **364**, eaav3506.
267 J. W. Sun, H. Q. Fu, P. F. Liu, A. Chen, P. Liu, H. G. Yang and H. Zhao, *EES Catal.*, 2023, **1**, 934–949.
268 Q. Ye, X. Zhao, R. Jin, F. Dong, H. Xie and B. Deng, *J. Mater. Chem. A*, 2023, **11**, 21498–21515.
269 M. Jouny, W. Luc and F. Jiao, *Ind. Eng. Chem. Res.*, 2018, **57**, 2165–2177.
270 Energy transition outlook, **https://www.dnv.com/energy-transition-outlook/**, (accessed June 11, 2025).
271 Carbon border adjustment mechanism – european commission, **https://taxation-customs.ec.europa.eu/carbon-border-adjustment-mechanism_en**, (accessed June 11, 2025).
272 Guarantee of origin scheme – DCCEEW, **https://www.dcceew.gov.au/energy/renewable/guarantee-of-origin-scheme**, (accessed June 11, 2025).
273 D. T. Ton and M. A. Smith, *Electricity J.*, 2012, **25**, 84–94.
274 Enapter AEM electrolysers: Produce maximum green hydrogen from renewables – green hydrogen – enapter, **https://www.enapter.com/**, (accessed June 11, 2025).

